Aaro Väkeväinen

Electron-beam induced optical superresolution in integrated light-electron microscopy

School of Science

Thesis submitted for examination for the degree of Master of Science in Technology.

Espoo 28.10.2014

Thesis supervisor:

Prof. Päivi Törmä

Thesis advisor:

Dr. Jacob Hoogenboom

Aalto University
School of Science

AALTO UNIVERSITY
SCHOOL OF SCIENCE

ABSTRACT OF THE
MASTER'S THESIS

Author: Aaro Väkeväinen

Title: Electron-beam induced optical superresolution in integrated light-electron microscopy

Date: 28.10.2014 Language: English Number of pages: 6+101

Department of Applied Physics
Professorship: Engineering Physics, Theoretical and Computational Physics
Code: Tfy-105

Supervisor: Prof. Päivi Törmä

Advisor: Dr. Jacob Hoogenboom

Abstract:

We have developed an optical superresolution method based on electron-bleaching of fluorophores in integrated light-electron microscopy. The main advantage of this novel superresolution method is that the non-fluorescent ultrastructure of the sample can be revealed by the simultaneously acquired SEM image. Furthermore, as the fluorescence superresolution image is based on an electron-beam-induced modification of the specimen, by "switching off" fluorescent probes, both the fluorescence and SEM image are recorded with perfect spatial overlap - being a great advantage for correlative imaging. The superresolution method is demonstrated with fluorescent microspheres, having a diameter of 40–50 nm. Their bleaching behaviour is studied as a function of various exposure parameters, and we show that the bleaching rate is mostly dependent on the injected electron dose and electron landing energy. The superresolution experiments are performed in an integrated light-electron microscope platform (SECOM, Delmic), with which fluorescence emission of the sample can be monitored while the electron beam scans over it. The method is successfully demonstrated with the fluorescent beads on ITO-coated glass and TEM-grid substrates. We have achieved a localization precision of approximately 100 nm of the fluorescent beads, and an image resolution of 160 nm – well beyond the diffraction limit of light. The method may eventually provide an excellent tool for researchers doing correlative light-electron microscopy in modern life sciences, such as cell and molecular biology.

Keywords: Fluorescence microscopy, correlative light-electron microscopy, optical superresolution, electronbleaching

AALTO-YLIOPISTO
PERUSTIETEIDEN KORKEAKOULU

DIPLOMITYÖN
TIIVISTELMÄ

Tekijä: Aaro Väkeväinen

Työn nimi: Optinen superresoluutio käyttäen hyväksi elektronisuihkua integroidussa valo-elektronimikroskopiassa

Päivämäärä: 28.10.2014 Kieli: Englanti Sivumäärä: 6+101

Teknillisen fysiikan laitos
Professuuri: Teknillinen fysiikka, teoreettinen ja laskennallinen fysiikka
Koodi: Tfy-105

Valvoja: Prof. Päivi Törmä

Ohjaaja: Dr. Jacob Hoogenboom

Tiivistelmä:

Olemme kehittäneet optisen superresoluutiomenetelmän, joka perustuu fluoresoivien molekyylien elektronisuihkuvalkaisuun integroidussa valo-elektronimikroskopiassa. Tämän aivan uudenlaisen superresoluutiomenetelmän suurin etu on, että näytteen ei-fluoresoiva hienorakenne pystytään paljastamaan samaan aikaan otetun elektronimikroskooppikuvan avulla. Koska fluoresenssikuva kerätään ”sammuttamalla” fluoresoivia molekyylejä elektronisuihkun avulla, on fluoresenssi- ja elektronimikroskooppikuvien koordinaatisto täsmälleen sama, mikä on suureksi hyödyksi ajatellen korreloivaa kuvantamista. Superresoluutiomenetelmä demonstroidaan fluoresoivien mikropallojen avulla, joiden halkaisija on 40–50 nm. Ensimmäiseksi mikropallojen sammumiskäyttäytymistä tutkitaan eri valkaisuparametrien funktiona. Näytämme, että valkaisunopeus riippuu enimmäkseen syötetystä elektroniannoksesta ja elektronien energiasta. Superresoluutiokokeet toteutetaan integroidulla valo-elektronimikroskooppialustalla (SECOM, Delmic), jossa fluoresenssisignaalia voidaan tarkkailla samalla kun elektronisuihku pyyhkii näytteen pintaa. Menetelmän osoitetaan toimivan ITO-päällystetyillä lasialustoilla, sekä TEM-hiloilla. Olemme saavuttaneet n. 100 nm tarkkuuden fluoresoivien mikropallojen lokalisaatiossa, fluoresenssikuvan resoluution ollessa n. 160 nm, joka on reilusti valon diffraktiorajan alapuolella. Menetelmä voi aikanaan tarjota erinomaisen työkalun tutkijoille, jotka hyödyntävät korreloivaa valo-elektronimikroskopiaa biotieteissä, kuten solu- ja molekyylibiologiassa.

Avainsanat: Fluoresenssimikroskopia, korrelatiivinen valo-elektronimikroskopia, optinen superresoluutio, elektronisuihkuvalkaisu

Preface

This Master's thesis is based on the work carried out in the research group of Charged Particle Optics (CPO) at the Department of Imaging Physics, Delft University of Technology, headed by Prof. Pieter Kruit. I wish to thank my advisor Dr. Jacob Hoogenboom for welcoming me to work on his project. I am very happy with my choice and I enjoyed my time in the group and in the Netherlands. I thank Jacob for the long insightful discussions and pushing me into the right direction. I also thank Pieter for his valuable comments and suggestions during the project meetings.

Next, I wish to thank Dr. Robert Moerland, former supervisor, colleague and a friend of mine from previous work in the Quantum Dynamics group at Aalto University. Without Robert I would not have found this great opportunity to work in Delft, and without Robert I would not be the experimental physicist I am now. I want to thank Gerward Weppelman, who always had time to help me with all kinds of issues with the electron microscopes. Gerward also offered me a couch to sleep on in the last two weeks when I was finishing my experiments. I am grateful for the support from Delmic. Special thanks must go to Éric Piel who made a crucial contribution to the project by providing the control software and patient troubleshooting service. In addition, I wish to thank Martijn Haring for transferring the know-how from earlier experiments, and Jan de Looff for the customized component manufacturing. Finally, I want to thank all other colleagues and staff members I had the pleasure to work with in the CPO group.

In Finland, I wish to thank Prof. Päivi Törmä for being my supervisor on behalf of Aalto University. I do not regret a tiny bit of taking the opportunity in 2010 to start to do research under Päivi's guidance. I also want to thank all the great friends I have made during my university studies, and the ones who have come along from the earlier years. It has been quite a journey.

I am grateful for the endless support from my family through the hard times, without them I would not be this far. Kiitos äiti ja isä.

Espoossa, 28.10.2014

Aaro Väkeväinen

Contents

CHAPTER 1

Introduction

Fluorescence microscopy (FM) is today a widely used method in biological imaging where cellular functions are tracked with the help of fluorescent labels [1]. However, everything non-labelled remains invisible, and so do the details of the surrounding ultrastructure. In contrast, electron microscopy (EM) can reveal the ultrastructure of the sample at nanometer scale resolution. By combining the information and overlaying the optical FM image with the EM image, researchers may obtain more comprehensive understanding of the actions taking place in the cellular specimen. This approach, known as correlative light-electron microscopy (CLEM), has gathered great attention especially over the last decade [2–8]. The conventional way of performing CLEM has, however, several drawbacks. FM and EM imaging with two separate microscopes is often cumbersome and very time consuming. Transfer between the microscopes makes the sample vulnerable to contamination and damage, and finding back the desired region-of-interest (ROI) may be difficult. Furthermore, it is hard to obtain a high overlay precision. To overcome these difficulties, researchers in our group have developed a simultaneous integrated correlative light-electron microscopy platform, known as scanning electron combined optical microscope (SECOM) [7, 9, 10]. In this study, we use the platform to explore a totally new approach for acquiring the FM signals of the sample during electron-scanning, resulting in sub-diffraction limited localization of fluorescent probes.

The integrated SECOM platform provides the flexibility to easily move back and forth between optical imaging and the EM, keeping the ROI stationary in the field-of-view of both microscopes. In addition, the SECOM provides an excellent overlay accuracy between the FM and EM images. However, the optical

resolution is still limited by the diffraction limit of light, which is for the visible wavelengths around 250 nm. In other words, even though the ultrastructure of the sample is revealed with the EM, the fluorescent probes in close proximity, inside a diffraction-limited fluorescence spot, cannot be accurately resolved, leading to issues with densely-labelled specimens. Even if so called dual-contrast probes are used, showing up in both FM and EM images (e.g. quantum dots or fluorophore-labelled gold nanoparticles), several probes with different colors cannot be resolved within a diffraction limited spot. Nonetheless, the dimensions of the biological subcellular structures are far below the diffraction limit of light. Localizing the fluorescent probes more accurately within the specimen ultrastructure would offer valuable information, e.g., for researchers who need to know whether a protein or a virus attaches inside or outside a few nanometer thick cell membrane. This is the ultimate goal of where we are heading to. Several superresolution FM techniques have been developed during the last two decades, which are capable to optically distinguish objects closer to each other than the diffraction limit of light. However, most of the existing techniques require very particular fluorescent probes, or high laser powers, and might therefore be difficult to implement in the EM conditions.

The aim of this Master's project is to develop an electron-beam-induced optical superresolution method to overcome the diffraction barrier in an integrated light-electron microscope, where the optical superresolution image and the SEM image can be acquired at the same time. The major advantage of this method over other existing superresolution methods is indeed the simultaneous acquisition of the structural SEM signal with an electron-beam induced change in the optical signal. By modifying the fluorescent particles with the electron beam, namely switching them "off", we demonstrate optical superresolution on our test samples on the SECOM platform. The concept of the method was already demonstrated earlier by another Master's student, but only by one-dimensional line scanning over a fluorescent particle [11]. Here, we go beyond that study by implementing a scanning procedure in two dimensions.

This thesis has been divided into five chapters between Introduction and Conclusion. In Chapter 2, I first provide an overview of biological imaging, i.e. fluorescence and electron microscopy. I focus on the phenomenon of fluorescence, the principle and limitations of fluorescence microscopy, and the principle of correlative light-electron microscopy. I also introduce the most important existing super-

resolution techniques in light microscopy. In Chapter 3, I discuss the theoretical background of photobleaching and electron-beam-induced bleaching of fluorescent molecules, including a summary of electron-matter interaction in the SEM. In Chapter 4, I have studied the bleaching behaviour of the fluorophore-doped polymer beads used later in the superresolution experiments. The bleaching rate is studied as a function of various parameters, such as injected electron-dose and electron landing energy. In Chapter 5, I cover the development of the novel superresolution method. I thoroughly explain the design of the SECOM platform and how it is used to perform the electron-beam-induced superresolution imaging. The principle of the method is explained in high detail. A discussion on the practical implementation of the method can be found with an explanation of the external control of the electron beam. In Chapter 6, the results obtained with the method are presented, and an outlook is provided on the current state of the development, with recommendations for future study.

CHAPTER 2

Imaging in biology: Fluorescence and Electron Microscopy

Fluorescence imaging plays a role of critical importance in the modern life sciences. It is a widely used optical imaging method in biochemistry, especially in molecular and cell biology, which both deal with the molecular basis of biological activity in cellular systems [1].

In this chapter, I discuss the basis of fluorescence and the various important properties of fluorophores, i.e. fluorescent chemical compounds. I explain the principle of fluorescence microscopy which is the main application of fluorescence imaging. Moreover, the correlative light-electron microscopy is introduced and the principle of electron imaging is discussed insofar required. Finally, the most important existing optical superresolution techniques are covered with their advantages and drawbacks. After this chapter, the reader should understand why we are developing an imaging method which could ultimately produce an optical superresolution image perfectly overlaid with the specimen ultrastructure, both provided by the SEM, with nanometer scale resolution.

2.1 Fluorescence

First of all, let us discuss photoluminescence, i.e light emission resulting from absorption of a photon by any substance. In this phenomenon, the absorbed photon gives up its energy to an electron and kicks it up to an excited state. When the electron returns to its ground state, another photon is emitted. Photoluminescence can be formally divided into fluorescence and phosphorescence, of which fluorescence is of the main interest for this study. The division is based on the life-

time of the excited state which furthermore depends on the nature of the excited state that the electron finally ends in: fluorescence refers to a transition between spin-singlet states while phosphorescence refers to a transition between a triplet and a singlet state. The processes of fluorescence and phosphorescence are illustrated by Jablonski diagram in Figure 2.1, which will be explained below in detail.

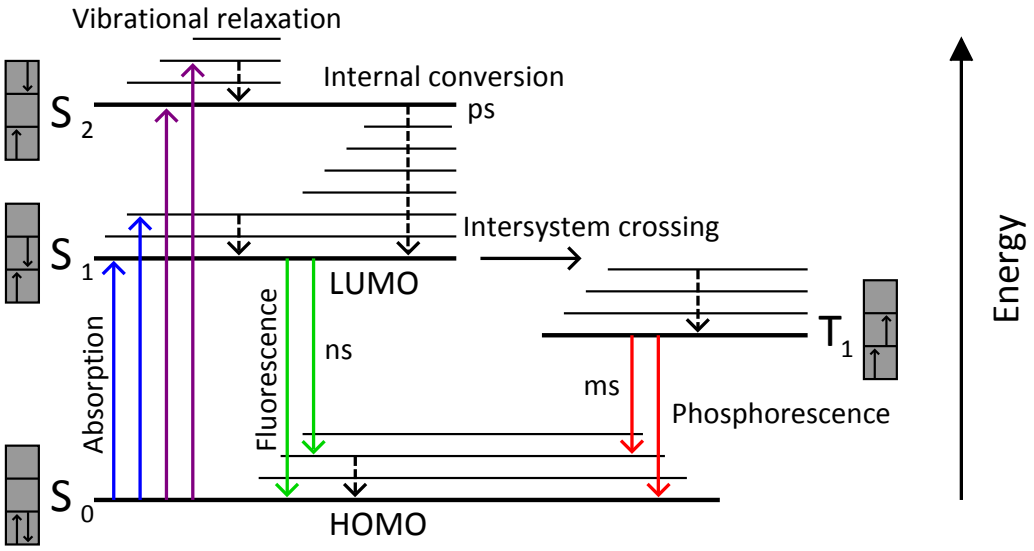

Figure 2.1: *Jablonski diagram. The diagram illustrates the orbital structure of a molecule and possible transitions between the electronic states (including rough time scales). Vibrational ground states are sketched with thick horizontal lines, whereas the thin lines represent higher vibrational energy-levels of the molecular orbitals. Here, S_0 is the electronic ground state and S_1 the first excited singlet-state of the molecule, corresponding to the HOMO and LUMO, respectively. The first (excited) triplet-state is named T_1, and the second excited singlet-state S_2. The essential electron configuration of each state is depicted in gray boxes where each arrow pointing up or down represents an electron with its spin-orientation. The total spin of a singlet-state is always zero, so the excited electron has an opposite spin to its electron pair, remaining in the ground state. In the triplet-state, the electrons have parallel spins, whereupon the typical electric dipole transition to the ground state is forbidden (Pauli exclusion principle).*

This section has the focus on fluorescent molecules, even though some other substances exhibit fluorescent behaviour as well. Other fluorescent substances include solid-state quantum dots and nitrogen-vacancies in diamond, where the nitrogen-vacancies act as color centers. However, we want to restrict ourselves in explaining the fluorescent behaviour of molecules, as molecules are the most common fluorophores used in biological imaging, and the fluorescent polystyrene particles used in this study are also doped with such molecules. In addition, most

of the principles of fluorescence may be applied to any type of fluorescent substance.

2.1.1 Electronic transitions

In fluorescent molecules, the electronic transitions occur mostly between the highest occupied molecular orbital (HOMO) and the lowest unoccupied molecular orbital (LUMO). Molecules have vibrational degrees of freedom which produces a discrete energy-level spectrum for the molecular orbitals, so-called vibrational states. At room temperature thermal energy is small compared to the separation between the vibrational states, thus the electronic excitation of a molecule typically starts from the vibrational ground state of the HOMO with no vibrational quanta excited [12].

The molecular excitation may be resonant meaning that the energy of the absorbed photon equals the energy difference between the vibrational ground states of S_0 and S_1 (see Figure 2.1). However, often this is not the case but the molecule is excited to some of the higher vibrational energy-levels of S_1, or even S_2. Nuclei are stationary during electronic transitions, which occur in less than 1 fs, a time too short for significant displacement of nuclei. The reason is that nuclear masses are much larger than the mass of an electron, yielding a much larger inertia. Therefore, the transitions between vibrational states owning similar nuclear coordinates are more probable than the transitions between other states. In the quantum mechanical picture, vibronic transitions are favoured between states of which vibrational wavefunctions overlap the most [13, 14]. This is known as the Franck-Condon principle. Vibronic transition refers to a simultaneous changes in the vibrational and electronic energy states of the molecule. Figure 2.2 illustrates the Franck–Condon principle with transitions in a diatomic molecule.

After excitation to either S_1 or S_2, the electron quickly goes through a vibrational relaxation process generating phonons (heat) and ending up in the lowest vibrational level of the LUMO. This is know as the Kasha rule. Vibrational relaxation between the electronic states is called internal conversion, which commonly occurs if the vibrational states of the molecular orbitals sufficiently overlap. Internal conversion occurs on the order of picoseconds, whereas a typical fluorescence lifetime is between 1–10 ns. Therefore, the relaxation process is generally complete prior to emission, and the emission takes place from a thermally equilibrated excited state, that is, the vibrational ground state of the LUMO. As a direct

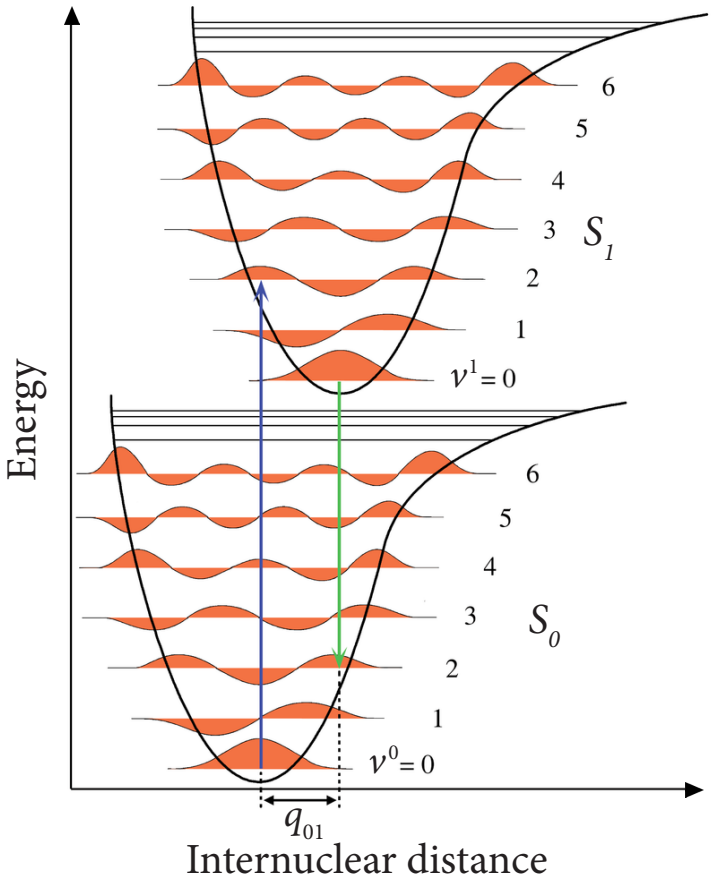

Figure 2.2: *Energy diagram of a diatomic molecule where the potential energy curves of the ground state and the excited state are approximated with a so-called Morse potential. The wavefunctions of the vibrational states are depicted with orange color. Since electronic transitions take place in a stationary nuclear framework, vibronic transitions are most probable when they correspond to a minimal change in the nuclear coordinates (internuclear distance). The potential wells here are shown to favour transitions between vibrational levels $v = 0$ and $v = 2$. Electronic excitation is depicted with a blue and fluorescent emission with a green arrow, corresponding to the depiction in Figure 2.1. The figure is a modified version of the one in [15].*

consequence of the Franck–Condon principle, return to S_0 very likely occurs to some of the higher vibrational states as well, followed by the final relaxation to the vibrational ground state of the HOMO.

Electronic transition between spin-singlet states is quantum mechanically allowed, and therefore fluorescence emission takes place relatively rapidly. However, due to non-negligible spin-orbit coupling in molecules, there is a finite torque acting on the electron in the excited state resulting in a tiny but significant probability that the spin of the excited electron is flipped upon excitation. This process is know as intersystem crossing and leads the excited electron to a spin-triplet

state. Transition between a triplet state and a singlet state is forbidden by the Pauli exclusion principle, which states that two electrons with parallel spins cannot exist in the same molecular orbital. Therefore, decay to the ground state requires a reverse spin-flip, and takes much longer time (phosphorescence). A typical phosphorescence lifetime is on the order of milliseconds but can easily extend to seconds. The energy of a triplet state is generally lower than that of the corresponding singlet state because the exchange interaction of parallel spins increases the average distance of the electrons, according to the Hund's rule [12].

2.1.2 Stokes shift and spectral broadening

In general, a vibronic transition from the vibrational ground state of the HOMO is more probable to some of the higher vibrational state of the LUMO, and vice versa, depending on the potential well structure of the molecular orbitals (see Figure 2.2). It follows that the fluorescence emission is always longer than the absorption wavelength. Difference between the absorption and emission maxima is know as the Stokes shift, which is one of the most prominent characteristic of a fluorophore. The Stokes shift is usually a few tens of nanometers but may be considerably larger in some special cases, as will be seen later on.

Ideally the photophysical electronic transitions in the molecule, i.e. absorption and emission of a photon, would lead to a discrete absorption and emission spectrum. However, in practice narrow separated spectral lines can be only observed in dilute gases. The reason is homogeneous and inhomogeneous broadening of the spectra. Firstly, homogeneous broadening refers to broadening of a single spectral line, which is the same for all molecules. It results to Lorentzian line shapes and originates from natural lifetime broadening, as well as pressure broadening for gases. Natural lifetime broadening can be explained with the Heisenberg uncertainty principle. Heisenberg requires that the finite lifetime of an electronic excited state yields to uncertainty of the energy of the excited state, in respect to the ground state.

Inhomogeneous broadening, on the other hand, originates mostly from the inherent disorder in liquid and solid samples in molecular scale, and includes effects like Doppler broadening for gases. Each molecule in the liquid/solid sample experiences a slightly different molecular environment, e.g. a local electric field, which modifies the transition energies of the molecule. Therefore, each molecule also has a slightly different absorption/emission spectrum, and the total spectra

are made up of all of the different spectra of individual molecules. Inhomogeneous broadening commonly results in a Gaussian shape spectrum [14].

2.1.3 Competing processes

The decay by emitting a photon is not the only possible decay mechanism of the electronic excitation of a molecule. In this subsection, we discuss non-radiative decay processes, which suppress the photoluminescence of a molecule, or even make it completely non-luminescent. In fact, most of the molecules are neither fluorescent or phosphorescent. This is the main reason that we need fluorescent probes for fluorescence imaging.

One of the most likely non-radiative decay mechanisms is vibrational relaxation, i.e. internal conversion all the way down to the vibrational ground state of the HOMO. Most molecular compounds have vibrational states filling up the gaps between the different electronic states, making an internal conversion favourable. Therefore, these molecules absorb light but do not show any type of emission. Other non-radiative decay mechanisms include quenching and photochemical reactions. Photochemical reactions sometimes result to photobleaching transferring an initially fluorescent molecule irreversibly to a non-radiative state. Photobleaching is an important phenomenon concerning this study, and it is discussed in detail in Chapter 3.

The decrease of the fluorescence rate due to any short-range interactions between the fluorophore and the local molecular environment is called quenching. A variety of processes can result in quenching, such as excited state reactions, charge transfer and non-radiative energy transfer between the excited fluorophore and the quencher. Firstly, the excited fluorophore may form a loosely associated non-radiative complex with the quencher or with the other fluorophores (self-quenching). Secondly, near metal surfaces or metallic nanoparticles the energy of excited electron may be dissipated by ohmic losses in the metal. Ohmic dissipations occurs near metals because of the near-field coupling that induces electric currents in the metal. On the other hand, the excited fluorescent molecule may give up its energy to another molecule through non-radiative fluorescence resonance energy transfer (FRET).

The most well-known quencher is molecular oxygen which is an efficient quencher to almost all known fluorophores. The paramagnetic nature of molecular oxygen (O_2) can induce the fluorophore to undergo an intersystem crossing to

its triplet state. Because the emission from the triplet-state is slow, it is highly suppressed with other quenching processes or other non-radiative decay mechanisms. Other well-know quenchers are heavy halogen atoms and amides [16], and of course metallic substances. It should be noted that quenching generally occurs without any permanent change in the molecule, that is, without a photochemical reaction.

The intersystem crossing between an excited singlet- and triplet-state causes also so-called fluorescence intermittency, i.e. fluorescence blinking phenomenon. In fluorescence blinking, a fluorescent molecule temporarily "turns off" from time to time because of the long lifetime of the triplet state (on the order of milliseconds). It is a common property of fluorophores and has been shown, e.g., for green fluorescent protein [17]. We come back to the blinking phenomenon in Chapter 3.

2.1.4 Properties of fluorophores

Besides the absorption/emission spectra and the Stokes shift, the most important characteristics of a fluorophore include extinction coefficient, fluorescent lifetime and quantum yield. The quantum yield, or the quantum efficiency, of a fluorescent molecule is the number of emitted photons relative to the number of absorbed ones. The number of absorbed photons depends on the extinction cross-section of the molecule, and of course on the excitation irradiance. The extinction cross-section, i.e. the extinction coefficient, describes the probability of a scattering or an absorption event to occur. Because light scattering by objects of molecular length scale is negligible, the main factor left here is the absorption cross section. Absorption rate is directly proportional to the absorption cross-section (absorption coefficient, σ_a) and photon flux according to [18]

$$k_a = \sigma_a I \frac{\lambda_{ex}}{hc} \ [s^{-1}], \tag{2.1}$$

where I is the irradiance, i.e. excitation light intensity, λ_{ex} is the excitation wavelength, h the Planck's constant and c the speed of light. Here, hc/λ is the photon energy.

Quantum yield and fluorescent lifetime can be derived from radiative and non-radiative decay rates of the excited state. Figure 2.3 shows a simplified

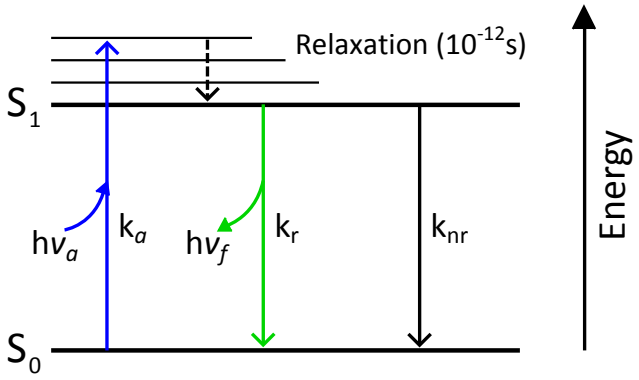

Figure 2.3: *Simplified Jablonski diagram showing absorption, radiative and non-radiative rate constants. [16]. Absorbed and emitted photons have energies of $h\upsilon_a$ and $h\upsilon_f$, respectively, where h is the Planck's constant and υ the frequency.*

Jablonski diagram with rate constants. The quantum yield is given by [16]

$$Q = \frac{k_r}{k_r + k_{nr}} = \frac{1}{1 + \frac{k_{nr}}{k_r}}, \tag{2.2}$$

where k_r is the rate $[s^{-1}]$ for radiative and k_{nr} for non-radiative decay. Here, k_{nr} includes all possible non-radiative decay processes. It is the ratio between k_{nr} and k_r that determines if the molecule is fluorescent or not. For good fluorophores, the fluorescence quantum yield is close to unity.

The fluorescent lifetime represents the average time that the molecule spends in the excited state prior to return to the ground state. Typical lifetimes for fluorophores are in the range of 1–10 ns. However, only few molecules of an ensemble return to the ground state at exactly the average time, as the decay from the excited state is a random process. The decay process follows Poisson statistics where events occur independently of each other, at a rate relative to the normalized population of the excited state (at $t = 0$ population equals unity). Poisson statistics results in exponential decay distribution, and if the excitation occurs at time $t = 0$, the normalized population of the excited state S_1 is given by

$$S_1 = \exp\left(-\frac{t}{\tau}\right), \tag{2.3}$$

where the lifetime τ corresponds to $1/e$ value of the exponential decay function. Statistically 63% of the molecules have decayed prior to time $t = \tau$. Here, τ is also

called the decay time constant. The lifetime of a fluorophore is simply given by

$$\tau = \frac{1}{k_r + k_{nr}}, \tag{2.4}$$

which follows directly from the rate equations

$$\begin{aligned} \frac{dS_0}{dt} &= -k_a S_0 + (k_r + k_{nr}) S_1 \\ \frac{dS_1}{dt} &= \ \ k_a S_0 - (k_r + k_{nr}) S_1, \end{aligned} \tag{2.5}$$

by setting $S_0 = 0$ in the latter equation (all molecules are in the excited state at $t = 0$). In general, the relationship between rate constants yield to the probability of the corresponding transitions. More comprehensive rate equations of the fluorescence cycle can be found in Chapter 3, in the discussion of photobleaching.

In summary, the fluorescence strength is directly proportional to the absorption coefficient, the excitation irradiance and the quantum yield, and certainly to the fluorophore concentration in others but single-molecule measurements. As already mentioned, only few molecules fluoresce efficiently, as the radiative decay only occurs for molecules exhibiting a low density of vibrational states on the HOMO and the LUMO energies. Under such circumstances an internal conversion to the ground state is not likely to occur. Particularly efficient fluorescence, i.e. high quantum yield, is observed for small and rigid aromatic/conjugated molecules such as Rhodamine. These compounds form an important sub-class of fluorophores, know as dye molecules. Efficiently phosphorescent substances are even more rare, as besides a low chance of non-radiative decay, they must involve a very low fluorescence quantum yield to make intersystem crossing and emission from the triplet-state more favourable.

To conclude, the purpose of this section was to go through the basic principles of fluorescence and related phenomena to be able to understand fluorescence microscopy, and to build up basic knowledge considering fluorescence bleaching discussed in Chapter 3.

2.2 Principle of fluorescence microscopy

In fluorescence microscopy (FM), the optical image is generated by fluorescence of the sample which provides particular contrast in the image. In regular optical microscopy, the contrast is provided by light absorption and scattering, which become extremely weak by small and thin objects, having dimensions on the order of the wavelength of light or smaller. This is, however, typical for cellular specimens. Few biological molecules are auto-fluorescent, meaning that they are naturally fluorescent and show up automatically in fluorescence images. Therefore, to make the inspection with the FM possible in general, the specimen needs to be stained with additional fluorescent molecules, called fluorescent markers or fluorescent probes. Fluorescent probes are typically programmed to attach to certain sites in the specimen, such as the cell nuclei, and they can be used for tracking proteins and other biological molecules. Probes with different colors may be used to separate different types of objects in the image. Therefore, fluorescence microscopy is able to reveal the biological functions in the cellular structure, even in living organisms (*in vivo*) by using proteins with intrinsic fluorescence. Figure 2.4 shows an example of a dual-color fluorescence images of a biological tissue.

2.2.1 Operational principle

The fluorescence of a sample is typically not very strong compared to the excitation light intensity. Hence, the operational principle of any fluorescence microscope lies in filtering the fluorescence signal from the excitation light, in order to obtain theoretically a zero-background (in thin samples). A fluorescence microscope may use the design of a standard inverted wide-field microscope or a more advanced technique, such as confocal microscopy. An inverted (epi-illumination) wide-field fluorescence microscope is referred to as an epi-fluorescence microscope, where the excitation and emission light travels to and from the sample via the same objective lens. The operational principle of an epi-fluorescence microscope is depicted in Figure 2.5.

In an epi-fluorescence microscope, the excitation light is guided to the sample through a dichroic beam-splitter which is a semi-transparent thin-film mirror, also know as a dichroic mirror. The dichroic mirror reflects a certain part of the spectrum, and transmits the other part, based on interference in the thin-film

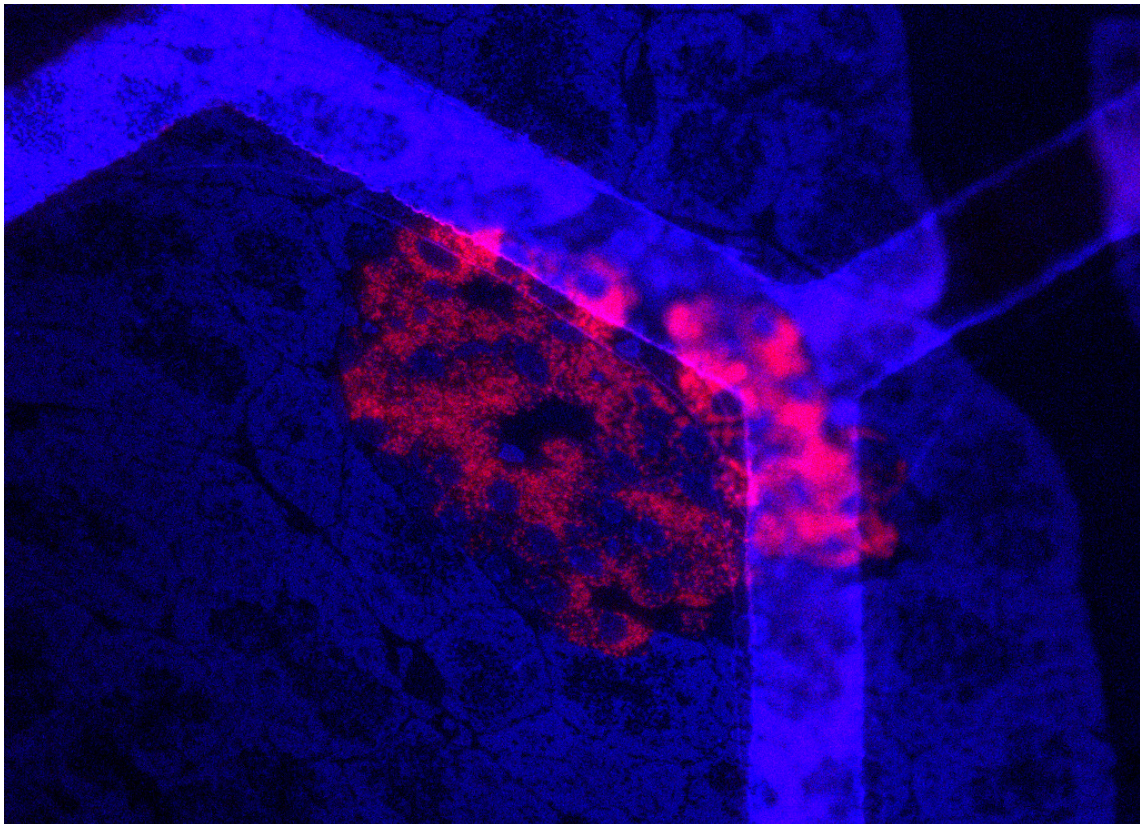

Figure 2.4: *Two-color fluorescence image of a diabetic-rat pancreas-tissue with red-emission quantum dots labelling insulin granules (red). The image is acquired with a confocal laser-scanning fluorescence microscope. To make the entire tissue visible in the FM, it is additionally stained with Hoechst, i.e. a nucleic acid stain of a fluorescent organic dye (blue). The tissue section is places on a TEM-grid which shows also in the image. The colors here are artificial: the red and blue correspond to emission subsequently recorded with two separate color channels, with different excitation laser and filter sets.*

structure. In the FM, the dichroic mirror reflects the excitation wavelengths and transmits the fluorescence. Dichroic mirrors are, however, not very good filters so a separate emission filter must be used to fully block the excitation light entering the detector. If needed, an excitation filter may be used to restrict the excitation spectrum. When the excitation light hits the sample and excites the fluorophores, they eventually emit light in all directions. To collect a maximal amount of emission, a high-NA objective must be used.

One of the main advantages of fluorescence imaging is its ability to reveal the interplay of different types of bio-molecules, by labelling them with different fluorescent probes. Multi-color imaging is possible by using multiple excitation sources and/or filter sets, so that the probes can be distinguished based on the

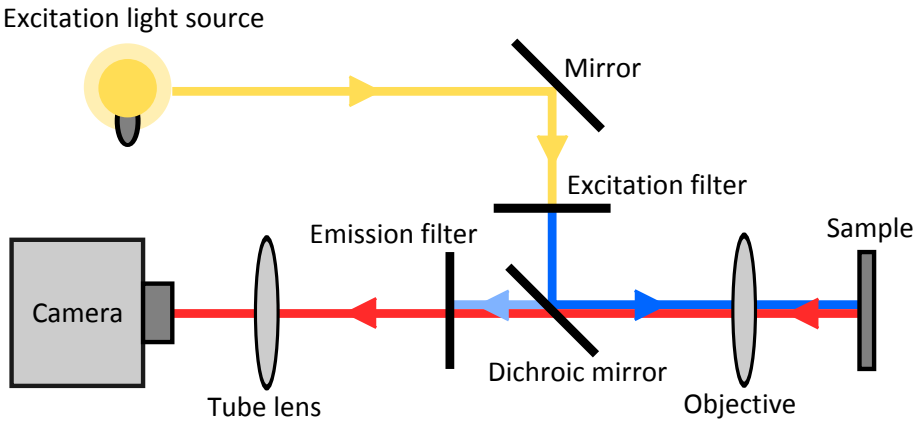

Figure 2.5: *Operational principle of an epi-fluorescence microscope. In the schematic, the broad-band spectrum of excitation light (yellow) is restricted with an excitation filter to remain only relevant wavelengths. The spectrum of filtered excitation light (blue) should match to the absorption spectrum of the employed fluorophore. The excitation light reflects from a dichroic mirror and is focused onto the sample with an objective lens. Fluorescence emission (red) is gathered with the same objective. The fluorescence passes the dichroic mirror, emission filter and is finally focused onto the detector by a tube lens. Additional lens optics may be introduced to collimate the light beams and correct for aberrations.*

excitation and/or emission spectra. To make the multi-color imaging more convenient, so-called multi-band filter sets have been developed, excluding the need of changing the filters between different probes are imaged. Fluorescence filter-sets are commercially available with a penta-pass dichroic mirror and emission filter, i.e. having up to five separate excitation and emission bands [19]. Even a six-color fluorescence image of sub-cellular structures has been demonstrated with a confocal fluorescence microscope with spectral imaging capabilities. A special set of fluorophores were excited with a single laser line and the different emission bands were separated with a diffraction grating and recorded with a multichannel photomultiplier [20, 21].

In the experimental part of this study we mostly employ standard epi-fluorescence microscopy. However, to provide the reader an overview of possible approaches to improve the optical resolution, two more advanced FM techniques are here briefly introduced. These developments eventually paved the way for the development of sub-diffraction limited imaging that will be discussed later in this chapter, and which is the main motivation of our study.

In a wide-field epi-fluorescence microscope, all parts of the specimen in the optical path are excited at the same time and the resulting fluorescence is detected including a large unfocused background part. To solve this problem, a confo-

cal fluorescence microscope was developed which improves the resolution especially in longitudinal (depth) direction. In a confocal microscope, two pinholes are used: one in front of the excitation light source to make it point-like, and the other one in front of the detector (typically a photomultiplier tube). Point-like source can be focused tighter on the sample and the pinhole in front of the detector is used to eliminate the out-of-focus signal [12]. Because only one spot can be imaged at a time, confocal microscopes need to raster scan the sample to construct a complete image. Laser-scanning confocal fluorescence microscopes are commercially available to produce real 3D-images of the sample.

Two-photon excitation (TPE) fluorescence microscopy is another well-know technique to improve resolution in the FM. The TPE microscopy is particularly advantageous method in imaging thick biological samples as it can image structures up to 1 mm deep in the specimen [22, 23]. It is based on the fact that the two-photon excitation rate is proportional to the light intensity squared, as the regular one-photon excitation is directly proportional to the excitation light intensity. Therefore, the excitation volume can be restricted very near to the focus of a Gaussian laser beam, enabling axial sectioning of the sample even without the detection pinhole. Excitation is done with a laser having a wavelength that corresponds to approximately half of the energy gap between the HOMO and the LUMO, such that two photons need to be absorbed at the same time. Because the multi-photon excitation rates are generally very low, relatively high laser powers or short pulses are required to obtain high enough intensities in the focus [12].

2.2.2 Fluorescent probes

Now when we understand how the fluorescence microscope operates, we can discuss a bit more about the probes for fluorescence imaging. The fluorescent probes are prepared to chemically bind in certain sites in the biological structure. In the case of genetically encoded fluorescent proteins, the binding is provided by direct covalent bonding. With other types of fluorescent probes, such as organic dyes, quantum dots or fluorescent microspheres, binding is provided by functional groups. The latter is applied in affinity-based immunolabelling, where binding of the probes to desired targets is assisted by antibodies [24]. Surface functional groups can be just hydrophilic polymers containing multiple carboxylic acids absorbing almost any protein [16], but they also include proteins such as streptavidin which enables a well-known covalent bonding of strepta-

vidin and biotin. The fluorescent microspheres used in this study are surface modified with streptavidin [25], which enables their use with biotin conjugated antibodies without any additional preparation.

The choice of fluorescent probes is generally made based on their absorption and emission spectra, the quantum yield and the binding possibilities. Moreover, in certain FM methods some specific fluorophore properties might be needed, such as photoswitchability (see Section 2.6). The most well-known fluorophores in biological imaging include, e.g., Fluorescein, Cyanine and Rhodamine dyes, Alexa Fluor dyes, and recently developed green fluorescent protein (GFP) and its variants. The GFP was originally derived from jellyfish exhibiting biological fluorescence [16]. More photostable and complementary new dyes and fluorescent proteins are constantly under development, but also other types of fluorescent markers attain a lot of attention. The most prominent of those are solid-state quantum dots because of their easy tunability and, indeed, photostability under intensive illumination.

Fluorescent probes can be engineered by synthesizing artificial new fluorescent chemical compounds and even combining several different fluorescent molecules. This has been done in the fluorescent particles used in this study (TransFluoSpheres 488/645, Molecular Probes) [25]. In these particles, two or more fluorescent molecules are linked inside the particle producing an exceptionally large Stokes shift of more than 150 nm. The complexity of the transitions and molecular states taking part to the fluorescent process is assumed to partly explain the exceptional behaviour of their photobleaching in vacuum (see Chapter 6). Unfortunately, more detailed information of the actual dyes in our fluorescent particles is not available.

2.3 Optical resolution

Optical resolution determines how fine details can be resolved in the optical image. In other words, the resolution is a measure of the ability to distinguish two separate point-like objects from a single object. Optical resolution depends on the quality and instrumentation of the optical system, such as the numerical aperture (NA) of the objective lens. The resolution is limited by the diffraction of light waves due to the finite apertures.

2.3.1 Diffraction limit of light

Let us first introduce the point-spread function (PSF). The point-spread function is a fundamental measure of the resolving power of an optical imaging system, which can be used to define the resolution. The narrower the PSF, the better the resolution. The PSF basically defines the three-dimensional (3D) intensity distribution into which the image of an ideal point source spreads in the system. A point source refers to an infinitely small object in space which can be mathematically expressed with a delta function. According to the classical Fourier transform, or the Heisenberg uncertainty principle in quantum mechanics, a perfect localization in space results in an infinite spectrum of spatial frequencies. However, only a limited range of spatial frequencies can be transferred to the far-field, as propagating electromagnetic waves, and higher frequencies only exists as evanescent waves in the near-field. An evanescent wave here refers to an electromagnetic wave, of which intensity decays exponentially from the source and therefore does not propagate or transfer energy (information). Because some of the information is lost, it is impossible to reconstruct a perfect image of the point-source and the image always has a finite size [12]. This sets the fundamental diffraction limit for all optical imaging. The point-spread function is broadened further by the diffraction in the optical imaging system with a finite aperture, which in the end determines the diffraction limit for the corresponding system.

The point-spread function in xy–plane, perpendicular to the direction of light propagation, produces a spatial intensity distribution called the Airy disks, which is basically the diffraction pattern of a circular aperture. The resolution of an optical system can be defined as the radius of the 1st Airy disk. This is called the Abbe diffraction limit, and it is given by [26, 27]

$$\Delta_{x,y} = \frac{\lambda}{2nsin\,\theta}, \tag{2.6}$$

where λ is the wavelength of light and $nsin\,\theta$ the NA, θ being the half-cone angle of the focused light produced by the objective, and n being the refractive index of imaging medium. This equation holds for lateral resolution (x, y), but because the 3D point-spread function is an ellipsoid, the axial resolution is different. The axial resolution can be derived by [27]

$$\Delta_z = 2\frac{\lambda}{\mathrm{NA}^2}, \tag{2.7}$$

which can be obtained in confocal microscopy where out-of-focus signal is eliminated. It follows that for the green light $\lambda = 550$ nm, with a high numerical aperture $\mathrm{NA} = 1.4$, the diffraction limit is around 200 nm in the lateral directions and 500 nm in the axial direction.

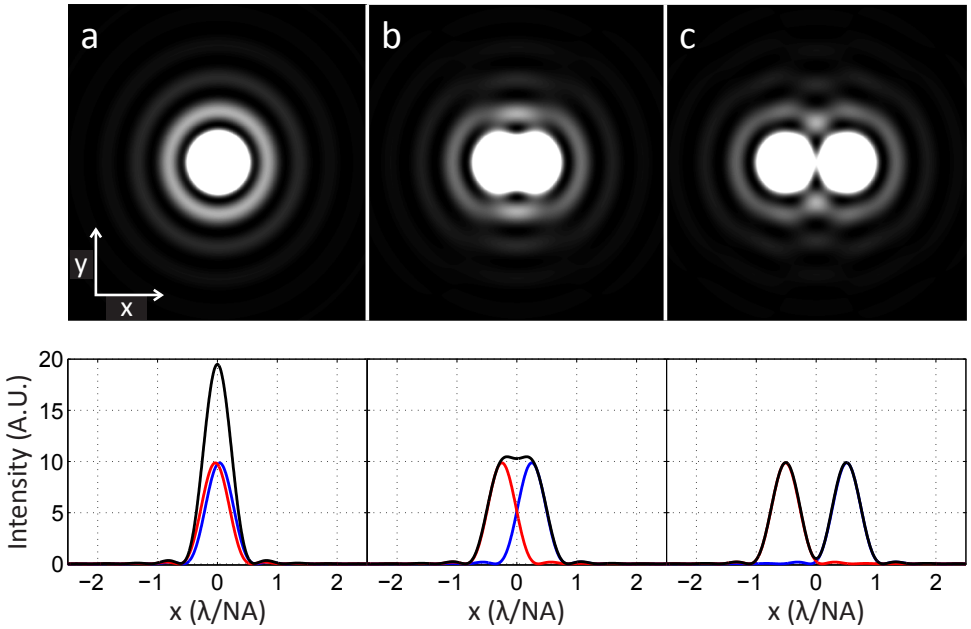

Figure 2.6: *Illustration of the Abbe diffraction limit of light. In (a)-(c), theoretical PSF of two ideal point-sources is show with increasing distance of each other. On the top row, the two-dimensional PSFs are plotted in gray scale, the scale being adjusted to enhance the brightness of the outer rings of the Airy pattern. On the bottom, cross-section of the intensity distribution is taken for each case along the x-axis ($y = 0$). Black curves show the total intensity, which is a sum of the red and blue curves, showing the individual PSFs. In (a), the two point-sources are almost overlapping (separation distance of 0.07·λ/NA). In (b), the point-sources are exactly at the distance of Abbe resolution limit (0.5·λ/NA). The PSF is elongated and a slight bump starts to appear in the middle of two separate peaks. In (c), the two objects are clearly separated (1.02·λ/NA). The figures were produced with a MATLAB script.*

The Abbe resolution limit is illustrated in Figure 2.6 with the PSFs of two ideal point sources. As can be seen, the definition of resolution is not unambiguous. One could claim already before the situation in Figure 2.6b that the elongated image clearly consists of more than one point-source. That is true, but before obtaining the situation in Figure 2.6b, we cannot say for sure that the image consists of exactly two point-sources. In contrast, even in Figure 2.6b, the points are not yet clearly separated, which finally occurs when moving on towards the situation in Figure 2.6c. The Abbe resolution limit is a good approximation for the

attainable optical resolution if no prior knowledge of the sample is available. If we know the exact PSFs of the underlying objects, e.g. that the image consists of only two point-like emitters, we can in most cases de-convolute the image and distinguish the objects in much closer proximity than the Abbe limit. However, then we are not limited by diffraction any more. In general, this kind of prior information is impossible to obtain, but some of the superresolution methods are actually based on the localization of individual fluorophores by exciting them one after the other.

There are possible means of pushing the diffraction limit further by modifying the PSF of the imaging system. The PSF is actually elongated in the axial direction because light is collected only from one side of the sample. Hence, a lot of light, i.e. optical information is actually lost. One can imagine that if the objective could cover the full spherical angel, the PSF would be symmetric in all three dimensions. In principle the light could be collected from both sides of the sample, increasing the effective NA, which is the approach taken in so-called 4Pi and I^5M microscopy, where two opposing objectives are used for excitation and/or detection. The combination of I^5M and so-called structured-illumination microscope has been shown to achieve better than 150 nm resolution in both lateral and axial directions, simultaneously [28]. However, this starts to be on the ultimate border of diffraction limited imaging. Despite the significant technical improvements, the diffraction barrier still limits us to the optical resolution approximately two orders of magnitude away from the molecular scale, the scale we desire to reach in biological imaging. Thus, superresolution techniques are needed.

Even though the diffraction limit is fundamental, it can be overcome with various means. One way of beating the diffraction barrier is to go close and record the electric field distribution in the near-field, which includes also the higher spatial-frequency components. This can be done by applying near-field scanning optical microscopy (NSOM), where 20–50 nm resolution has been achieved. In the NSOM, a sharp probe tip is scanned over the sample which converts the evanescent fields to propagating waves, e.g. inside an optical fiber. In addition, a wide-field near-field imaging has been demonstrated with a so-called superlens, with negative refractive index [29]. The near-field techniques, however, suffer from one major drawback in biological imaging. The near-field region extends only a few tens of nanometers from the corresponding features, which makes it impossible to image anything further below from the surface, e.g. inside the cell.

Therefore, far-field superresolution techniques are required to maintain the flexibility of optical microscopy. Various far-field superresolution techniques have indeed been developed, which are introduced below.

2.3.2 Localization

In contrast to resolving two point sources in close proximity, localization of a single emitter can be done much more precisely than actual resolution of the optical system. Localization refers to the accuracy with which the position of an object can be defined. The image of a point-source is, in principle, a symmetrical point-spread function which can be approximated with a Gaussian. A two-dimensional Gaussian function can therefore be fitted to the intensity distribution of the image. Data produced by N photons can be seen as N measurements of the fluorophore position. As photons follow the Poisson statistics, the localization precision can be approximated by [29]

$$\Delta_{loc} \approx \frac{\Delta}{\sqrt{N}}, \tag{2.8}$$

where Δ_{loc} is the localization precision and Δ is the size, i.e. the full-width half-maximum of the PSF. However, it must be emphasized here that to achieve localization precision of such, prior knowledge of the fluorophore distribution is needed. It must be known that only single object is located in the diffraction limited spot, otherwise the localization cannot be trusted. Localization of single fluorophores is the basis of some of the superresolution techniques introduced below.

2.4 Superresolution techniques

Superresolution stands for an optical imaging resolution beyond the diffraction limit of light. Superresolution cannot be obtained with purely optical methods but additional factors are required, in particular, the involvement of the photophysics or photochemistry of fluorophores.

The main goal of this Master's thesis project is to develop a novel optical superresolution method based on electronbleaching in the SEM. However, several superresolution techniques already exist, of which examples are introduced in this section. The superresolution techniques can be generally divided in two main categories: 1. techniques that employ non-linear effects to sharpen the point-spread

function of the microscope, and 2. techniques that are based on the localization of individual fluorescent molecules. The operational principle with the advantages and limitations of each technique is discussed below.

The resolution achieved with these advanced imaging methods can be well below the diffraction barrier, revealing three-dimensional biological structures at the scale of tens of nanometers. However, none of these techniques has been yet shown to work in an integrated system, such as the SECOM platform. Thus, many difficulties considering correlative imaging still show up, which could be overcome with our complementary approach of utilizing electronbleaching.

2.4.1 Non-linear effects to sharpen the PSF

One approach to attain the optical superresolution is to introduce sub-diffraction limit features in the excitation patter. We refer to this approach as spatially patterned excitation which employs reversible saturable optical fluorescence transitions (RESOLFT), i.e. non-linear saturation effects of excitation/emission of fluorophores. The first realization of RESOLFT microscopy was stimulated emission depletion (STED) microscopy, first proposed in 1994 [30] and subsequently demonstrated experimentally [31].

The operational principle of the STED is summarized in Figure 2.7. The configuration consists of two pulsed lasers, from which one is used for excitation and the other one, i.e. the STED laser, is used to produce stimulated emission of fluorophores. There is a short delay between the excitation pulse and the STED pulse such that the vibrational relaxation of the fluorophores has time to complete. The depletion laser has a longer wavelength than the excitation (see Figure 2.7a,b). The foci of the excitation and STED laser is made to overlap, and the focal region of the STED beam is engineered to have a donut shape with zero-intensity in the middle. Therefore, the STED laser depopulates the excited state of fluorophores everywhere else than in the geometrical center of the excitation beam.

The spatial pattern of the STED laser focus is diffraction limited but the key to achieve superresolution is the saturation of the depleted population, i.e. stimulated emission: If the local intensity of the STED laser is higher than a certain level, essentially all spontaneous fluorescence emission is suppressed. Therefore, the region in where fluorescence occur can be made much smaller than the diffraction limit of light. In other words, the effective PSF of the excitation beam is reduced, as can be seen in Figure 2.7c. In principle, the PSF could be made ar-

bitrarily narrow but its size is limited by practical power level of the STED laser still keeping the zero-intensity in the middle. Fluorescent probes are preferred having high photostability and a large stimulated emission cross section, with a substantial red-shift compared to excitation wavelength. The specific requirements of fluorophores and relatively complicated setup are the main limitations of the STED method. In addition, photobleaching becomes a significant issue under high intensities of the depletion laser, as often $>10^9$ W/cm^2 is required. With STED microscopy, researchers have obtained spatial resolution of 30 nm [29].

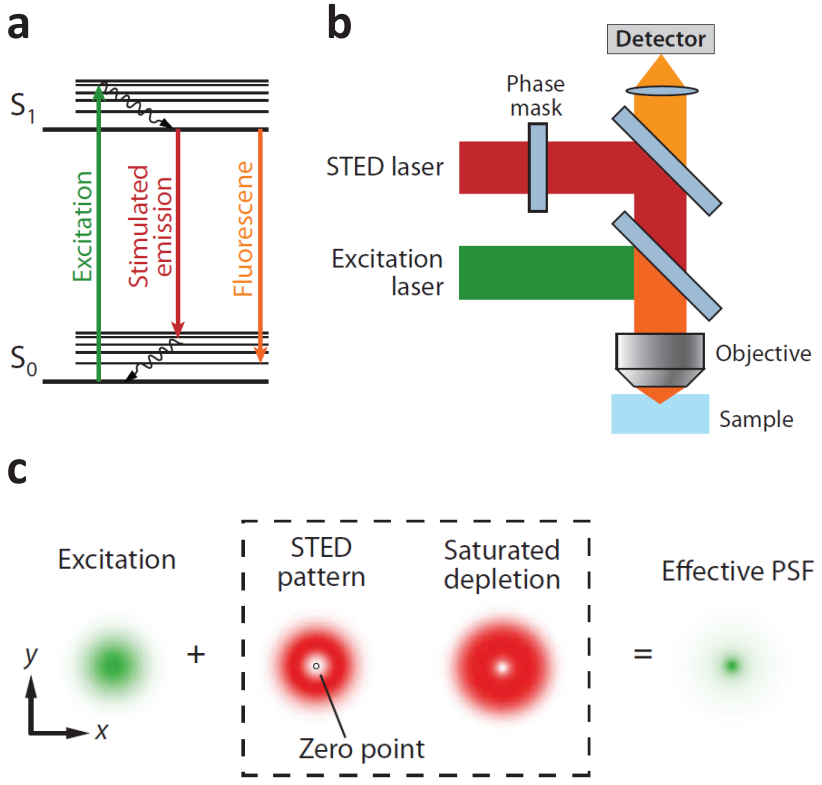

Figure 2.7: *Operational principle of STED. The figure is a modified version of the one in [29].*

Other superresolution techniques based on the RESOLFT have been developed as well, such as ground state depletion (GSD) microscopy and so-called saturated structured-illumination microscopy (SSIM). In contrast to the STED, the GSD microscopy employs fluorescent probes that can be reversibly switched to a long-lived dark state, e.g. triplet state, depleting the ground state and therefore spatially suppressing the excitation/fluorescence. The GSD microscopy benefits from the fact that the depletion laser can have much lower power level than in the STED. Optical resolution better than 100 nm has been obtained at a deple-

tion laser intensity of 600 W/cm^2, employing photoswitchable fluorescent proteins [32].

2.4.2 Localization of individual fluorophores

The diffraction limit of light does not limit the localization precision of a single fluorescent molecule because the image of the molecule is a spatially symmetrical point-spread function. The precision can be approximated with Equation 2.8, and accuracy down to 1 nm has been demonstrated with fluorescent molecules under ambient conditions [29]. Consequently, it is logical to think of an optical superresolution method based on localization of single molecules. Here, we introduce the three methods demonstrated in 2006, all of which were developed independently but are based on the same principle idea of single-molecule imaging. These methods are: photoactivated localization microscopy (PALM) [33], stochastic optical reconstruction microscopy (STORM) [34] and fluorescence PALM (FPALM) [35].

PALM, STORM and FPALM all utilize photoswitchable fluorescent probes which can be switched between fluorescent and dark state. Furthermore, the activation should be possible by a wavelength different from the excitation light. In this approach, molecules within a diffraction-limited region can be activated at different points in time so that they can be individually imaged, localized, and subsequently deactivated. The process consists of a series of cycles during which different subsets of the fluorophores are separately activated and imaged. During each cycle, the density of activated molecules must be kept low enough such that the diffraction limited spots of individual molecules can be clearly resolved in the optical image. This is necessary as the localization of a single fluorophore is accurate only if the images of the fluorophores do not overlap.

In the beginning of the imaging process, the fluorophores are in a dark state. Each cycle starts by the activation of a subset of probes with activation laser with shorter wavelength that the excitation. The activated fluorophores are imaged as long as they are deactivated by the excitation laser itself. The density of activated fluorophores is controlled with the activation laser intensity and/or pulse duration. This procedure is run over and over again till a desirable amount of fluorophores are imaged. The locations of individual fluorophores is calculated by fitting two-dimensional Gaussian function to the FM images and finally, the superresolution image is reconstructed by overlaying all the frames. A demonstration of the power of superresolution imaging compared to conventional diffraction-

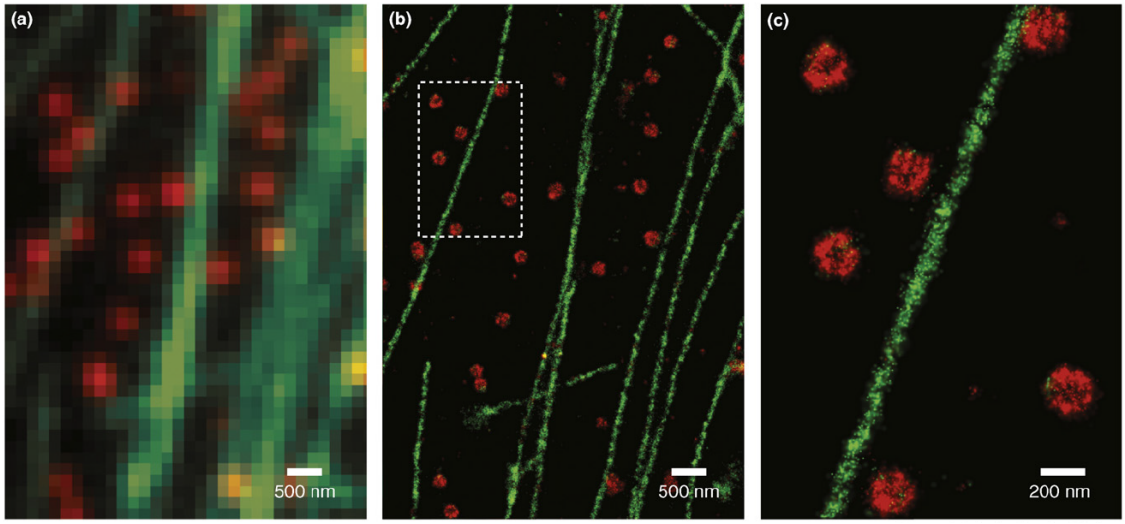

Figure 2.8: *Demonstration of the optical superresolution. Comparison of a two-color conventional diffraction limited FM image of microtubules and clathrin-coated pits in a mammalian cell (a), and the superresolution STORM image of the same area (b). Combined Cy2 and Alexa 647 probes were used to label microtubules, Cy3 and Alexa 647 to label clathrin. The 457 nm and 532 nm laser pulses were used to selectively activate the two pairs, and emission of the reporter dye Alexa 657 was recorded using a single color channel. Each localization is false coloured according to the following code: green for 457 nm activation and red for 532 nm activation. A further magnified view (c) of the boxed region shown in (b). The figure is from [36], and original data from [37].*

limited FM is shown in Figure 2.8.

The main difference between the STORM and PALM/FPALM is the choice of fluorescent probes and the details in their activation/deactivation. In general, the STORM employs reversibly photoswitchable probes that can be activated and deactivated up to hundreds of times. In contrast, PALM/FPALM employs probes that are simply photobleached after imaging and therefore transferred irreversibly to a non-fluorescent state. The STORM uses a pulsed laser to activate fluorophores, but in PALM/FPALM also the activation laser is usually one with a continuous-wave mode. Furthermore, STORM is mostly used with immunolabelling as it requires probes with reversible photoactivation property, which is mostly obtained by combining two different fluorophores: so-called reporter and activator fluorophores (see Figure 2.8). Because of reversibly photoswitching, STORM has a huge potential in time-resolved fluorescence imaging. PALM/FPALM are mostly used with fluorescent proteins and is therefore applicable also for studies with genetic labelling of cells *in vivo*. However, also reversibly photoswitchable fluorescent proteins have been recently developed [29].

Superresolution techniques that employ the localization of individual fluorophores are one of the most recent developments on the area of optical superresolution, and researchers are currently heading to the ultimate goal of molecular resolution. Even very dense samples of fluorescent probes can nowadays be resolved with a spatial resolution on the order of 20 nm. In principle, an arbitrary high resolution would be possible, but it is limited by the number of photons detected per fluorophore. These methods improve the optical resolution more than one order of magnitude, at the same time retaining the most important applicabilities of fluorescence microscopy, including three-dimensional live-cell imaging. However, the photophysical and photochemical properties of fluorescent probes are critical and very particular. Moreover, superresolution techniques based in single-molecule imaging are rather time consuming, and the non-fluorescent ultra-structure still remains hidden.

2.5 Correlative light-electron microscopy

Correlative light-electron microscopy with a novel optical superresolution method is the central topic of this thesis. To understand the CLEM, we first need to discuss the operational principle of a scanning electron microscope (SEM) which is the EM used in this study. After that, we will discuss the correlative imaging, the conventional way of performing it, and an integrated system with its advantages. Finally, we summarize the essence of the chapter, taking an approach towards realization of optical superresolution in the CLEM.

2.5.1 Scanning electron microscopy

In an electron microscope (EM), the sample is illuminated with electrons instead of light (photons). Like in a light microscope (LM), the resolution of an EM is limited by the diffraction, but the de Broglie wavelength of an electron is much shorter than the wavelength light. Hence, the fundamental limit of resolution is far beyond the diffraction limit of light, and electrons can carry information of much finer details. The de Broglie wavelength of an electron is given by

$$\lambda = \frac{h}{p} = \frac{h}{\sqrt{2m_e eV_a}}, \tag{2.9}$$

where h denotes the Planck's constant, p the electron momentum, m_e the electron mass, e the elementary charge and V_a the acceleration voltage in the EM. With a

typical acceleration voltage of $V_a = 10$ kV, the electrons have a de Broglie wavelength of approximately 10 pm. However, in a scanning electron microscope, the diffraction limited imaging cannot generally be reached because other factors limit the resolution to the order of a nanometer. Nevertheless, nanometer resolution is already two-orders of magnitude better than that of the conventional light microscope. Figure 2.9 shows an SEM images of the same biological tissue section imaged with a confocal fluorescence microscope in Figure 2.4. The difference in the resolution, and details present, is tremendous.

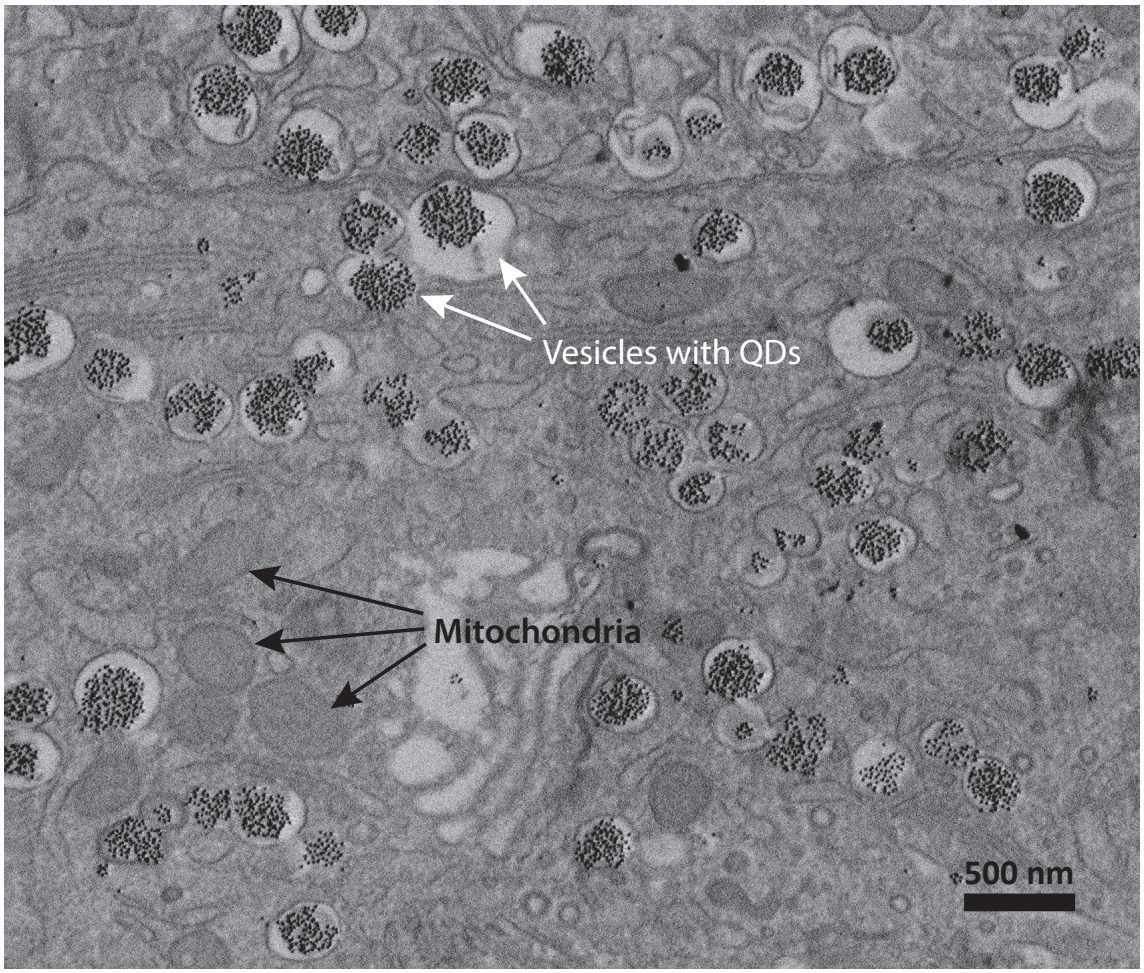

Figure 2.9: *An SEM image of the same quantum-dot labelled diabetic-rat pancreas-tissue as imaged with a confocal fluorescence microscope in Figure 2.4. The SEM image reveals the specimen ultrastructure at nanometer scale resolution. Here, the contrast is inverted and individual quantum dots can be seen as black spots labelling insulin-containing vesicles, indicated with white arrows. The labelling here is exceptionally dense. The quantum dots have a nominal diameter of approximately 10 nm.*

The SEM consist of two main parts: an electron column, which generates and controls the incident electron-beam, and the detection side, which records and reconstructs a topographical gray scale image of the sample. A simplified illustration of an SEM is shown in Figure 2.10. The SEM column consist of an electron gun (electron source), electron lenses, apertures and scanning coils. The electron lenses modify the electron wavefunction with electromagnetic fields, and focus the electron beam onto the sample. Apertures are used to limit the electric current and energy spread of the beam. The scanning coils can deflect the electron-beam and therefore control the beam position on the sample. The scanning coils are used to scan the sample surface with discrete spots (pixels) with an adjustable step size.

Once an electron hits the sample, it scatters through the material in a complex manner generating secondary electron (SE) and other secondary products, such as heat, cathodoluminescence and X-rays. The SE yield depends on the injected primary electron (PE) dose, the electron landing energy and certainly the material parameters. Secondary electrons are generated through inelastic scattering in the specimen, when an incident electron excites a constituent atomic electron above the vacuum level, basically ionizing the atoms. As the SEs have relatively low kinetic energy (<50 eV), those generated deep within the interaction volume are quickly absorbed. Only SEs produced near the surface, typically in a few nanometer thick layer, are able to diffuse to the surface and leave the specimen [38]. A primary electron can also leave the sample as a backscattered electron (BSE) if it does not dissipate all of its energy in the scattering process. The electrons exiting the specimen can be selectively detected according to their energy spectrum (c.f. SE and BSE detection). More detailed discussion of the electron-matter interaction, and the various scattering events taking place, can be found in Chapter 3, in discussing of the electronbleaching of fluorescent molecules.

The SEM image is reconstructed by monitoring the electron emission signal of the sample during which the electron beam scans over it pixel by pixel. The amount of escaping secondary and/or backscattered electrons of each pixel is recorded by the detector. Because we can only detect the SEs and/or BSEs that are produced within the exit depth of a few nanometers from the surface, the final result is an image of the sample surface. The detected SE yield depends strongly on the topography of the sample because increasing incident angle increases the path length of the primary electrons inside the exit depth, thus increasing the

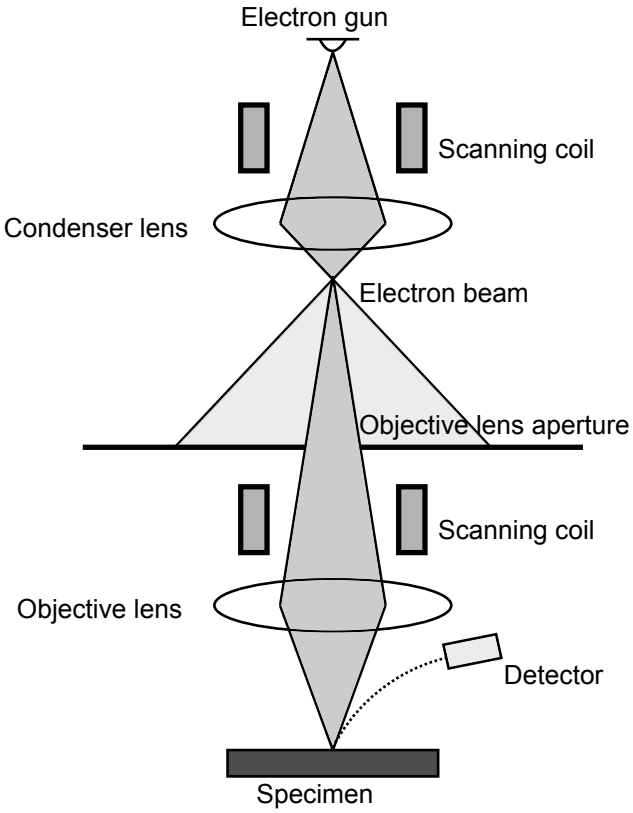

Figure 2.10: *Simplified illustration of an scanning electron microscope.*

SE emission. Here, normal incidence is considered the zero-angle. The variation in the detected SE yield provides contrast in the image. Sharp edges form additional image contrast because their large surface area compared to the interaction volume also increases the SE emission rate. The detected BSE yield depends generally more on the atomic structure of the specimen, that is, the electron collisions with heavy atoms produce more BSEs than collisions with lighter atoms. BSE detection is widely used in biological imaging as it provides a good contrast especially with heavy-metal stained specimens.

The most important parameters in the SEM are the acceleration voltage (e-beam energy), electric current and the dwell time, which is the time e-beam spends on each pixel. The electron dose per pixel is defined as a product of electric current and dwell time. The resolution of an SEM is determined by the size of the region from which the signal originates, which is interrelated to the electron-beam spot-size on the sample. It is easier to form a tighter focus (smaller spot size) at higher beam energies because the degrading effects of chromatic aberration of the system are relatively less significant. This is because of a smaller relative en-

ergy spread of the beam electrons. The downside of higher beam energies is that the incident electrons penetrate deeper and scatter more widely within the specimen, generating signal from locations well outside the focal spot. With modern SEMs, however, an electron-beam spot-size of less than 1 nm is nowadays achievable even at low beam energies, by reducing the relative energy spread with a monochromator for the electron beam. For FEI Verios 460, the SEM employed in this work, a sub-nanometer resolution has been demonstrated with acceleration voltages below 1 kV [39]. Besides the signal generation volume, the final resolution depends also on the noise and contrast of the image. The noise is mostly shot noise in nature, and can be reduced by increasing the electron dose (electric current and/or pixel dwell time), thus increasing the total signal level.

In the SEM, the sample needs to be conductive to prevent charging effects, such as distortions of the SEM image and the radiation damage of an organic specimen. The radiation damage is proportional to incident charge density [38] which piles up if the sample is not conductive. Therefore, biological specimens are usually placed on a conductive substrate, e.g. indium-tin-oxide coated glass slide, or even coated with a few nanometer thick metal film. Even in the EM, biological specimen often exhibit contrast so poor that staining is required. Particular molecules can be labelled with metal nanoparticles, and a complete tissue can be stained with heavy-metal compounds, such as Osmium tetroxide. So-called dual-contrast probes, showing up in both LM/FM and EM, are very interesting and also important for correlative imaging. However, fluorescent probes combined with metal nanoparticles do not really work because metal particles completely quench the fluorescence emission. Moreover, for practical applications the probes should not be very large to minimize their effect on the behaviour of the target molecules. Most promising dual-contrast probes are currently semiconductor quantum dots, typically size of 5-10 nm, exhibiting very bright emission and good contrast in the EM.

Low acceleration voltages of 1–5 kV and BSE detection are usually preferred in biological SEM imaging because that provides the best image contrast. Moreover, around that energy range for insulating materials, there is an optimal beam energy at which the total electron emission yield σ_{tot} per injected primary electron becomes equal to one ($\sigma_{tot}/PE = 1$), implying no charging of the specimen [38].

To conclude, the SEM provides a spatial resolution at nanometer scale and can therefore be employed to resolve the specimen ultra-structure in near-molecular

level. Albeit the superior resolution compared to the conventional optical microscopy, the SEM image is lacking some invaluable information present in the FM image, that is, the functional information. The fluorescent probes do not necessarily light up in SEM image and even with the promising dual-contrast probes, two quantum dots of similar sizes but with different emission colors cannot be distinguished in the SEM image. Furthermore, tracking of rare events can be very hard, sometimes even impossible [40]. Therefore, the SEM and the FM must be seen as complementary techniques, which of course can be combined.

2.5.2 Correlative imaging

The basic idea of correlative light-electron microscopy (CLEM) is to combine the information acquired with both the LM and the EM, in order to obtain a more comprehensive picture of the specimen. The biological functions show in the FM image, and the ultrastructure of the sample can be revealed with the electron microscope. Figure 2.11 shows an example of correlative imaging where an FM image overlaid with an SEM image of a biological tissue.

The conventional way of performing CLEM is to image the sample with two separate microscopes which has, however, several drawbacks. The main drawback is the lack of flexibility because one just cannot easily move back and froth between the two microscopy techniques. Moving between two separate systems is time consuming and the sample gets vulnerable to contamination and damage. First of all, it is difficult to find the exact region-of-interest when moving the sample to another system. When the ROI is found, e.g. with a help of dual-contrast markers, the overlay accuracy of the images may still be poor, or at least advanced coordination transformations are needed.

To overcome the difficulties pointed out above, an integrated light-scanning electron microscope has been developed in our research group of Charged Particle Optics. This integrated system called SECOM platform enables the flexibility to change between the LM and EM while the sample is kept on the spot. This is extremely convenient in practice, and makes the inspection much faster than with two separated systems. Moreover, the overlay accuracy of the FM and SEM images is highly improved because the FM coordination systems can be directly aligned to that of the SEM, with a help of cathodoluminescence of the substrate. The SECOM platform is introduced more in detail later in Chapter 5.

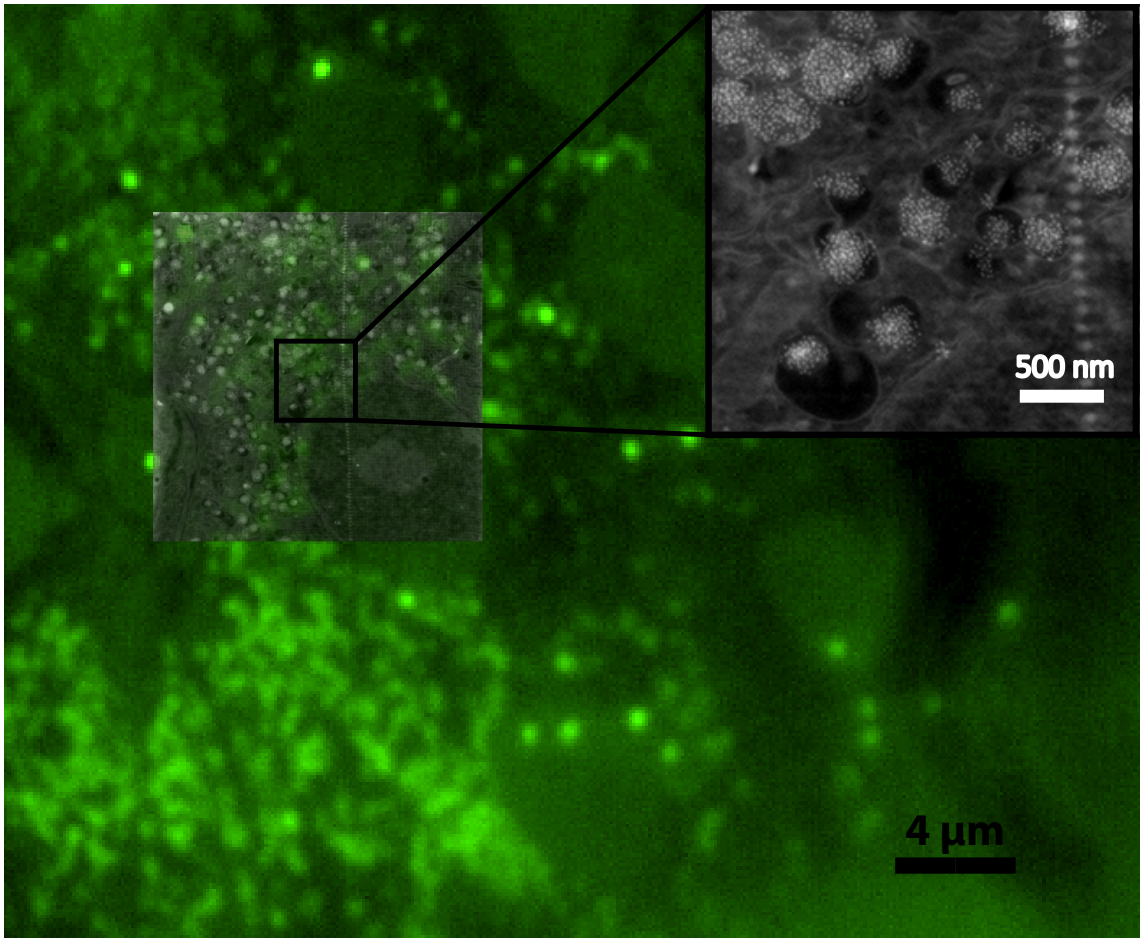

Figure 2.11: *Overlay of the FM and SEM image of the quantum-dot labelled diabetic-rat pancreas-tissue already introduced earlier in Figures 2.4 and 2.9. The SEM image reveals the specimen ultrastructure in nanometer scale resolution. Individual quantum dots can be seen as white spots in the SEM image and bright diffraction limited fluorescence spots in the FM image. In contrast to the confocal FM image in Figure 2.4, only one color channel is now in use. Thus, the quantum dot emission cannot be separated from the nucleic acid stain of the tissue, and the fluorescence intensity in the image is represented neutrally in green color scale. The overlay image is acquired with the SECOM platform. The inset shows a zoom-in of the SEM image.*

To summarize the chapter, we have seen how important fluorescence microscopy is for life sciences, what is the basis of fluorescence and what is the operational principle of fluorescence microscope. We have discussed the diffraction limit of light which sets a fundamental limit for the resolving power of a conventional light microscope. This diffraction barrier was thought to be unbreakable but the development in the past three decades has brought us many different means to actually overcome it. Optical resolution far beyond the diffraction limit of light has been demonstrated with various superresolution techniques. Resolu-

tion down to ∼20 nm has been obtained, so it is justifiable to ask: Why are we developing yet another superresolution method? The answer to this key question is the correlative light-electron microscopy. All superresolution techniques are only complementary to the electron microscopy which can reveal the entire non-fluorescent ultrastructure of the specimen which does not light up in the FM image. In correlative microscopy the FM and EM images are combined to provide more comprehensive understanding on the biological actions, and where they are located within the ultrastructure.

All existing superresolution methods have certain limitations: either very high laser powers are required (STED) or very specific criteria restrict the fluorophores to be used (STORM, PALM). High laser powers cause troubles with photobleaching, and they might cause additional problems under vacuum conditions, such as sample heating, which can become a huge problem especially for cryo-imaging. Moreover, in an integrated system, fluorescence must be maintained in the vacuum. Our novel superresolution method could in principle work with any type of probes such as standard organic dye molecules, and with any kind of labelling method. What is more, the FM and SEM images are simultaneously acquired in the same coordinate system, providing intrinsically a perfect overlap between the two images.

CHAPTER 3

Bleaching of fluorophores

This chapter discusses the bleaching phenomena of fluorescent molecules. I first cover the physical basis of photobleaching, and further on that of electronbleaching, which both are of great importance for this study. Photobleaching is generally an undesired phenomenon which reduces the fluorescence signal of the sample in fluorescence microscopy. Photobleaching takes place after a certain amount of fluorescent cycles, once the fluorophore transfers irreversibly to a non-fluorescence state. Photobleaching of fluorophores has been intensively studied in the literature during the past a few decades. However, the mechanisms involved are still not fully understood [41]. The photobleaching studies show some common factors for most fluorophores, and models for bleaching behaviour have been developed. In this chapter, I discuss these common factors and models of photobleaching.

Here, the theoretical discussion of photobleaching also serves as an introduction for electronbleaching which is the key of our superresolution method. I start the discussion of electronbleaching with a brief introduction of electron-matter interaction, namely electron scattering in matter. After that, Monte-Carlo simulations are presented of the electron scattering in the samples used in this work. Finally, I address the most probable mechanisms involved in electronbleaching.

3.1 Photobleaching

Upon repetitive excitation, a fluorophore eventually stops emitting photons, that is, it photobleaches. On the ensemble level, this causes a gradual decrease of the fluorescence signal, whereas on the single emitter level photobleaching yields to

a sudden disappearance of fluorescence.

Irreversible photobleaching occurs through a photochemical reaction from an excited state of the fluorophore, typically from a long-lived triplet state. The main causes of photobleaching seem to involve interaction between the fluorophore and oxygen species [41]. First of all, molecular oxygen (O_2) acts as an efficient quencher for almost all known fluorophores. A particular feature of O_2 is that its ground state is a triplet state, making it paramagnetic. Molecular oxygen therefore increases the chance of a spin flip, i.e. intersystem crossing from excited singlet state S_1 to excited triplet state T_1, where the fluorophore has much more time to interact with its environment. From T_1, the fluorophore may be even further excited to some higher triplet state T_n. In the excited state, the fluorescent molecule has generally a higher chance to react with the surrounding chemical compounds, such as reactive oxygen radicals or other free radicals with a dangling covalent bond. The molecule might bleach due to oxidation or some other charge transfer process, which changes the molecular configuration. A fluorescence cycle with the most common photobleaching pathways is illustrated in Figure 3.1.

Typically bleaching rate is linearly dependent on the excitation intensity, and the variation of excitation power and exposure time has no effect on the total fluorescence yield. The molecules will emit a pre-determined number of photons, independent of the rate at which they are emitted. However, in some cases a nonlinear dependence has been observed, implying a photobleaching mechanism that involves absorption of multiple photons. This has been observed for Rhodamine 6G in vacuum, where the contribution of oxygen has been excluded [42]. Here, low excitation rates yielded prolonged photochemical survival times and unpredicted number of emitted photons per molecule. Indications of two-step photobleaching mechanisms/photolysis have also been seen earlier in [43, 44]. Furthermore, it has been shown that the photobleaching rate can be reduced by using pulsed excitation, with a pulse separation time longer than the triplet state relaxation. This prevents the excitation of the molecule to a further reactive triplet state T_n, as the triplet state has time to relax between subsequent molecular absorption events. For commonly employed fluorescent probes, green fluorescent protein (GFP) and Rhodamine dye Atto532, a 5–25-fold increase in total fluorescence yield has been demonstrated, when strong continuous-wave or high-repetition-rate pulsed illumination is replaced with pulses featuring tempo-

ral pulse separation of >1 μs [45].

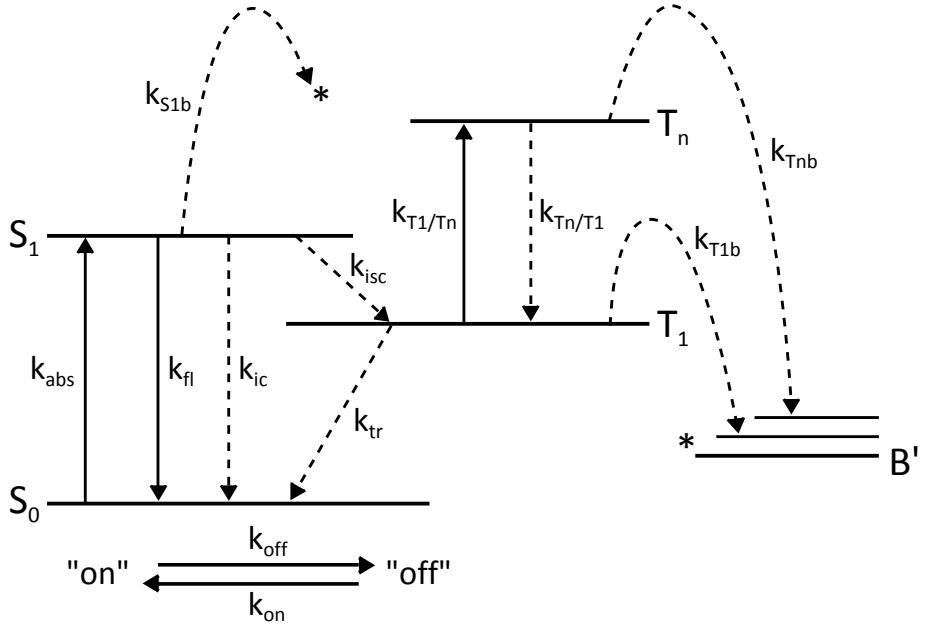

Figure 3.1: *Jablonski diagram of a fluorescent molecule, including photobleaching from several excited states. The photobleaching is illustrated as a transfer to one generic state B, but the actual state can be different for different bleaching processes. Transitions that include a photon absorption or emission are depicted with solid lines, others with dashed lines.*

The dynamics of the fluorescence cycle can be broken down to so-called rate equations. The rate equations describe how the population of different states changes in time. For the fluorescence cycle presented in Figure 3.1, the rate equations can be written by

$$\frac{dS_0}{dt} = -k_{abs}S_0 + (k_{fl} + k_{ic})S_1 + k_{tr}T_1 \tag{3.1}$$

$$\frac{dS_1}{dt} = k_{abs}S_0 - (k_{fl} + k_{ic} + k_{isc})S_1 - k_{S1b}S_1 \tag{3.2}$$

$$\frac{dT_1}{dt} = k_{isc}S_1 + k_{Tn/T1}T_n - (k_{tr} + k_{T1/Tn})T_1 - k_{T1b}T_1 \tag{3.3}$$

$$\frac{dT_n}{dt} = k_{T1/Tn}T_1 - k_{Tn/T1}T_n - k_{Tnb}T_n \tag{3.4}$$

$$\frac{dB}{dt} = k_{S1b}S_1 + k_{T1b}T_1 + k_{Tnb}T_n \tag{3.5}$$

$$1 = S_0 + S_1 + T_1 + T_n + B, \tag{3.6}$$

where B represents a generic state of bleached molecules.

The equilibrium condition can be calculated by setting $\frac{dS_0}{dt} = \frac{dS_1}{dt} = \frac{dT_1}{dt} = \frac{dT_n}{dt} = 0$ and assuming that the bleaching rates k_{S1b}, k_{T1b} and k_{Tnb} are much smaller than all other rate constants [46, 47]. For every bleaching pathway separately, Equation 3.6 can eventually be written with only the population of the generic bleached state B and the population of the state from which photobleaching occurs. For instance, for T_1 it yields

$$T_1 = \left(\frac{(k_{fl} + k_{ic} + k_{isc})k_{tr}}{k_{abs}k_{isc}} + \frac{k_{tr}}{k_{isc}} + \frac{k_{T1/Tn}}{k_{Tn/T1}} + 1 \right)^{-1} \cdot (1 - B). \tag{3.7}$$

Here, we have assumed no photobleaching from other states than T_1. Similar expression can be calculated also for S_1 and T_n. Substituting Equation 3.7 in 3.5, and setting $k_{S1b} = k_{Tnb} = 0$, it yields

$$\frac{dB}{dt} = C_k(1 - B), \tag{3.8}$$

where constant C_k consist of the complex rate constant term. From this it directly follows that the population of bleached molecules through the corresponding bleaching pathway is given by

$$B = 1 - \exp\left(-\frac{t}{\tau_b}\right), \tag{3.9}$$

and the decrease of fluorescence intensity can be described by an exponential decay function

$$I = I_0 \exp\left(-\frac{t}{\tau_b}\right). \tag{3.10}$$

where I_0 is the intensity in the beginning of the measurement, and fluorescence decreases with a decay constant $\tau_b = C_k^{-1}$. Here, we have assumed that photobleaching takes place from state T_1 only, which is a valid approximation if bleaching from state T_1 is predominant. However, if the probabilities of other bleaching processes are comparable, the decay is no more just a single-exponential. In general, photobleaching results to multi-exponential decay whenever multiple bleaching processes are involved, as has been shown in [18]. Photobleaching may also result in a non-exponential decay, as discussed for linear polarized excitation in [46].

Besides irreversible photobleaching, another very important phenomenon can

reduce the fluorescence intensity over the measurement time. That is the intermittent switching between bright and dark states, so-called fluorescence blinking, which is one of the most prominent features of single molecule emission under observation at room temperature [48]. Fluorescent blinking/intermittency is sometimes called reversible photobleaching or photophysical bleaching, which should be discriminate from irreversible photobleaching, referred to as the photochemical bleaching.

Fluorescence blinking occurs in broad range of time scales from microseconds to minutes [49]. Fast blinking processes are typically due to the triplet state bottleneck, i.e. if the molecule is transferred to an excited triplet state, the return back to the actual fluorescent cycle might take time up to milliseconds. In contrast, long lasting "off"-periods cannot be explained just with a triplet state excursion. Long "off"-periods require more complex metastable excited states to occur. For instance, if the fluorescent molecule is embedded in a polymer matrix, a charge transfer might take place between the fluorophore and the surrounding. The electron in the excited state may be transferred from fluorophore to a trapping site in the host matrix. The ejection of the charge is subsequently stabilized by the dielectric response of the matrix, and therefore the depth of trapping potential, and thus the "off"-time duration, is a function of the dielectric constant of the embedding matrix [50]. In addition, it has been proposed that an intermolecular electron transfer may occur in either direction, between the fluorophore and a molecule in the surrounding, thus forming a radical pair [51, 52]. In any case, the metastable state reverts to the ground state S_0 by electron tunnelling.

The durations of "on"- and "off"-times in fluorescence blinking typically follow a slowly-decaying power law distribution instead of an exponential [49, 50, 52–54], which has peculiar consequences. The power law distribution is given by [49]

$$p(\tau_i) = p_0 \tau_i^{-\alpha_i}, \qquad i = on,\ off, \tag{3.11}$$

where τ_{on} and τ_{off} are the durations of "on"- and "off"-times, respectively. Here, α_{on} and α_{off} are the power law exponents, and p_0 is the normalization factor. In contrast to exponential distribution, the power law distribution exhibits so-called statistical aging [53, 55]. It follows that the power law distribution is connected to an increasing duration of "on"- and "off"-times during the observation time. Assuming $\alpha_{on} > \alpha_{off}$, an individual emitter will spend more and more time in the "off"-state, as the measurement continues. For an ensemble of emitters, this effect

appears as gradual decrease of fluorescence intensity over the measurement time, resembling irreversible photobleaching. However, in contrast to regular photobleaching, the decrease of fluorescence due to increasing "off"-periods is fully reversible. Moreover, a situation of $\alpha_{on} < \alpha_{off}$ will result to photobrightening [49].

In Chapter 6, we will see that our fluorescent polymer beads photobleach much faster under vacuum conditions than in the ambient, but only contrary results can be found in the literature, e.g. [42, 47, 56]. However, the photobleaching of the beads in vacuum is observed to be reversible. It might be that the lack of humidity in vacuum drastically increases the lifetime of metastable dark states, as the charge dissipation becomes more difficult. It has been seen that also oxygen reduces "off" periods, as the oxygen may assist the excited metastable state recovery as an electron carrier [52]. It may therefore imply that the very photostable probes in the ambient become unstable under vacuum conditions, undergoing a fast (reversible) photobleaching.

To summarize, irreversible photobleaching typically results in an exponential decay of the fluorescence intensity of an ensemble of fluorophores, as in every cycle each fluorophore has a certain probability to bleach. The bleaching process typically involves a photochemical reaction between an excited fluorophore and an oxygen/other free radical. In addition, fluorescence blinking can decrease the fluorescence signal over time in certain conditions, because the "off"-times of fluorescent molecules become longer during the measurement. This might partly explain the peculiar photobleaching behaviour of our fluorescent polymer beads in vacuum, and recovery of fluorescence in ambient, seen in Chapter 6.

3.2 Electronbleaching

Let us first discuss the electron-matter interaction taking place after an electron-beam hits the sample. An electron that enters the specimen is called a primary electron (PE), typically carrying kinetic energy of >1 keV. The primary electron will scatter in the solid generating various secondary products, that are, secondary electrons (SEs), Auger electrons, phonons (heat) and electromagnetic radiation (X-rays, cathodoluminescence) [38]. Eventually the primary electron dissipates all its energy in the specimen, or leaves the specimen as a backscattered electron (BSE). The secondary products can of course further interact in the solid: especially high-energy Auger electrons and X-rays can generate more secondary electrons, and secondary electrons can induce chemical changes in the structure,

e.g. polymerization in electron-beam lithography and electronbleaching of fluorophores.

The scattering events occur within a restricted volume, called the interaction volume, the size of which depends on the landing energy of incident electrons, and the atomic number and density of the specimen. Scattering processes result in zig-zag trajectories of electrons in solid until the electrons come to rest by gradual deceleration or leave the specimen as BSEs (see Figures 3.2-3.2). The scattering processes can be formally divided in elastic and inelastic scattering.

Elastic scattering originates from the interaction between the incident electron and the nuclei of the specimen. During the elastic scattering, the total momentum and total kinetic energy of the collision partners are conserved. However, the energy loss of the incident electron and the kinetic energy transferred to the nucleus can be neglected since the electron mass is so much smaller than that of the nucleus. Elastic scattering mainly influences electron diffusion and backscattering. Backscattering coefficient, i.e. the ratio (BSE / PE), depends on the atomic number of the material because at heavy nuclei elastic scatter to large angles is more probable that at light nuclei.

Inelastic scattering, on the other hand, originates from the interaction between the incident electron and the atomic jellium (atomic electrons) in the solid. During the inelastic scattering, a fraction of the kinetic energy of the incident electron is transferred to an atomic electron, which can be excited to a higher energy level, and if the transferred energy is larger than the binding energy, the atomic electron can leave the host atom (ionization). If the transferred energy is much larger than the binding energy, the electron-electron collision can be treated as quasi-free, and the dynamics follows so-called Compton scattering. The angular distribution of inelastic scattering is very narrow, which yields that elastic scattering is the main responsible of beam broadening inside the specimen [38].

Inelastic scattering is responsible for the generation of all the secondary products. Auger electrons and X-rays result from inner-shell ionization of the constituent atoms. When an electron on a higher molecular orbital drops down to fulfil the vacancy in the inner-shell, the energy of that electron is released as photon emission (X-ray) or transferred for kinetic energy of another electron in some of the outer electron shells (Auger electron). Binding energies of even more than 10 keV are common for the inner-cell electrons in heavy atoms, such as gold, so if the incident electrons carry enough energy to excite them, also the Auger elec-

trons and X-rays can have energies in that range [38]. In contrast, secondary electrons are generated by ionization of the constituent atoms by excitation of valence electrons. SE energy spectrum typically peaks in the range of 1–10 eV [38, 57]. Cathodoluminescence is analogous to fluorescence but the excitation occurs by an electron instead of a photon. Lastly, phonons/heat is always generated when excitations relax by non-radiative means.

We have applied an open-source Monte-Carlo simulation software (CASINO v2) to study the electron scattering process in the substrates used in this work, namely ITO-coated glass slips and TEM-grids with a 30–60 nm thick Formvar membrane. The samples are discussed in more detail in Sections 4.1 and 5.4. Figure 3.2 presents CASINO simulations for a ITO-glass substrate with landing energies of 1, 3, 5, and 10 keV. The surface area of BSE emission increases significantly with increasing landing energy. Figure 3.3 presents CASINO simulations for 40 nm thick polystyrene layer on top of the ITO-glass substrate, corresponding to the size of the fluorescent polystyrene beads used in the experiments. We simulate trajectories of 10^5 electron to obtain a sufficient accuracy of the electron diffusion in the specimen [38].

Electronbleaching is a complex process, analogous to photobleaching, and no dedicated studies can be found in the literature. Radiation damage of organic molecules have been shown to involve destruction of chemical bonds due to additional local charge in the solid, which is proportional to the incident charge density, i.e. the injected electron dose [38]. Therefore, we can assume that electronbleaching processes involve dissociation of the fluorescent molecule, and/or charge transfer states, followed by chemical reactions that further transfer the molecule to a non-fluorescent state. Molecular dissociation cross-section, which basically defines the probability of the corresponding scattering event, typically peaks at low-energy electrons of 5–50 eV [58–60], implying the secondary electrons to be the main responsible of electronbleaching [60]. In principle, bleaching might also involve cathodoluminescence cycles of fluorescent molecules. Our first approximation is that the fluorescence decay due to electron exposure (as a function of electron dose) follows a single-exponential, which is fitted to the experimental data in Chapter 4.

Bleaching spot-size of the electron beam is always at least the size of the focal spot, but can easily become two orders of magnitude larger due to electron scattering in the substrate. From the Monte-Carlo simulations in Figure 3.2, one

can observe that both the surface area of electron emission and the interaction volume increase with increasing landing energy (shown for BSEs), implying that more out-of-focus bleaching of fluorophores may occur. Figure 3.3 shows the situation including a 40 nm polystyrene layer on top, as with our fluorophore doped nanoparticles. As can be seen in Figure 3.3, at 1 keV landing energy, the interaction volume corresponds to the size of our 40 nm polymer bead meaning that the scattering primary electrons fulfil the whole particle. For beam energies of >1 keV, the interaction volume extends beyond the 40 nm polystyrene layer, and energy starts to be dissipated in the substrate. It suggests, that with higher landing energies, the fluorescent particle is bleached less efficiently in the focus relative to out-of-focus contribution.

In contrast, with decreasing landing energy, reduced surface area of electron emission implies that less out-of-focus bleaching may occur. However, with landing energies of <1 keV, the scattering electrons do not even fulfil the polystyrene particle anymore. Furthermore, secondary electron generation typically peaks at incident-electron energy of 0.3–2 keV for insulators [38]. Thus, we may conclude that a landing energy of around 1 keV should be the most efficient energy to bleach the fluorescent particles (see the results in Section 4.3.3), also providing the best ratio between in-focus to out-of-focus bleaching and therefore the best resolution with which the fluorescent particles could be "switched off".

The experimental study in Chapter 4 will provide further understanding how the electronbleaching rate of our fluorophore doped nanoparticles depends on various electron exposure parameters.

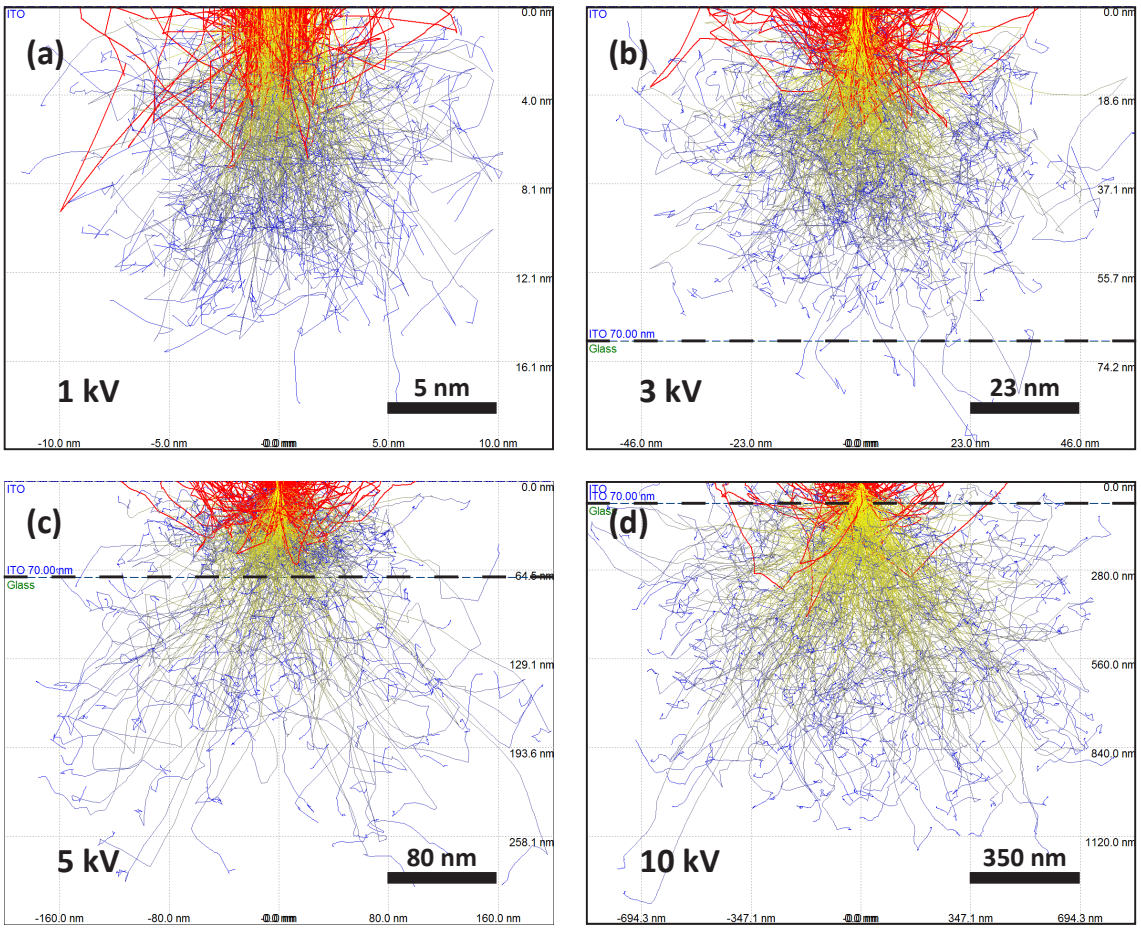

Figure 3.2: *Monte-Carlo simulations of electron scattering in the ITO-coated glass substrate with landing energies of 1, 3, 5 and 10 keV, in (a)-(d) respectively. ITO-coating thickness of 70 nm is used on top. The figures show trajectories of 500 electrons once an electron-beam with a diameter of 3 nm hits the sample. Red lines represent the trajectories of backscattered electrons, and yellow/blue lines the trajectories of electrons that gradually dissipate all their energy in the substrate. The color scale from yellow to blue represents the electron energy along the trajectory. Dashed black horizontal lines indicate the ITO–glass interface. The interaction volume changes rapidly as a function of electron landing energy, as well as the surface area from which the BSEs exit the sample. In (c), the figure nicely shows how the density of the material affects the diffusion of electrons. That is, electrons diffuse much greater distance in glass. Here, the density of ITO is 7.14 g/cm^3 and that of amorphous quartz glass 2.203 g/cm^3. Chemical configurations of $In_{18}SnO_{29}$ and SiO_2 were used for ITO and glass, respectively. The simulations are performed with CASINO v2, which is an open-source simulations software for backscattered electrons in solids.*

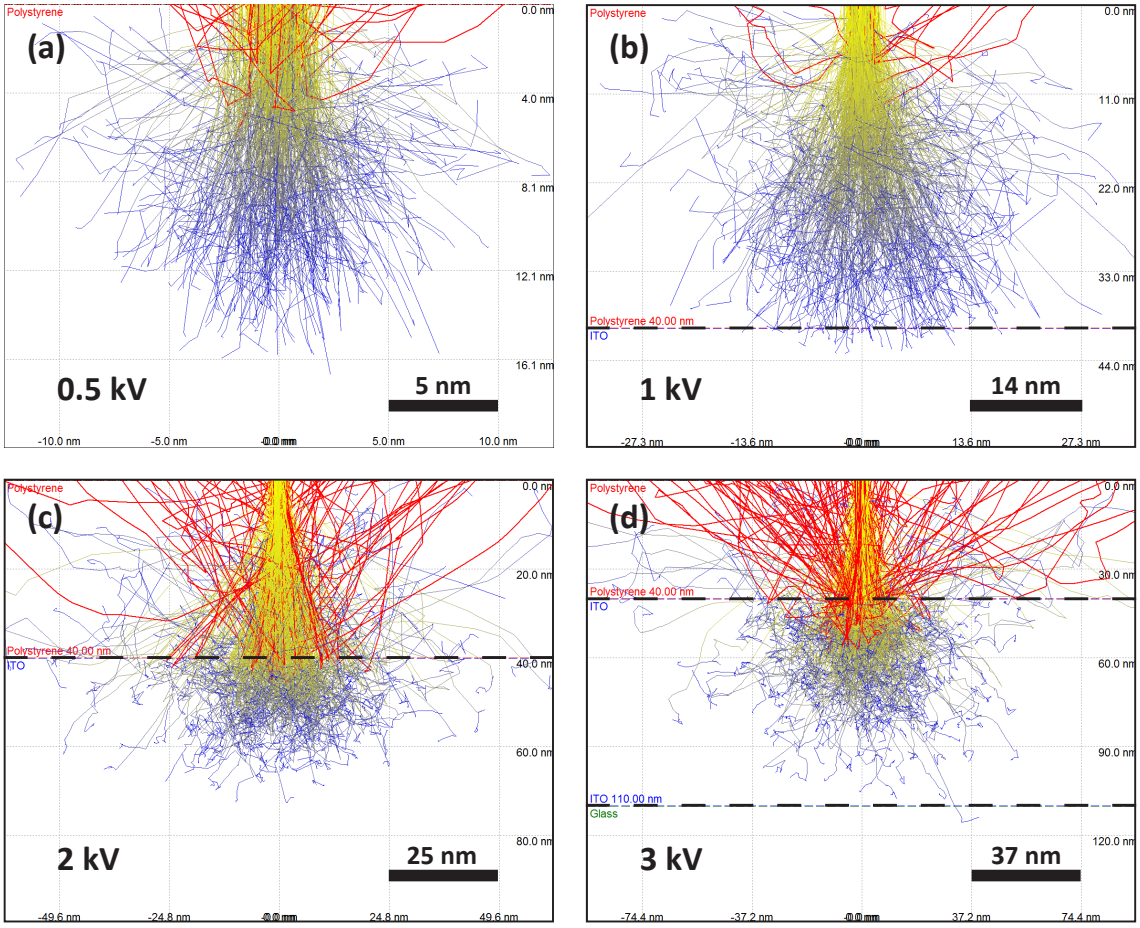

Figure 3.3: *Monte-Carlo simulations of electron scattering in the ITO-glass substrate with a 70 nm thick ITO coating and 40 nm thick polystyrene layer on top. Electron scattering is simulated for landing energies of 0.5, 1, 2, and 3 keV. The figures show trajectories of 500 electrons as an electron-beam with a diameter of 3 nm hits the sample. Red lines represent the trajectories of backscattered electrons, and yellow/blue lines the trajectories of electrons that gradually dissipate all their energy in the substrate. The color scale from yellow to blue represents the electron energy along the trajectories. Dashed black horizontal lines indicate the polystyrene–ITO and ITO–glass interfaces. In (a), the interaction volume extends approximately 16 nm below the surface whereas in (b) it just reaches the interface of polystyrene and ITO at 40 nm. In (c)-(d), more and more electrons start to dissipate their energy in the ITO layer. Because the density of ITO is 7.14 g/cm^3 and that of polystyrene is only 1.05 g/cm^3, backscattering from ITO layer is much more pronounced. The total backscattering coefficients for (a)-(b) are 0.075, 0.060, 0.11 and 0.21, respectively, showing how the behaviour of ITO starts to dominate with higher landing energies. Backscattering coefficient of ∼0.3 is obtained for bare ITO layer. Here, chemical configurations of C_8H_8, $In_{18}SnO_{29}$ and SiO_2 were used for polystyrene, ITO and glass, respectively. The simulations are performed with CASINO v2, which is an open-source simulations software for backscattered electrons in solids.*

CHAPTER 4

Characterization of the probes: TransFluoSpheres 488/645

One of the main advantages of the electronbleaching based superresolution method is that almost any type of fluorescent probes can be employed. In the proof-of-principle experiments, we have chosen streptavidin-conjugated fluorescent microspheres, namely TransFluoSpheres 488/645 (product code: T10711) provided by Molecular Probes [25]. These microspheres are made of polystyrene having a nominal diameter of 40 nm. They are doped with several different dye molecules and are referred here to as fluorescent polymer beads (PBs). These fluorescent probes are chosen because they show good contrast in the SEM and exhibit a very large Stokes shift of 157 nm, which makes them generally easy to work with. Furthermore, the visibility in the SEM is crucial for reliable demonstration of the superresolution method. The PBs also exhibit very bright emission as they are loaded with lots of fluorescent molecules. Moreover, the supplier promises excellent photostability (slow photobleaching), and the streptavidin-conjugation enables antibody-labelling of biological samples without any extra preparation of the probes. Unfortunately, the supplier does not provide more detailed information about the actual dyes inside the microspheres, e.g. their absorption or emission spectra, which would help us to describe the electronic transitions involved in the fluorescent cycle or photo/electronbleaching processes.

In this chapter the electronbleaching behaviour of the polymer beads is experimentally studied. To be able to apply electron-beam induced fluorophore bleaching in the following superresolution experiments, we first need to know how the electronbleaching rate of our probes depends on the electron exposure settings.

The electronbleaching rate is studied as a function of various parameters: electron dose, electric current, electron landing energy, and spatial and temporal electron dose distribution on the sample.

First, the sample preparation is explained, followed by the introduction of the experimental methods. Finally, the results are presented and analysed.

4.1 Samples

The polymer beads were dispersed onto glass substrates with a conductive indium tin oxide (ITO) coating on top (standard 22 x 22 mm microscope cover slips). The substrate needs to be conductive for charge transportation in the SEM and transparent to enable optical imaging from below in the integrated light-electron microscope. The thickness of the ITO layer was not specified by the supplier (Optics Balzers), but for microscope cover slips it is typically on the order of 70 nm. The ITO cover slips were pre-cleaned by the supplier but they were furthermore cleaned in a plasma cleaner, with air precursor, to avoid any possible contamination. The PBs were initially dissolved in water including 50 mM of sodium phosphate (Na_3PO_4), 50 mM of sodium chloride (NaCl) and 5 mM of sodium azide (NaN_3), which constitute a so-called phosphate buffer (pH 7.5), compatible with biological salt solutions.

The first trial of dispersing PBs onto the substrate was simply drop-casting, i.e. pipetting a droplet of the PB solution onto the substrate and letting it dry. However, this approach produced a very non-uniform particle distribution with a lot of large aggregates, and undesired solvent remains and salt crystals showing inconsistent background fluorescence (see Figure 4.1). The bleaching rate was studied by exposing different areas of the sample with varying exposure settings. Hence, the uniformity of the PB distribution and minimization of the ambiguous fluorescent background were important to enable reliable interpretation of the data, i.e. how different parameters contribute to the bleaching rate. Therefore, for the characterization experiments here, the PB stock solution was purified and eventually spin-coated onto the substrate to obtain as consistent samples as possible: salt-free with nicely uniform particle distribution in a single layer.

To remove the salt the stock solution of PBs was purified with dialysis. The solution was loaded in a Micro Float-A-Lyzer dialysis device (100–200 μl) provided by Spectrum Laboratories, which consisted of a porous tubular membrane and a floating support cage [61]. The molecular weight cut-off (MWCO) of the mem-

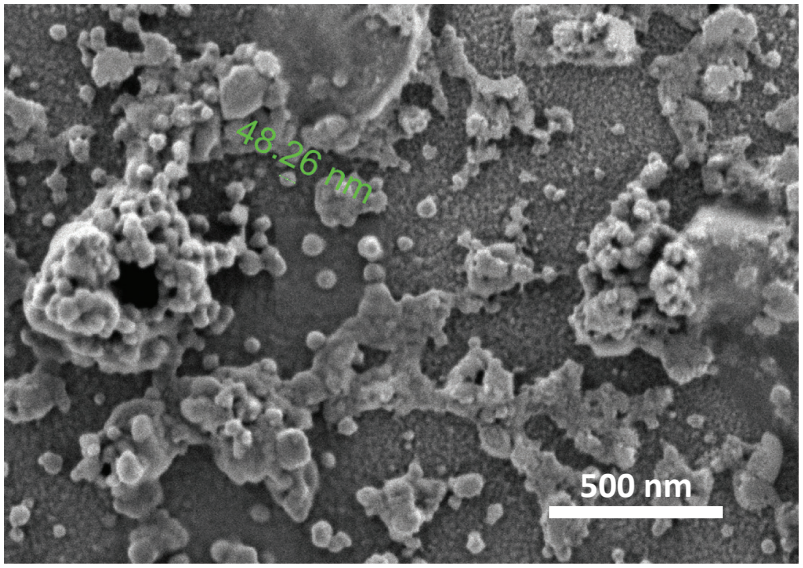

Figure 4.1: *SEM image of the sample surface after the PBs were dispersed onto the substrate by drop-casting the solution with the original salt buffer. Large aggregates and a lot of solvent remains/dirt are found on the sample. The SEM image was acquired with a landing energy of only 500 V. It therefore strictly shows the sample surface only, creating a particular height contrast in the image.*

brane was 50 kDa implying that 90% of the compounds having atomic weight of 50 kDa are retained in the solution. Here, 50 kDa corresponds to approximately a 4 nm microsphere according to dialysis instruction sheet by Bangs Laboratories [62], therefore the loss of PBs in the dialysis process was negligible. The dialysis was performed overnight in a glass beaker filled with de-ionized water, which was exchanged two times. The beaker was kept on a magnetic stirrer to stir the buffer solution (de-ionised water) during the process. Finally, the purified solution was diluted to concentration of 1/10 of the stock solution, the stock solution having $8.2 \cdot 10^{13}$ particles/ml [63].

Water is a particular solvent for the spin-coating process, since it has a very strong surface tension and it sticks to hydrophilic surfaces. Furthermore it dries relatively slow in the ambient. To spread the particles uniformly onto the glass substrate, increasing spinning speed was found to be beneficial during spin-coating process. The spinning program consisted of four subsequent steps of 60 s each, starting from 700 rpm and ending up to 1000 rpm, with acceleration of 1000 rpm/s for every step. After each of the first three steps, the spinning direction was changed and spinning speed increased by 100 rpm. At 1000 rpm, the remaining water droplet was finally swept off from the surface, and the spin-

coating was finished. Possible remains of water were let to dry on the surface before proceeding to experiments.

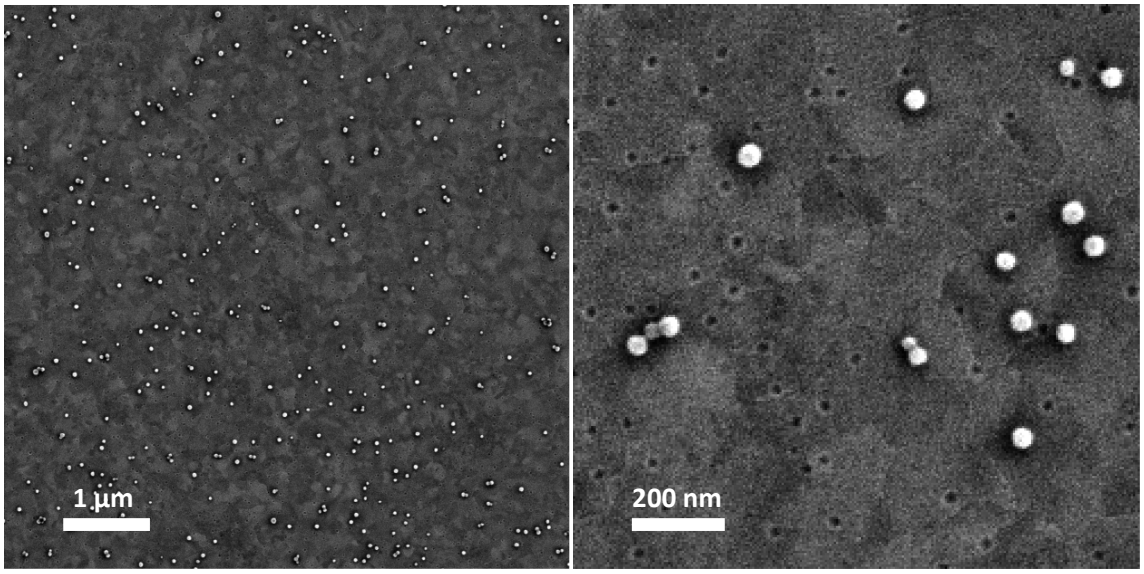

Figure 4.2: *Two SEM images of Sample I with different magnifications. Polymer beads are distributed randomly, but they show approximately a uniform concentration on average, over a larger area. The PBs appear bright in the image, whereas the structure of ITO shows in the background.*

Figure 4.2 shows two SEM images of a sample used for most of the characterization experiments covered below (Sample I). The particle diameter varies rather much and the real diameter specified by the supplier for two random batches of microspheres is actually 48±6 nm [63]. The particle concentration in this sample was approximately 8.7 particles/μm^2, which was calculated over an area of tens of μm^2 in the middle of the sample. Local variation of the concentration was substantial but an area of this size shows already a rather consistent average concentration. On a larger scale, a concentration gradient was observable such that on the edge of the sample the particle concentration was much smaller. An FM image of the sample is shown later in Figure 4.3. Relatively uniform fluorescence is obtained in the field-of-view of the optical microscope, besides the bleached rectangles that are exposed by the electron beam.

4.2 Experimental methods

The bleaching rate of the fluorescent polymer beads (TransFluoSpheres 488/645) was studied as a function of electron dose, electric current, electron landing energy, and spatial and temporal electron dose distribution. The electronbleaching rate refers strictly speaking only to the actual rate by which the fluorescent compounds bleach, i.e. the rate of fluorescence intensity decay as a function of electron dose. However, the bleaching rate as a function of dose may depend also on the values of other electron-beam parameters, such as electron landing energy. In this case, the electron bleaching rate may be studied as a function of these other parameters, too. We may assume that the dependence on the electron dose follows always the same model regardless of the values of the other e-beam parameters, the bleaching model being exponential decay. When we study the bleaching rate as a function of some other parameter, the dose is fixed and the rate can be studied in other dimensions of the five-dimensional parameter space.

The parameters are practically varied as follows. First of all, the electron dose D is defined by

$$D = \frac{IT_{dwell}}{A} = \frac{IT_{dwell}}{s^2}, \tag{4.1}$$

where I is the electric current, T_{dwell} is the dwell time, i.e. the time electron beam spends on each SEM pixel, and A is the area of that pixel which is basically defined by the step-size s of the e-beam. It follows that we can change the total electron dose per area by changing any of the three parameters. However, here we want to separately study the effects of the electric current and step size, step-size referred to as spatial dose distribution. The electron dose is therefore varied by varying the dwell time. The temporal dose distribution refers to fractionating the dose injection in time while keeping the total dose and electric current constant. Fractionating the dose in time means, for instance, that the area is exposed by ten e-beam scans with a dwell time of 1/10 of the dwell time of a single scan.

Here, we used a separate scanning electron microscope (FEI Verios 460) and a fluorescence microscope (Nikon Eclipse Ti). The bleaching rate was studied as an average behaviour by measuring ensembles of particles. The electron dose is varied by varying the dwell time, which can be inserted in the FEI user interface with an accuracy of 100 ns. The electric current can be chosen from the pre-set nominal values: 3.1, 6.3, 13, 25, 50 pA and so on. Electron landing energy is

determined by the electron acceleration voltage in the SEM column, and possibly applied stage bias-voltage, which both can be adjusted with an accuracy of 1 V. Spatial dose distribution (e-beam step size) is varied by changing the resolution of the SEM image and/or the horizontal-field-width (HFW), i.e. the size of the SEM field-of-view. The resolution can be chosen from several pre-set values and the HFW can be inserted with an accuracy of three significant digits, the HFW generally being more than 10 μm^2. Finally, the temporal dose distribution can be studied by choosing a total dose and exposing the sample with a single and multiple scans by keeping the product $T_{dwell} \cdot$ (cycle number) constant.

In the electronbleaching experiments, the electron beam in the SEM was first aligned and focused on the sample in a location outside the measurement area, to avoid any prior bleaching of the fluorescent beads. Then, the stage was moved by inserting coordinates of relative movement while keeping the electron beam blanked. A regular pattern of rectangles was exposed one by one with different exposure settings, varying one of the parameters while keeping the other parameters constant. After that, the FM imaging was performed with the separate microscope, for which the sample was brought from vacuum to the ambient conditions. The so-called bleaching pattern was searched with a low-magnification (5 x) objective because of its large field-of view. The actual FM imaging was then performed with a 40 x or 60 x objective. An example of a bleaching pattern on Sample I can be seen in Figure 4.3, where the electron dose was varied while keeping other parameters constant. The fluorescence intensity is clearly changing from rectangle to rectangle which indicates change in the ratio of bleached fluorophores.

From the FM image, the fluorescence intensity was integrated over the exposed areas (rectangles), which sizes were typically on the order of tens of μm^2. Intensity extraction was done with an open-source image processing software ImageJ, and the data was exported for further processing in a spreadsheet application. To calculate the normalized intensity I/I_0 for a certain parameter set, the average intensity inside the rectangle, I_s, was compared to a reference value I_{ref}. Because the original intensity of the corresponding area was impossible to measure with the arrangement of two separate microscopes, the reference was taken around the bleached rectangle, assuming that the average intensity around the rectangle resembles the original intensity inside it. The sample and reference areas are indicated in Figure 4.3. Background signal was measured from bare ITO

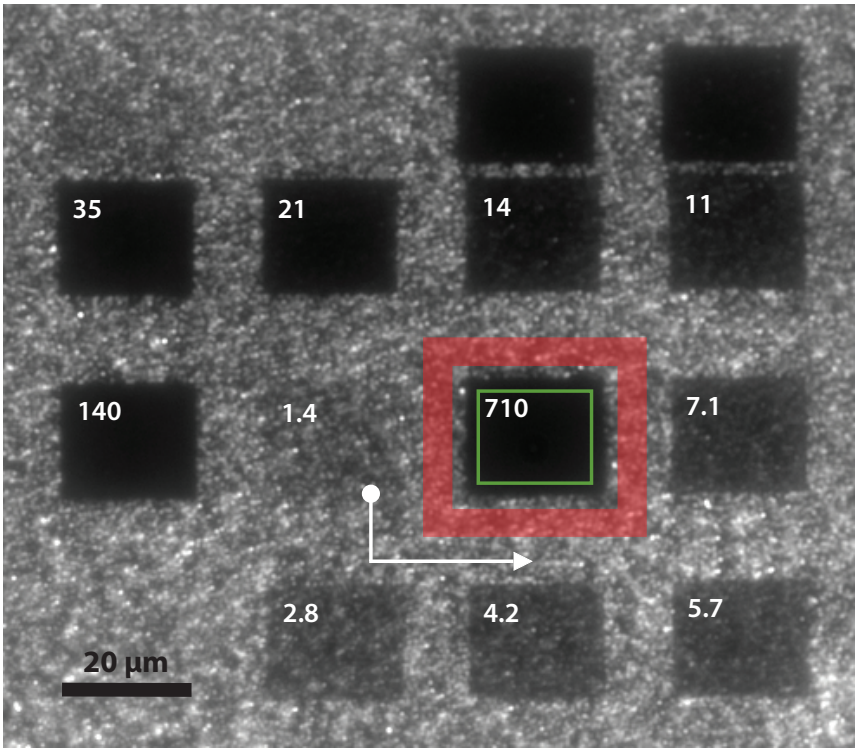

Figure 4.3: *Fluorescence image of Sample I. Relatively uniform fluorescence is obtained over the FM field-of-view. Dark rectangles in a spiral pattern are exposed with different electron doses showing noticeable variation in the remaining fluorescence intensity (bleaching). The measurement series starts from the rectangle exposed with the lowest dose, indicated with the white sphere, and the pattern continues with increasing dose as indicated by the white arrow. The dose for each rectangle is denoted in $electrons/nm^2$. The rectangle with the highest dose is in the middle, surrounded by green and red rectangles. The green rectangle borders the area from which the sample intensity is calculated, and the red area depicts the reference area, to which the sample intensity is compared to calculate the bleaching ratio. Row on the top is a separate measurement (two very light rectangles on the left and two dark ones on the right). The FM image was acquired with a 60x objective.*

glass, and the average value I_{bg} was subtracted from sample and reference values prior to the comparison. Hence, the normalized intensity for a rectangle is given by

$$\frac{I}{I_0} = \frac{I_s - I_{bg}}{I_{ref} - I_{bg}}. \tag{4.2}$$

In addition, complete images can be subtracted from each other with ImageJ. Because the sample illumination in the FM was not completely uniform, background subtraction becomes more accurate if the complete image of a bare ITO glass is subtracted from the sample image, prior to the calculation of the sample

and reference intensities. This method was applied in some of the latter characterization experiments.

Typically fluorescence images were acquired with the maximum illumination power of the LED source (Lumencor SPECTRA light engine) at 475 nm peak wavelength, nominal maximum power being 400 mW. Integration times of 3–10 s were used for the CCD camera (Ixon).

The electric currents in the SEM were measured for different landing energies with a so-called Faraday cup on the sample holder. The holder was isolated from the stage with a teflon spacer and was connected to an external picoampere current meter. Faraday cup is basically a deep micron scale size hole which traps all the electrons when the electron beam is focused inside the hole. Therefore, no electrons exits the sample and the total current can be guided to the current meter. Accuracy of ± 0.2 pA was obtained, estimated from the variations in the values shown by the current meter.

4.3 Results and conclusion

In this section, I present the results of the experimental electronbleaching study of TransFluoSpheres 488/645, described above. The bleaching rate was studied as a function of electron dose, electric current, electron landing energy, and spatial and temporal electron dose distribution on the sample.

4.3.1 Electron dose

In Figure 4.4 we plot the normalized fluorescence intensity of the polymer beads as a function of electron dose. Here, we chose a nominal electric current of 25 pA, e-beam step size of 4.9 nm and landing energy of 5 or 1 keV. The measured current values were 28.5 pA and 27.0 pA, for landing energies of 5 keV and 1 keV, respectively. The dose was distributed to the sample in a single pass. The intensity seems to decay more or less exponentially, but the curves have a major offset from the zero-level. To extract the fluorescence decay rate, an exponential function is fitted to the experimental data. Because of the offset, a constant was added to the fitting model which is given by

$$F(D) = (1 - C) \cdot \exp\left(-\frac{D}{\tau}\right) + C, \tag{4.3}$$

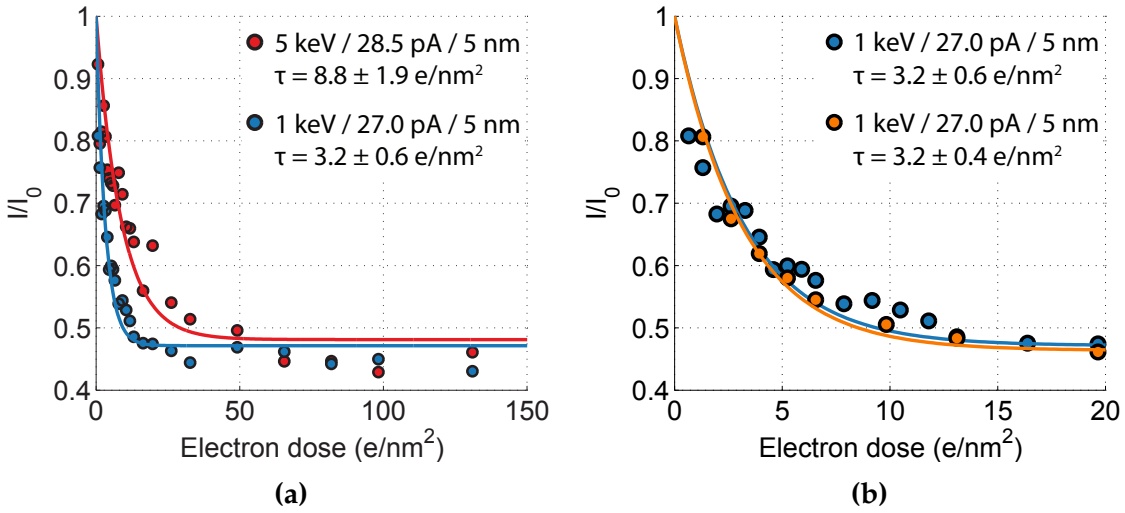

Figure 4.4: *Normalized intensity as a function of electron dose. Exponential function is fitted to the experimental data and then plotted with the data points. In (a), exposure with landing energy of 1 keV (blue) shows much faster bleaching than exposure with 5 keV (red). The decay constants τ are marked in the figures, as well as the landing energy, electric current and e-beam step size for the corresponding measurement. (b) shows a comparison between two separate measurements at low dose values, with exactly the same exposure settings. The blue dots represent the same data as the blue dots in (a). The data with orange is from exposure pattern shown in Figure 4.3. Slight deviation is visible but the fitting gives almost an identical decay constant, which shows the consistency of the electron dose dependence of fluorescence. Here, a nominal current of 25 pA was used for all measurements, but the actual measured currents differ a bit for different landing energies, denoted in the figures. However, at this point the nominal value was used in calculating the electron dose for plotting and fitting the data.*

where C is the offset, D the electron dose and τ the decay constant. Here, as the first approximation, we assume the fluorescence decay to follow a single-exponential. However, a somewhat consistent deviation can be observed between the fit and the experimental data (see Figure 4.4, 4.5a), implying that multiple electronbleaching processes might be embedded under the bleaching curve (see Section 3.1). More thorough analysis including multi-exponential fitting would be required to confirm this, but decay constants from single-exponential fits are sufficient to estimate the bleaching rates at this point.

Fitting was performed with MATLAB curve-fitting tool which uses the method of least squares. Here, the error for fitting parameters was estimated with 95% confidence bounds, given by the curve-fitting tool. In Figure 4.4a, decay constants of $\tau = 8.8 \pm 1.9 e/nm^2$ and $\tau = 3.2 \pm 0.6 e/nm^2$ were obtained for 5 keV and 1 keV landing energies, respectively. Figure 4.4b, shows the same data for 1 keV as Figure 4.4a with another measurement with exactly the same exposure settings

on a different day. The obtained decay constants $\tau = 3.2 \pm 1.9 e/nm^2$ and $\tau = 3.2 \pm 0.4 e/nm^2$ proves the consistency of electron dose dependence of fluorescence emission.

The measurement error of the normalized intensity was on the order of 0.03, which was estimated by calculating the standard deviation of the normalized intensities for an exposure pattern where all rectangles were exposed with identical settings. The standard error of the fit, i.e. standard deviation of the data points from the fit, was 0.02–0.05 for the data presented in Figure 4.4. Thus, the model of single-exponential decay gives a sufficient approximation for the bleaching rate even though the fluorescence decay due bleaching is not necessarily a single-exponential, as pointed out in Chapter 3.

Concerning the offset, even if all the particles are fully bleached after extensive electron exposure, there was still some remaining fluorescence left after background subtraction. Spectral measurements revealed another peak in fluorescence emission which barely decreased during photobleaching of the PBs by the excitation laser. The spectral measurements were performed with a confocal laser scanner installed in the Eclipse microscope. Most probably the remaining emission came from the remaining solvent compounds on the substrate. It might be also induced by the electron exposure of the sample. Nevertheless, the offset here is not of great importance for the superresolution experiments, so the reason was not extensively studied. More comprehensive spectral measurements would be required for further understanding of the origin of the fluorescence background signal.

To conclude, electronbleaching leads to an exponential-like decay of the fluorescence emission as a function of electron dose, such as photobleaching as a function of light dose. The bleaching rate is basically the derivative of the bleaching curve. From Figure 4.4 it can already be noticed that the bleaching rate depends also on some other exposure parameters, in this case the landing energy, which will be discussed below.

4.3.2 Electric current

Figure 4.5a shows the normalized intensity (bleaching rate) as a function of electron dose for various electric currents. Figure 4.5b shows the same data but now the normalized intensity (bleaching rate) is plotted as a function of electric current for constant doses. The rise in current is compensated by changing the dwell

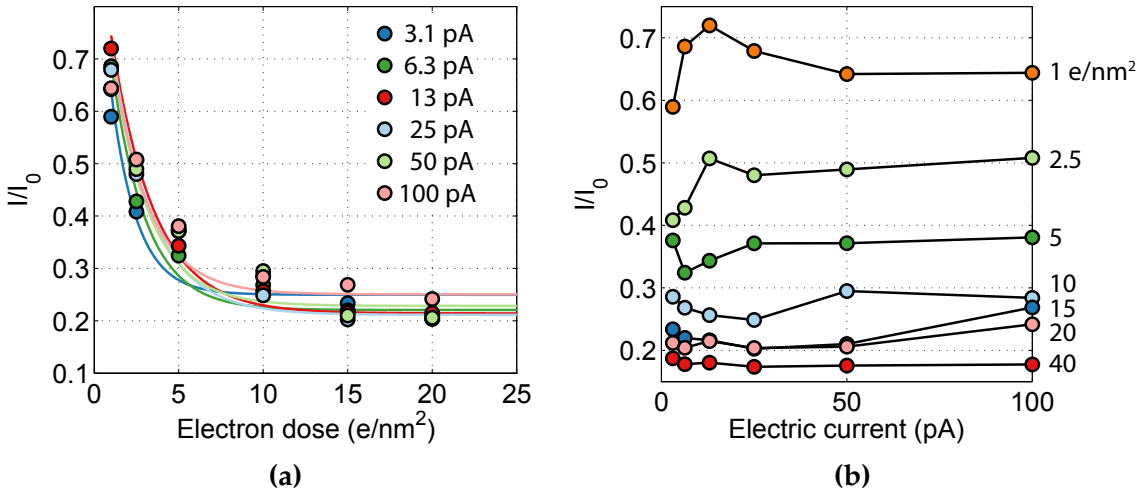

Figure 4.5: *In (a), the normalized intensity is plotted as a function of electron dose for different electric currents, with exponential fits. In (b), the same data is presented as a function of electric current for different doses. (b) shows cross sections of (a) for constant doses, revealing the bleaching rate dependence on the current. There is no consistent dependence on the current. Even though some variation in the bleaching rate can be seen at low currents at low doses, the curves are mostly flat. Here, we used a landing energy of 1 keV, e-beam step size of 7.3 nm.*

time, thus keeping the dose constant. Here, we used a landing energy of 1 keV, e-beam step size of 7.3 nm, and the dose was distributed in a single scan. The electric current shows a little effect to the bleaching rate. The decay constants are between 1.5 and 2.6 e/nm^2 with average error of ± 0.7 e/nm^2. With low doses, there is a bump at low currents, but the trend is not consistent and the curves are mostly flat. No consistent dependence was observed in any other experiment either. Thus, we conclude that the current dependence of electron bleaching is negligible and we do not need to consider it in further experiments.

4.3.3 Electron landing energy

Figure 4.6 shows the normalized intensity (bleaching rate) as a function of landing energy. A very clear minimum can be found at approximately 1 keV. It means that the bleaching is most efficient at that landing energy. The reason is that the interaction volume of the electron beam at 1 keV is similar to the size of the polymer bead (see Section 3.2), and no dose is "lost" to the substrate. Using a low landing-energy is beneficial for the superresolution method, as when the interaction volume is small, out-of-focus bleaching alleviates from electron scattering in the substrate. At the same time, as an efficient bleaching energy is employed,

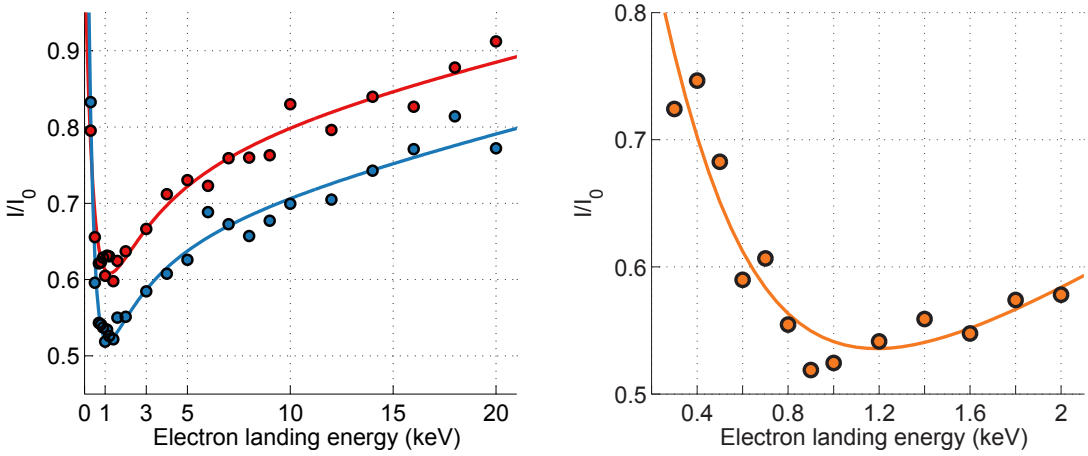

Figure 4.6: *In (a), the normalized intensity is plotted as a function of electron landing energy for two different e-beam step sizes: 7.3 nm (red) and 14.6 nm (blue). Electric current of 55 pA and dose of 10.2 e/nm^2 was used for exposure. In (b), data from another measurement is presented taking a closer look to the voltage range around the minimum intensity. Here, nominal electric current of 25 pA, dose of 6.3 e/nm^2, and e-beam step size of 7.3 nm was used for exposure. The intensity minimum, i.e the most efficient bleaching value, is found around 1 keV. All the curves are only illustrative and not fits with any physical model.*

the contrast of in-focus/out-of-focus bleaching should be enhanced. Hence, the results of the landing-energy study are very useful and a near-optimal bleaching value is employed in the further superresolution experiments.

4.3.4 Spatial dose distribution

Figure 4.7 shows the bleaching rate as a function of electron-beam step size. Surprisingly, the dependence on the step size is apparent at step-sizes smaller than our fluorescent polymer beads. The most efficient bleaching is found roughly at 20 ± 10 nm. For larger step-sizes, the intensity increases because the electron-beam simply starts to miss particles. For short step-sizes the reason is not fully understood. To investigate the phenomenon, a simplified MATLAB calculation was performed for the total electron dose, directly injected to a particle, as a function of step size. First, the total intersection volume of the e-beam interaction volumes and the microsphere was calculated. Interaction volumes were spaced in a square matrix with a separation of e-beam step size, as in the real SEM scan. Only the interaction volumes having the center inside the sphere radius, i.e. e-beam hits the particle directly, were taken into account. The total intersection volume is the sum of the individual intersection volumes for the e-beam spots (inside the

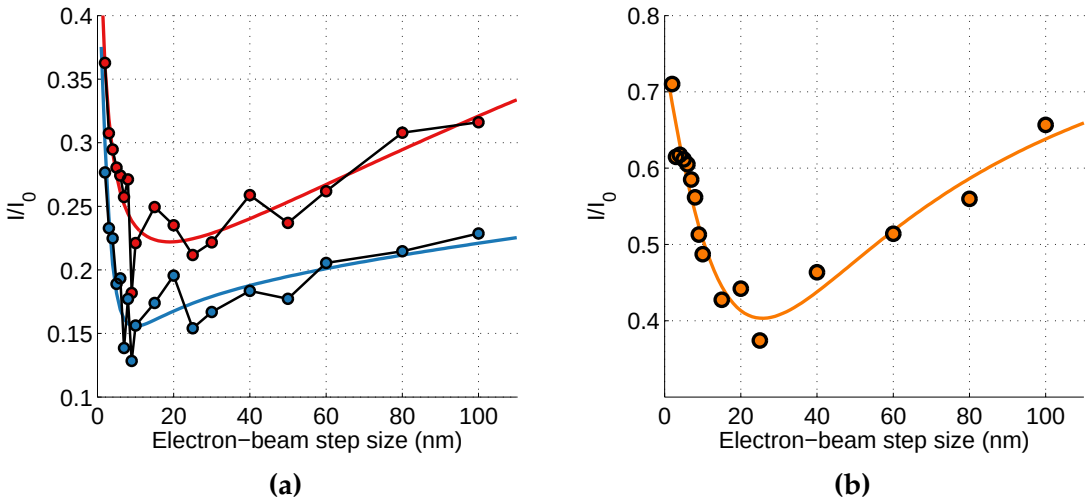

Figure 4.7: *In (a), the normalized intensity is plotted as a function of e-beam step size for two different doses: 6.3 e/nm^2 (red) and 10.2 e/nm^2 (blue). Electric current of 27 pA and landing energy of 1 keV was used for exposure. In (b), data from another measurement is presented with identical exposure settings with 6.3 e/nm^2, corresponding to the red curve in (a). In (b), some of the data points are average values over several exposed rectangles. Surprisingly, the step-size dependence of the bleaching rate is obvious also at step-sizes smaller than the polymer beads. The intensity minimum is found roughly at 20 ± 10 nm. All the curves are only illustrative and not fits with any physical model.*

sphere radius), and the total dose was obtained by multiplying the total volume with the dwell time corresponding to the step-size while the dose per area was kept constant. However, the directly injected dose was constant as a function of step size, not explaining the dependence.

The only obvious difference with various step sizes is the following: with large step-size the dose is more localized on the sample than with small step-size. It follows that with a regular raster scan of horizontal lines, more dose will be injected into the nanoparticle per one scan line. For example, if the step size is doubled, the dwell time needs to be multiplied by four to keep the dose per area constant. Therefore, with doubled step-size, an equal electron dose will be distributed to the sample in only one scan, as in two scans with the initial step-size. There is a delay time between the local dose injection, corresponding to the scanning time of one line. Thus, one suggestion was that maybe some kind of charge dissipation or saturation effect plays a role in electronbleaching. This suggestion, however, is not consistent with the result obtained for the temporal dose distribution, explained below.

4.3.5 Temporal dose distribution

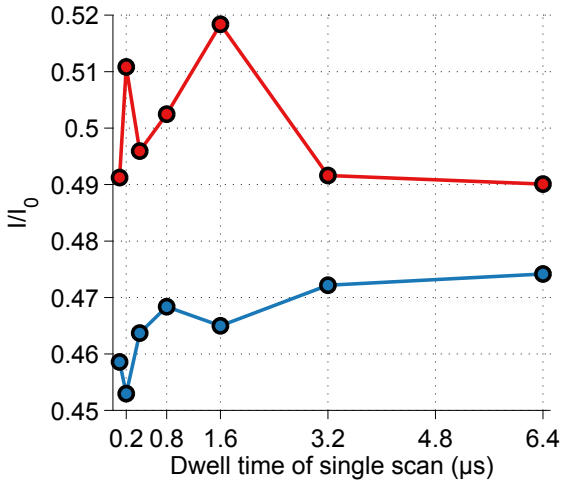

Figure 4.8: *The normalized intensity is plotted as a function of dwell time of a single scan, the total dwell time being 6.4 µs. The dwell time of single scan corresponds to the amount of scans in which the total dose was distributed. The exposure was done with nominal current of 25 pA, 4.9 nm step size, and landing energy of 5 keV (red) and 1 keV (blue). Some of the data points are average values of two bleached rectangles. The variation of normalized intensity is within the error of the experiment.*

The temporal distribution of electron dose did not affect the bleaching rate as can be seen in Figure 4.8. The temporal dose distribution means that the injected dose is fractionated in time while keeping the total dose and electronic current constant. For example, in Figure 4.8, the dose was injected to the sample with 64 scans with 100 ns dwell time, 32 scans with 200 ns dwell time and so on, until a single scan with 6.4 µs. The variation in fluorescence intensity is within the few percent error marginal of the experiments.

The temporal dose distribution could well be studied further in the integrated SECOM platform with a so-called time-lapse measurement, where the same sample area could be exposed pass by pass, during which the fluorescence intensity is monitored. Further experiments of temporal distribution would be necessary to find the explanation for the step-size dependence discussed above.

To conclude the chapter, the bleaching rate of fluorescent microspheres depends mostly on electron dose and landing energy, but also on the spatial dose distribution (e-beam step size). However, the step size dependence is not fully understood. We assume that the electron exposure parameters are independent on each other, such that they all can be separately studied by just fixing the oth-

ers to some typical values. This assumption is not necessary valid in some cases, but in the characterization experiments here, it is sufficient to gain qualitative understanding on the bleaching behaviour.

The contribution of the photobleaching was negligible in the ambient conditions. Even after 40 min of illumination with full power (400 mW) of the LED source (475 nm peak wavelength), the fluorescence intensity did not decrease more than a few percents. Surprisingly, in vacuum the photobleaching of the polymer beads is highly pronounced, which complicates the superresolution experiments as will be seen in Chapter 6.

CHAPTER 5

Development of the superresolution method

This chapter covers the main objective of the Master's thesis: the development of the electron-beam-induced superresolution method in an integrated light-electron microscope. First, the integrated microscope platform, know as the SECOM, is introduced. After that, the principle of the superresolution method is explained in detail, and the practical implementation and samples are discussed.

5.1 SECOM platform

The SECOM platform is an integrated light-electron microscope where correlative light and electron microscopy can be performed "on the spot". SECOM stands for Scanning Electron Combined Optical Microscopy and the platform is provided by Delmic, a spin-off company of the Charged Particle Optics research group [7, 9, 10]. In the SECOM platform, the original door of the SEM is replaced with a customised door including the light microscope part. A schematic of the system is shown in Figure 5.1. In this work, the SECOM platform was used on FEI Quanta FEG 250 and FEI Verios 460 scanning electron microscopes.

In the SECOM platform, an inverted high-NA objective is positioned inside the SEM below the sample holder. The SEM electron objective lens and the light objective lens have the same focal plane such that electron and optical imaging can be performed simultaneously. The sample holder can be moved by piezos in XY-directions and the light objective in all XYZ-direction, from which Z-direction is used for focusing and XY-directions to align the optical axis to the electron-beam axis. A mirror is placed below the light objective lens to guide the excitation light into the sample and fluorescence emission out of the vacuum chamber, through

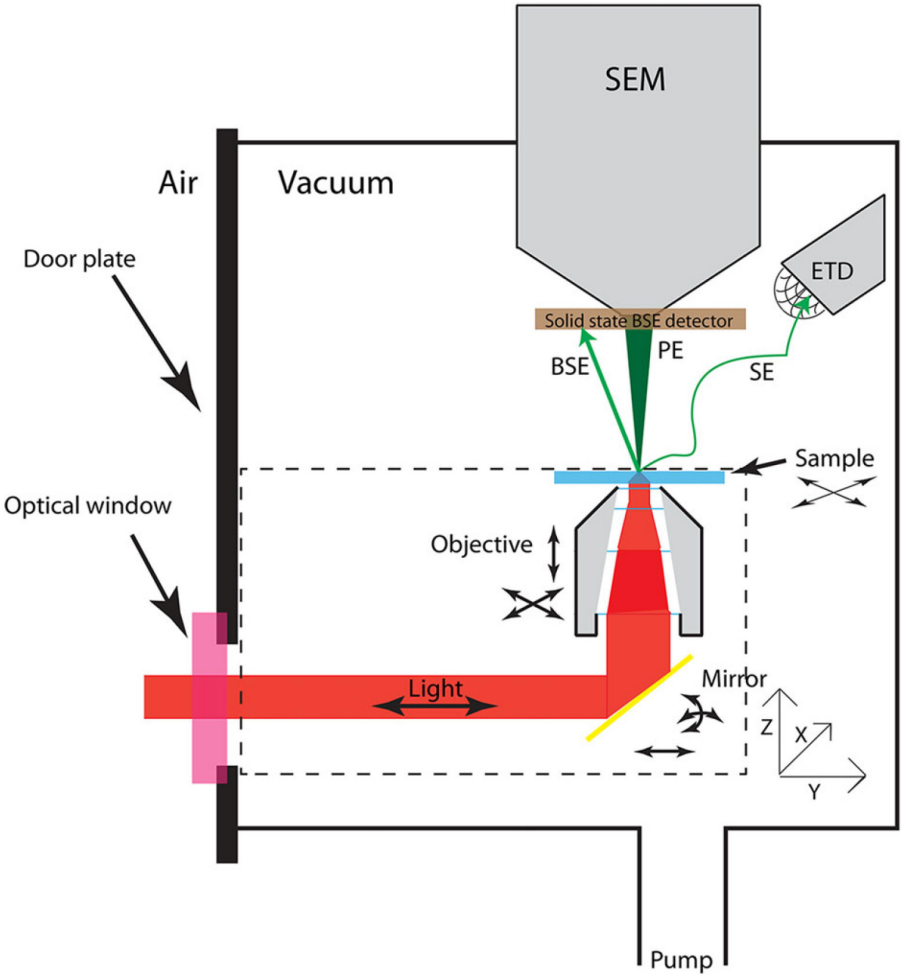

Figure 5.1: *Schematic depiction of the SECOM platform inserted into the vacuum chamber of an SEM, with definition of the coordination system. The light microscope part inside the chamber is surrounded with dashed line. The degrees of freedom for the sample, objective and mirror movement are depicted with arrows. PE, SE and BSE refer to primary, secondary and backscattered electrons, respectively. ETD refers to an Everhart-Thornley secondary-electron detector. The figure is from [9].*

a vacuum sealed window. All other optical components are located outside the chamber on an optical "breadboard", which gives the freedom to vary the microscopy technique applied on the SECOM platform. In our case, just a simple epi-fluorescence microscope is employed, which is schematically illustrated in Figure 2.5. The system consists of an excitation path and an emission path which are combined inside a filter cube. The filter cube consist of a band-pass excitation filter, a dichroic mirror and a long-pass emission filter. Figure 5.2 presents photographs of the SECOM platform on the FEI Verios 460.

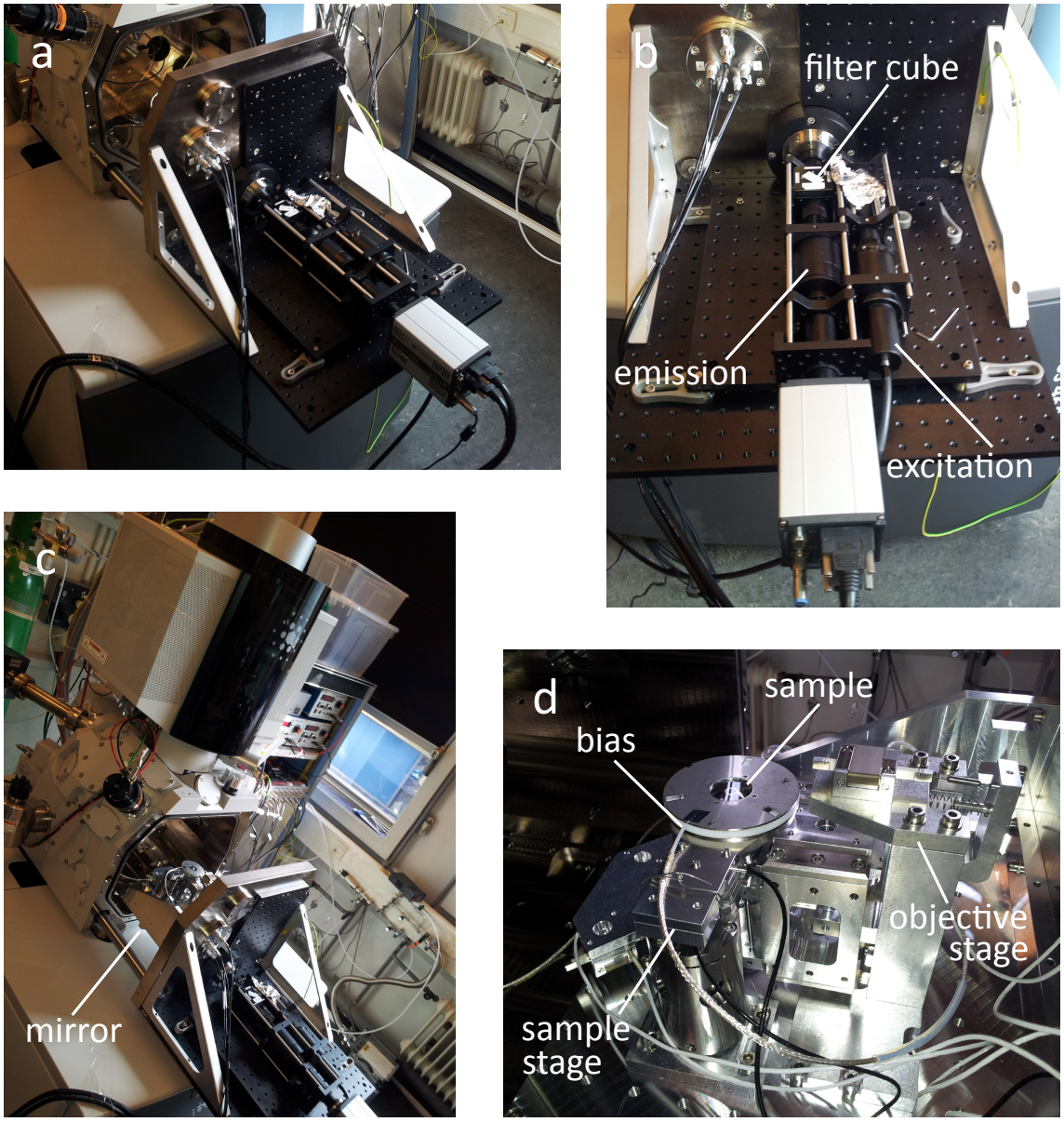

Figure 5.2: *Photographs of the SECOM platform on the FEI Verios 460. In (b), the excitation and emission paths are denoted with the filter cube, in which the paths are combined. In (c), the mirror is indicated below the stage. (d) shows the piezo stage configuration, and points out the sample and the connection for stage bias-voltage. An insulating teflon spacer can be seen under the sample-holder ring, and the light objective under the sample.*

Operation of the SECOM platform involves the usage of the SEM operating software (in our case provided by FEI) and SECOM's own operating software (Odemis). First, the user needs to align and focus of the electron-beam in the SEM software. Furthermore, the beam energy (acceleration voltage and possible stage bias), current and magnification must be chosen in the SEM user interface.

After that, the SEM must be switched to an external-control mode and the rest can be done with Odemis. The user can find the optical focus and align the optical and electron axis by moving the light objective. The axis alignment is done by imaging cathodoluminescence (CL) from the substrate and centering the CL spot to the middle of the optical image. After that, an automatic fine-alignment procedure can be run. The fine alignment basically calculates the translation, rotation and scaling between the FM and EM image, by writing a regular CL pattern with the SEM and defining the CL spot locations in the optical image. An overlay accuracy of sub-5 nm has been demonstrated between the FM and EM images [64]. A desired region-of-interest is chosen by moving the sample in XY-directions. Furthermore, the e-beam dwell time and the EM image resolution can be controlled on Odemis. Odemis also provides a full control over the light microscopy part: the excitation light power and spectrum, and the camera integration time. The SECOM platform employs Lumencor SPECTRA light engine, which is a seven-color LED light source for excitation, and Andor Zyla 5.5 sCMOS Camera for optical imaging.

In this work, the SECOM platform was additionally controlled with a Python script to perform the superresolution imaging procedure. The scripting and some required modifications to the hardware drivers were done with support from Delmic. The practical implementation and automation of the method by the Python script is discussed in detail below in Section 5.3.

5.2 Principle of the method

This section covers the principle of the optical superresolution method developed in this work, which can be applied to localize and distinguish fluorescent probes with resolution well beyond the diffraction limit of light. It could be said that this section is the most important section of the entire Master's thesis providing the understanding of how the method actually works.

First of all, the method is based on electron-matter interaction which modifies the fluorescent properties of the probe, namely destroying the fluorescence emission. In other words, electron scattering in the specimen induces changes in the chemical configuration of the fluorophores, such that they stop emitting photons, a phenomenon considered as electronbleaching, discussed earlier in Chapter 3. It all implies that the fluorescent probes could be "switched off" with the electron beam in a controlled manner.

Operational principle of the superresolution method is illustrated in Figures 5.3-5.6. First, a region-of-interest (ROI) on the sample is defined from the FM image, shown in Figure 5.3. The ROI (red square) must be chosen inside the SEM field-of-view (white square), which is aligned to the middle of the optical field-of-view. It is advised to keep the electron-beam blanked while moving the sample and looking for a desired ROI, and unblank the beam just before starting the imaging procedure. This is done in order to minimize the chance of unintentional electronbleaching of any potential ROI in the sample.

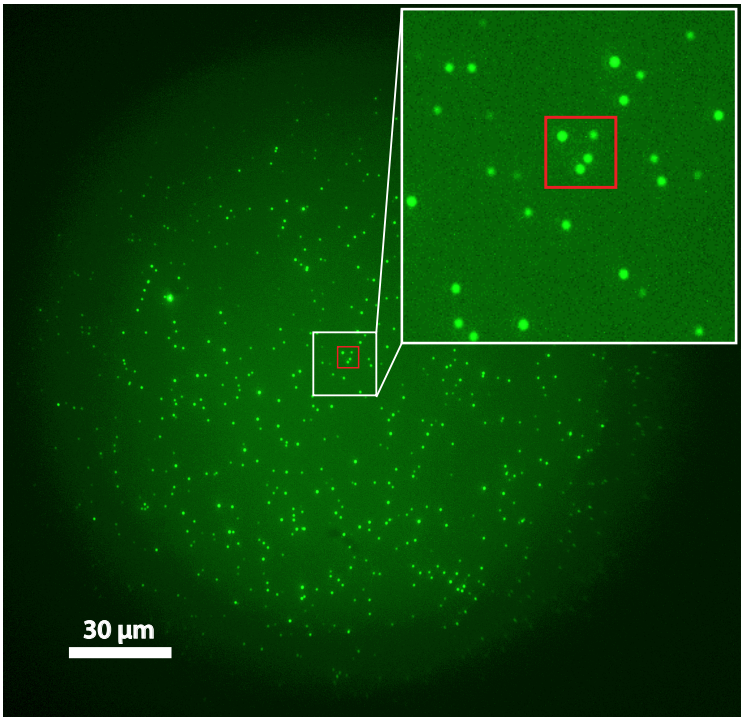

Figure 5.3: *Fluorescence image of Sample II, prepared for superresolution experiments consisting of fluorescent polymer beads on ITO-glass substrate. Substantially lower particle concentration is present than in the earlier samples for the characterization study. The light objective is aligned such that the SEM field-of-view (white square) is in the middle of the optical field-of-view. A desired region of interested (red square) can be chosen inside the SEM field-of-view.*

The imaging procedure begins by acquiring an FM image of the sample in its initial state, prior to any electron exposure of the ROI. This initial image is referred to as the 0th FM image. At this time the beam is waiting at a parking spot outside the ROI (see Figure 5.4). The ROI is divided into sub-areas called superresolution (SR) pixels, the size of which determine the uppermost limit for the localization precision of fluorescent probes, and thus for the resolution of the final SR image. The electron beam scans the ROI exposing it pixel by pixel,

during which the fluorescence intensity is monitored. Once the electron beam hits a fluorescent probe, a drop can be observed in fluorescence intensity in the ROI, enabling the localization of the fluorescent probe into the corresponding SR pixel.

The electron beam is constantly on and it moves back and forth between the ROI and the parking spot. An FM image of the sample is acquired after electron exposure of each individual SR pixel, while the beam is waiting at the parking spot. The SR pixels are always exposed in order from left to right, and from top to bottom, row by row. An average intensity is calculated in the FM image over the ROI, and the obtained value is compared between the subsequent images. That is, the intensity value of the 1st image is subtracted from that of the 0th image to evaluate the change in the fluorescence intensity due to electron exposure of the 1st SR pixel, and so on. A discrete drop in fluorescence intensity indicates that a fluorescent probe has been bleached inside the corresponding SR pixel.

Fluorescence intensity can be plotted as a function of the FM image number, directly connected to the SR pixel exposed prior to the FM image. The resulting curve is called the fluorescence trace, which is sketched as a red curve in Figure 5.4. Absolute change in the intensity value, between subsequent images, is basically the derivative of the intensity trace between the corresponding data points. A peak in the negative derivative corresponds to a sudden decrease of fluorescence intensity. The final superresolution image is reconstructed by plotting the negative derivative value in gray scale for corresponding SR pixels. In other words, in the final SR image, the gray scale indicates the difference in average fluorescence intensity, inside the ROI, before and after electron exposure of the corresponding SR pixel.

Figure 5.5 shows an example of the imaging procedure with real experimental data. Here, we have chosen a SR pixel size of 250 nm. Three diffraction limited fluorescence spots can be seen in the FM image, and when the electron beam scans over the ROI (blue square in Figure 5.5a), the fluorescence spots disappear one by one (Figures 5.5a-d). In Figure 5.5e, the fluorescence trace is plotted with a black curve and its negative derivative with a red curve. It can be noticed, however, that the derivative peaks are not much above the noise level. Fortunately, there is something we can do to improve the signal-to-noise ratio (SNR), to make the detection of fluorescent probes more sensitive.

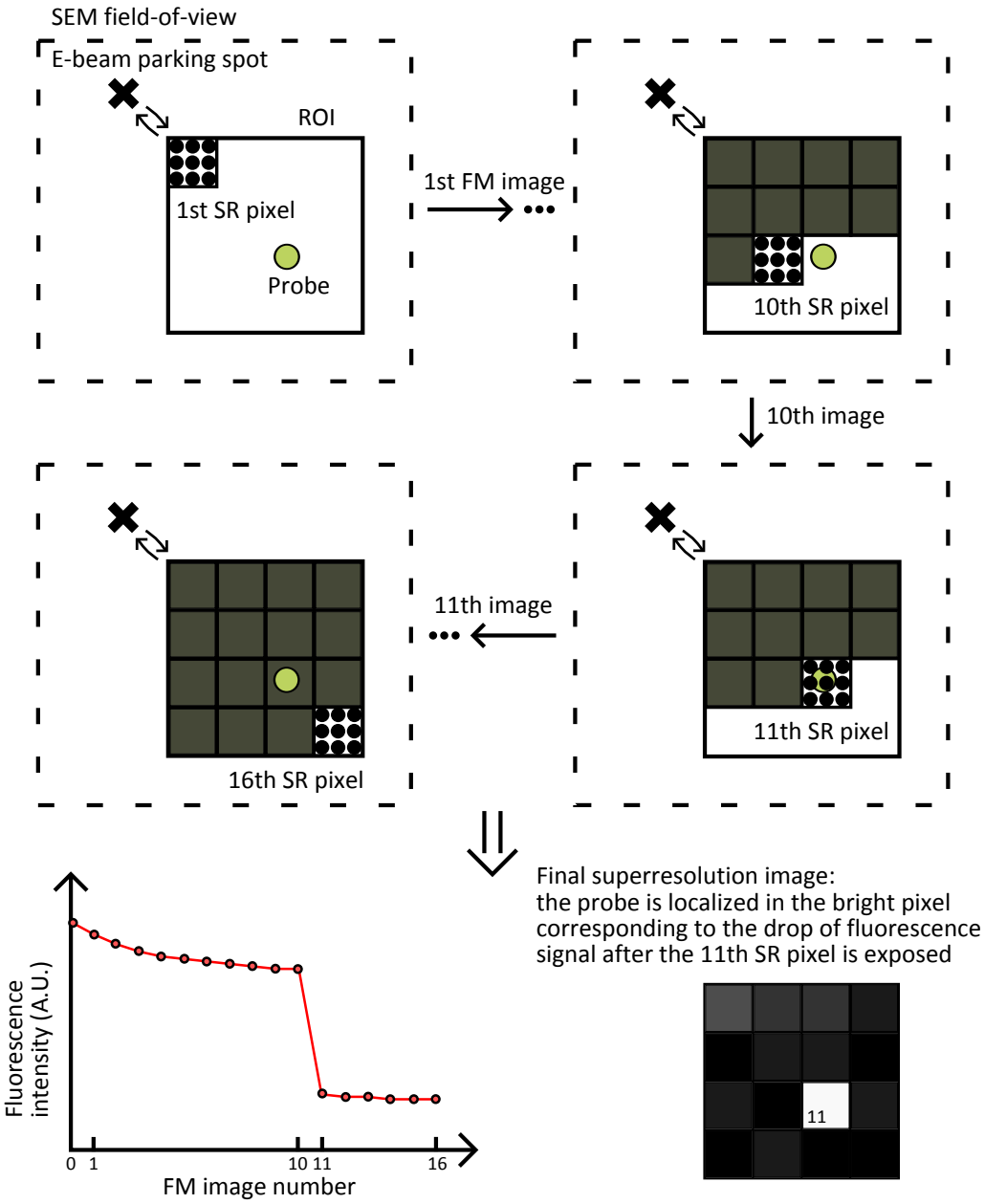

Figure 5.4: *Operational principle of the superresolution method. First, initial FM image is acquired prior to any electron exposure of the ROI. After that, the electron beam scans the ROI exposing it pixel by pixel, during which the fluorescence intensity is monitored. After each pixel, the electron beam moves back to the parking spot and another FM image is acquired. The electron-beam moves back and forth between the ROI and the parking spot until the whole ROI is scanned. Finally, an average fluorescence intensity is calculated over the ROI in the FM images. In this example, a fluorescent probe is located in the 11th SR pixel and a discrete drop can be observed in the fluorescence trace in the 11th image. The final superresolution image is reconstructed by plotting intensity difference between subsequent FM images in gray scale. Decay of the fluorescence trace starts already from the 1st image because of photobleaching, which determines the underlying baseline of the trace.*

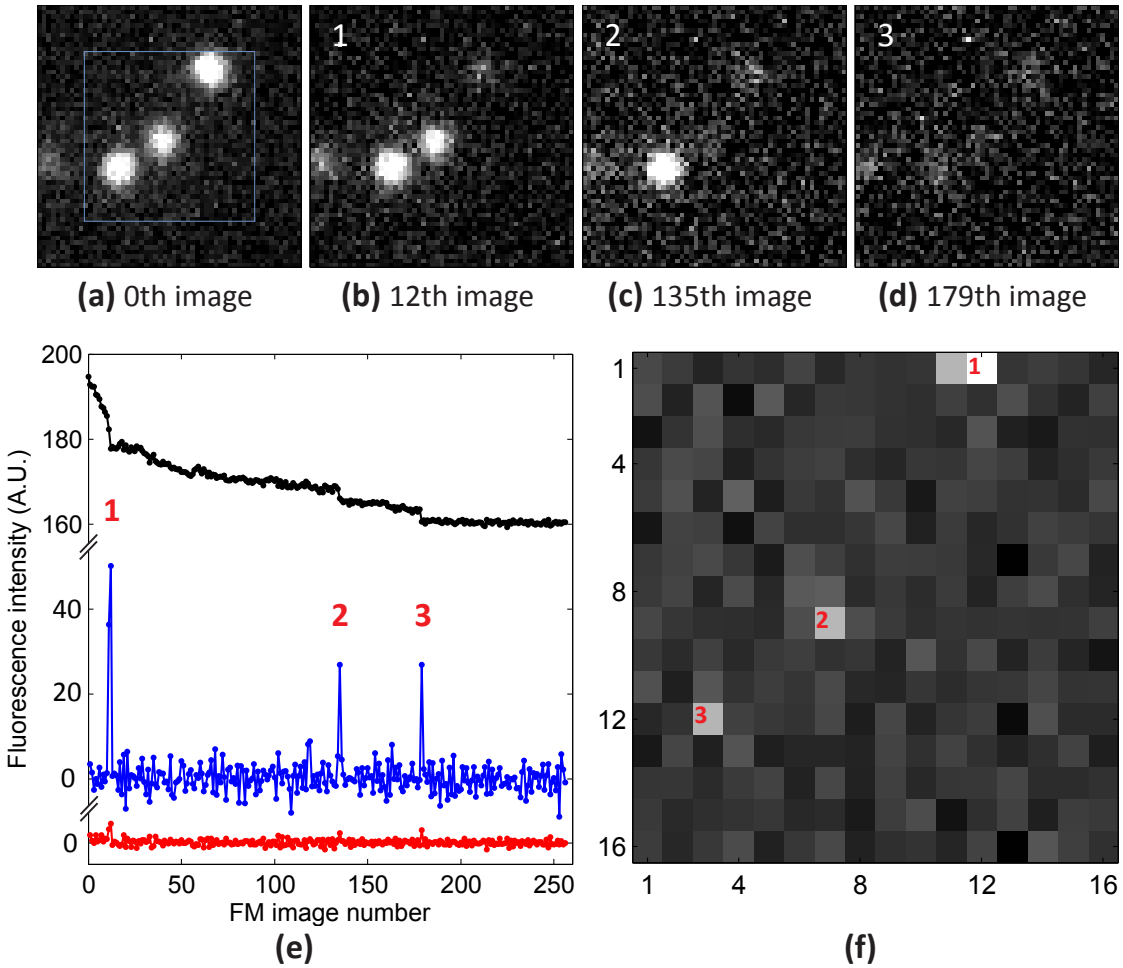

Figure 5.5: *Principle of the superresolution method demonstrated with real experimental data, having 250 nm SR pixel size. 0th image denotes the FM image acquired prior to electron exposure of the sample. FM images 1–3 corresponds to SR pixels where the fluorescence intensity drops due to bleaching of fluorescent probes. In (e), fluorescence intensity trace is plotted in black, which is an average intensity calculated over the whole ROI from the FM images. The derivative of the trace is calculated as an absolute difference in the intensity value, between subsequent data points. The negative derivative is plotted with a red curve showing peaks corresponding to the steps clearly visible in the fluorescence trace. The blue curve represents absolute changes in fluorescence intensity calculated with so-called spatial filtering, which is illustrated in Figure 5.6. A great improvement is obtained in the signal-to-noise ration: SNR of 2.2 and SNR of 5.5 are obtained for the derivatives without and with spatial filtering, the red and blue curves, respectively. (f) shows the reconstructed gray scale superresolution image. Numbers 1–3 connect the FM images to the corresponding steps in fluorescence trace, and furthermore to the peaks in the derivative and bright pixels in the SR image.*

So far changes in fluorescence intensity have been evaluated by calculating average intensities over the whole ROI. However, when fluorescent probes are bleached, the change in the average intensity of the whole ROI is much smaller

than the change in the pixels of the corresponding fluorescence spot. Furthermore, the electron beam can modify the fluorescent properties of the sample only in a small area around the focus. Therefore, to improve the SNR of the fluorescence trace derivative, average intensities can be calculated over only a certain amount of pixels around the known electron-beam location in the FM image. This is referred to as spatial filtering of the signal and it significantly improves the SNR. In the example in Figure 5.5, approximately 2.5-fold increase is observed. The final superresolution image, shown in Figure 5.5f, is reconstructed from the spatially filtered data (blue curve), having much less noise than the SR image without spatial filtering (not shown).

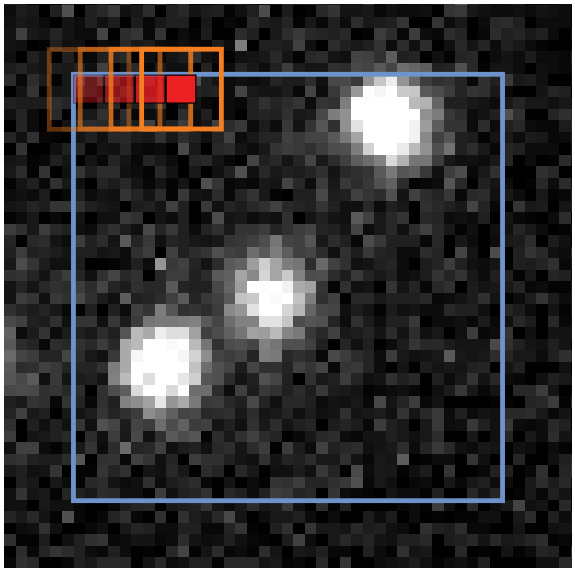

Figure 5.6: *Illustration of the spatial filtering of fluorescence intensity in the FM image. Blue square indicates the ROI, over which the average intensity is calculated in the first place (fluorescence trace). Small red squares indicate the superresolution pixels scanned by the e-beam, and the orange squares around them depict the filter areas, over which the average intensity is calculated before and after the corresponding SR pixel is exposed. The color gradient visualizes the subsequent filter positions. Spatial filtering can drastically improve the signal-to-noise ratio of the fluorescence trace derivative, especially when the ROI is much larger than the typical filter size of 7 x 7 pixels (750 x 750 nm), and the ROI contains several fluorescence spots as in this case.*

Spatial filtering is further clarified in Figure 5.6, which indicates the first few SR pixels with red squares, and the spatial filter around them with orange squares. Typically an area of 7 x 7 pixels in the FM image is taken into account, corresponding to approximately 750 x 750 nm square on the sample, as the FM image pixel size with 60 x magnification is 108 x 108 nm. Spatial filtering requires a good

alignment precision of the optical and electron axis because we need to know the e-beam position in the FM image very accurately, to locate our filter around that spot. In principle, the alignment precision should be on the order of the FM image pixel size.

We have now learned how the optical superresolution image is acquired. However, the main advantage of the method is that the SEM image of the specimen can be acquired at the same time. In principle, the SEM image could be reconstructed from the SE/BSE signal of the specimen during the SR pixels are scanned by the electron beam. Unfortunately, it was noticed in the experiments, that at this point such low electron doses bleach the fluorescent probes, and the idea is to not completely bleach the probes in only a single pass, that the electron emission signal is too low to obtain a nanometer scale SEM resolution. Therefore, in the superresolution experiments of this work, the SEM image is acquired separately, after the actual superresolution procedure is run. The SEM image is of course required for revealing the ultrastructure in correlative imaging, but in our experiments it also has a crucial function to confirm the locations of the fluorescent probes on the sample. The method must be able to reliably find the fluorescent probes in the locations found in the SEM image. Another reliability check is that the probes are found in the same SR pixels in subsequent scans of the ROI, which indeed requires incomplete bleaching of the probes in a single scan.

Post processing of the data, such as extraction of the intensity values from the FM images without and with spatial filtering, and reconstruction of the final superresolution image, was all done with a MATLAB script which can be distributed on request.

5.3 Practical implementation

In this section, we go through the practical implementation of the superresolution method, meaning the control and automation of the method with a Python script. Furthermore, some advanced details of the experimentation are discussed, and practical tips are given along the way. The Python script applies existing functions of Odemis (Open Delmic Microscope Software), and it communicates with the SEM controller box, the Zyla sCMOS camera and the Lumencor LED-source. The SEM controller box drives the scanning coils of the SEM, and it also receives the data from SE/BSE detectors. The Python script was written with a help from Delmic. Here, we do not go into the details how the Odemis functions work, but

rather focus on providing the required understanding that the user needs to run the script and thus employ the superresolution method. A detailed documentation of the Odemis environment can be found elsewhere [65].

First of all, before the ROI is chosen from the FM image, the magnification of the SEM must be adjusted such that the SEM field-of-view is larger but on the same order of magnitude as the desired size of the ROI. The ROI should not be bordering the top-left corner of the SEM field-of-view because the parking spot of electron beam is relatively close to the top-left corner, and we want to minimize any additional exposure of the ROI while e-beam is waiting at the parking spot. In addition, magnification sets the lowest limit for e-beam step size because the maximum SEM image resolution with the Odemis SEM controller is limited to 4096 x 4096 pixels. The magnification value must be the same in both Odemis and the FEI user interface, when the FEI software is in the full-screen mode.

After the magnification is chosen, the ROI is defined by setting the left, top, right and bottom (LTRB) borders of the ROI relative to the SEM field-of-view, as a form of [L T R B]. The origin of the coordination system is the top-left corner, and [0 0 1 1] implicates the whole SEM field-of-view. For instance, the ROI of [0.5 0.5 0.7 0.7] implicates 0.2 x 0.2 fraction of the field-of-view having the top-left corner in the middle.

In the script, the ROI is divided into superresolution pixels which are then scanned with a certain e-beam step size. In other words, every SR pixel is further divided into sub-pixels which are then exposed by the electron beam with a certain dwell time. The SR pixel size is defined in nanometers and the dwell time in seconds. The SEM controller box currently limits the dwell time to a lowest value of 800 ns. The e-beam step size, i.e. the size/separation of the sub-pixels, must be defined as the total amount of sub-pixels inside one SR pixel. Only square shape SR pixels are supported, and therefore the sub-pixel amount must be also a square of an integer.

The procedure can be automatically run multiple times over the same ROI, also with different dwell time in each pass if desired. The dwell time and the e-beam step size can be separately defined for the SEM image acquisition, subsequent to the actual superresolution procedure. At the moment, the final SEM image is typically acquired with a very long dwell time of ≥ 100 µs, such that all the fluorescent probes in the ROI are fully bleached afterwards. The final SEM image is also acquired one SR pixel at a time, which actually turns out to be beneficial

for correlation of the final SR and SEM images, because borders of the SR pixels show up in the SEM images (see e.g. Figure 6.1).

Finally, the exposure light power and sCMOS camera exposure time are defined in watts and seconds, respectively, from which the exposure time is defined in Odemis even though it could easily be implemented as a script argument as well. The script can be run from the computer terminal by command

```
./sem_bleaching_map.py
--dt 0.8e-6 --dtsem 100e-6 --pxs 108
--subpx 49 --stepsize 2025 --roi 0.4,0.4,0.6,0.6
--lpower 0.4 --output ~/Foldername/filename.h5,
```

where --dt, --dtsem, --pxs, --subpx, --stepsize, --roi, --lpower and --output represent the arguments: dwell time, dwell time for final SEM image, SR pixel size, amount of sub-pixels, amount of sub-pixel for final SEM image, definition of ROI, exposure light power and output file, respectively. The argument values here are a typical example of real values used in the experiments. The script saves each FM image to its own .h5-file, and in the end, the electron detector signal, fluorescence trace calculated from the whole ROI, the resulting SR image and the final SEM image to one final .h5-file. Here, .h5 is an extension of HDF5 (hierarchical data format), a versatile file format for complex scientific data [66].

The injected electron dose and electron landing energy have the main influence in electronbleaching rate. The electron dose per area is determined by the electric current, dwell time and electron-beam step size (see Eq. 4.3). The landing energy, on the other hand, is determined by the acceleration voltage and possible (negative) stage bias, applied to the stage holder in the SEM/SECOM. The stage bias was implemented in the SECOM platform from the original voltage source of the Verios 460, and connected to the sample holder ring via a coaxial cable with a piece of carbon tape. An insulating teflon spacer was placed between the holder ring and the stage (see Figure 5.2d).

Each SR pixel is scanned with sub-pixels to obtain a uniform electron dose distribution over the sample, thus to make sure that all the probes receive an equal amount of dose. The uniformity of the distribution depends on the effective electronbleaching spot size, which is certainly larger than the focal spot of the electron beam. Here, the distribution is considered uniform if each 40 nm polymer bead gets directly hit multiple times by the electron beam. However, the step size can-

not be chosen arbitrarily because it also affects the total electron dose of the sample. Hence, a step-size around 15 nm is typically chosen, because it makes low doses easier to reach, still ensuring multiple hits per polymer bead. In addition, the spatial dose distribution seems to have an influence to the electronbleaching rate (see Section 4.3.4), but in here it is not considered because adjusting the total dose has much greater importance.

Finally, a few words concerning the alignment procedure. As we have learnt in Section 5.1, once the SEM is focused with desired electric current and beam energy, and optical focus is found, the optical axes needs to be aligned to the electron axis. In the SECOM platform this is done by imaging cathodoluminescence of the glass substrate. However, the CL signal becomes very weak at low currents and landing energies. Long integration times of the sCMOS camera and manual adjustment of the contrast is required to be able see the CL spot, and at 1 keV and with less than 6 pA, it becomes nearly impossible. Moreover, on TEM-girds, the CL generation of the Formvar polymer membrane is even lower.

The issue was overcome by the following two means. With FEI Verios 460, an approximate alignment could be performed with higher current/landing energy, because the e-beam spot did not move much while changing the current or acceleration voltage, due to excellent internal alignment of the SEM. Furthermore, with the TEM-grid samples, the electron beam induced compounds in the Formvar membrane to become fluorescent, such that the light objective could be aligned to the middle of the exposed rectangle visible in the FM image. However, in neither case the fine alignment procedure could be run.

5.4 Samples

First samples for the superresolution experiments are similar to the samples used in the characterization study. The samples consist of fluorescent polymer beads (TransFluoSpheres 488/645) dispersed on an ITO-coated glass substrate. The samples were prepared with exactly the same procedure as explained in Section 4.1. Only the concentration of the beads was substantially reduced to obtain distinguishable diffraction limited spots in the fluorescence image. For that, the salt-free polymer bead solution was further diluted to 1/500 concentration of the stock solution.

Secondly, the superresolution experiments are performed with other test samples consisting of TransFluoSpheres on TEM-grid substrates, on top of a 30–60 nm

thick Formvar polymer membrane. The TEM-grids have a thickness of 18 μm, a standard diameter of 3.05 mm, and they are made of nickel. The Formvar membrane on top of the grid consists of polymers formed from polyvinyl alcohol and formaldehyde. These samples were prepared together with our collaborator[1] as discussed below.

Ultrathin tissue sections of a pancreas of a diabetic-rat were placed on top of the TEM-grids and labelled with red-emission quantum dots, as well as with our fluorescent polymer beads. Immunolabelling with primary and secondary antibodies was applied. The secondary antibodies were conjugated with biotin to enable binding of streptavidin conjugated quantum dots or TransFluoSpheres 488/645 (polymer beads). FM and SEM images are shown in Chapter 2 of a tissue-section where insulin granules are labelled with the quantum dots. Specific labelling with the polymer beads actually failed but a suitable concentration of the beads could still be found in the tissue, and importantly also outside the tissue, on the Formvar membrane. These "failed" samples were still applicable for our superresolution experiments, as at the current state, we are developing the method from the technical/physical point-of-view. The idea of course was that the method could be tested and demonstrated on real biological specimens, too, but this remains for future research.

The ITO-glass samples were attached to the SECOM holder ring with small pieces of conductive carbon tape, whereas the TEM-grid samples were placed on top of an empty ITO-glass slip and fixed with a piece of carbon tape from top. No carbon tape could be put between the TEM-grid and the glass substrate because then the grid would then stand too high for the light objective to reach the focus. Because the TEM-grids are nickel which is a magnetic material, they really need to be fixed to the sample holder. Otherwise the magnetic fields in the immersion mode of the SEM could flip the sample.

[1] Cellular Imaging group at the Department of Cell Biology, Faculty of Medical Sciences, University of Groningen

CHAPTER 6

Results

This chapter presents the results obtained with the superresolution method developed in this Master's thesis. Experiments are performed on test samples, and the method is demonstrated to work on both ITO-coated glass and TEM-grid substrates. The aim is to find the optimal conditions to enable as small SR pixel size as possible, as that determines the image resolution of the method. Furthermore, reliable localization of the probes requires confirmation of the probe locations by multiple scans of the ROI. Thus, the electron dose needs to be adjusted so that the probes are not fully bleached during the first pass. A more comprehensive discussion on the current state of development and recommendations for future study can be found towards the end of the chapter.

6.1 TransFluoSpheres on ITO-glass in FEI Quanta SEM

Initially, superresolution experiments were performed with the SECOM platform on the FEI Quanta scanning electron microscope, having TransFluoSpheres (fluorescent polymer beads) on an ITO-glass substrate. We begin with a landing energy of 1 keV, as that beam energy is assumed to provide the best ratio of in-focus/out-of-focus bleaching (see Section 3.2). The FM image pixel size is 108 nm in all experiments, determined by the sCMOS camera pixel size of 6.5 μm and objective-lens magnification of 60 x. The SR pixels size is always chosen as a multiple or common fraction of 108 nm for easier comparison. Excitation wavelength of 475 nm is applied, provided by blue LED of the Lumencor SPECTRA light engine.

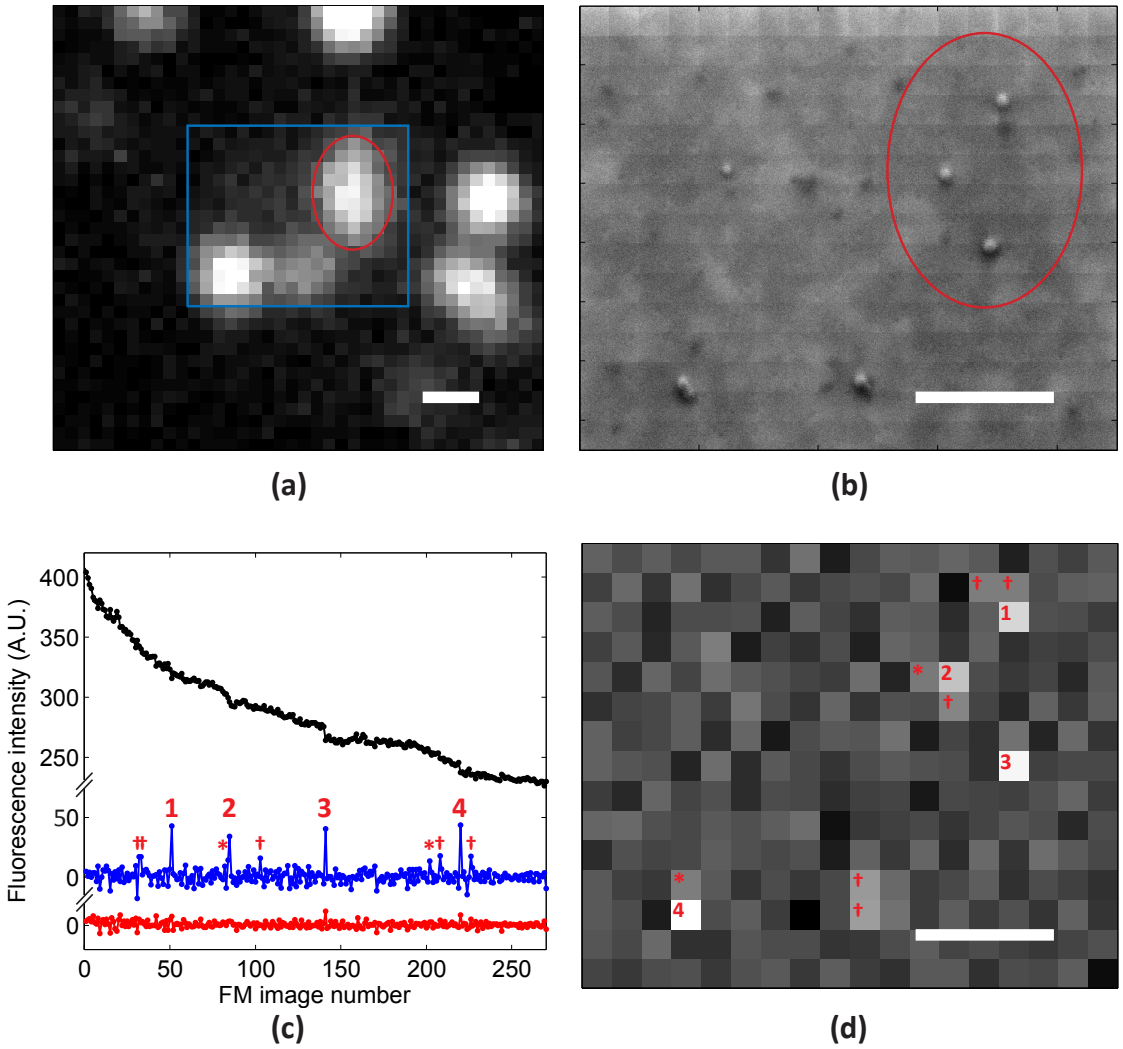

Figure 6.1: *Results for Experiment 2307_f. (a) shows the initial FM image where the ROI is indicated with a blue rectangle. (b) shows the corresponding SEM image acquired afterwards. Absolute alignment is missing between the FM image and the exposed ROI because the SECOM's fine alignment procedure could not be run with such a low landing energy and electric current. Here, the ROI is located in the FM image according to the particle locations in the SEM image. In this experiment, three individual beads were found inside one diffraction limited spot surrounded by the red ellipses in (a)-(b). The ellipses are in scale. (c) shows the fluorescence trace with black curve, and the derivative of the signal without and with spatial filtering, plotted with a red and blue curve, respectively. Daggers denote peaks >2σ above the baseline but not as high as the four main peaks. Stars denote peaks that are just below the 2σ-level, but because the corresponding SR pixels are next to higher peaks in the 2-dimensional configuration, they can be considered as real signals. (d) shows the reconstructed SR image, with the main peaks denoted with 1–4, and smaller peaks denoted with daggers and stars. Here, the following exposure settings were applied: SR pixel size of 108 nm, landing energy of 1 keV, electric current of 6 pA, dwell time of 1.6 μs, e-beam step-size of 15.43 nm, electron dose of 0.25 e/nm^2, excitation light power of 400 mW (nominal), light exposure time of 3 s and SEM magnification of 30 000 x (8.53 μm field-of-view). Each scale bar in (a),(b) and (d) is 500 nm.*

Figure 6.1 presents the results of Experiment 2307_f where three individual beads were resolved inside one diffraction limited fluorescence spot, with a 108 nm SR pixel size. In total, five polymer beads were found with the method. The peaks in the spatially filtered fluorescence trace derivative (blue curve) are determined by assuming Gaussian (normally distributed) noise and calculating the standard deviation of the derivative. Standard deviation σ can be applied as a confidence level for event occurrence, and $\sigma = 7.15$ is obtained in this case. We set a confidence level of 2σ for peak identification, meaning that if the derivative value is greater than 2σ, a peak is detected. Here, 2σ confidence level corresponds to only 2.3% chance that the detected peak would be produced by random noise. The peaks above that level are therefore considered real signals due to electronbleaching of fluorescent probes. Here, the calculated standard deviation is slightly biased because also the actual peak values are included in the calculation. However, it only makes the confidence level a bit higher.

The peaks are denoted with numbers 1–4 (main peaks, $>3\sigma$), with daggers (still $>2\sigma$) and stars (close to 2σ). The peak locations in the final SR image are indicated with the same markers. A good correspondence is found between the SR and SEM image. Borders of SR pixels are visible in the SEM image because the SEM image is acquired identically to the actual superresolution procedure, one SR pixel at a time. The actual reason, why this produces visible squares around the SR pixels, is not fully understood but it can be related to pronounced contamination due to slight overlap between the SR pixels, or extra time spend at the end of scan lines by the electron beam. The small bead located top-left in the SEM image shows no fluorescence and is therefore not found with the method. Experiment 2307_f firmly confirms that our superresolution method can operate with a resolution beyond the diffraction limit of light. The final SR image is overlaid on the initial wide-field FM image for comparison in Figure 6.2.

Here, the locations of the probes are confirmed by the SEM image to prove that the method works. However, the main idea of optical superresolution is that the fluorescent probes can be found in the specimen independently, to provide additional functional information, i.e. the probe locations, that cannot be found in the SEM image. In real samples the fluorescent probes do not generally light up in the EM image. Reliable localization of the probes requires that the method finds the probes in the same locations with multiple passes. If the probes are fully bleached during the first pass, there is no way to prove that the suggested

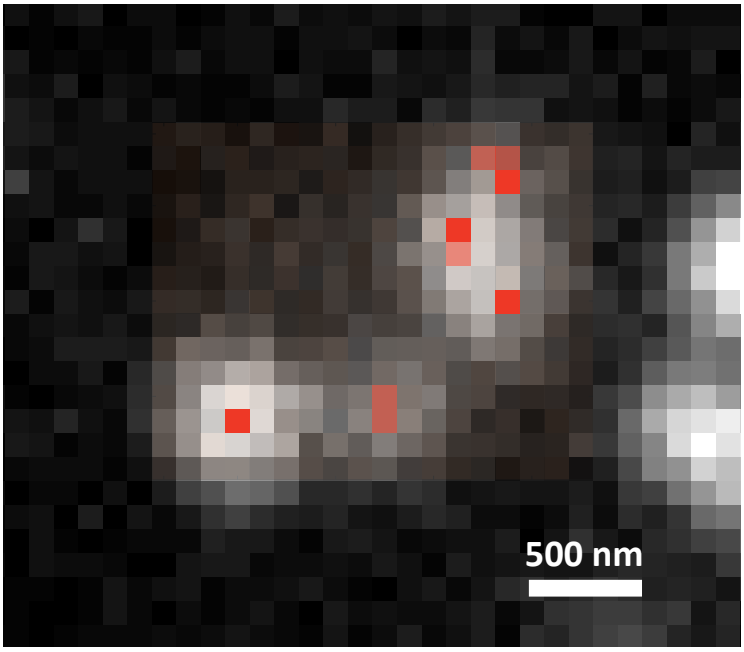

Figure 6.2: *The final SR image of Experiment 2307_f overlaid on the initial FM image for comparison. The superresolution method provides resolution significantly better than that of the wide-field fluorescence microscope. The SR image is made nearly transparent but the pixels corresponding to the main peaks ($>3\sigma$) and the other peaks above the 2σ-level are coloured dark and light red, respectively. Absolute overlap calibration of the FM and SR image pixels is missing because the SECOM's fine alignment procedure could not be run with such a low landing energy and electric current.*

locations are correct. If the dose has been much too high, the probes might have been fully bleached due to out-of-focus bleaching already far before the electron beam was actually at the true probe locations.

Figure 6.3 presents the fluorescence traces and corresponding derivatives of two experiments: Experiment 2307_d and Experiment 2307_n, where the ROI was scanned multiple times. In Experiment 2307_d, the ROI was scanned ten times with a 216 nm SR pixel size. All subsequent passes are combined into a one total fluorescence trace in Figure 6.3a, where each of the first two passes shows a large sudden drop in the intensity trace after 18th SR pixel, but even passes 8–10 find the probe in the same location. The localization is further confirmed with the subsequently acquired SEM image, which reveals a double-bead in the 18th SR pixel. Surprisingly, some passes in between do not show any modification of the intensity level. This might be because electronbleaching is a random process, and the dose that sometimes bleaches the fluorophores might sometimes not induce any changes in the molecular configurations. The randomness becomes more

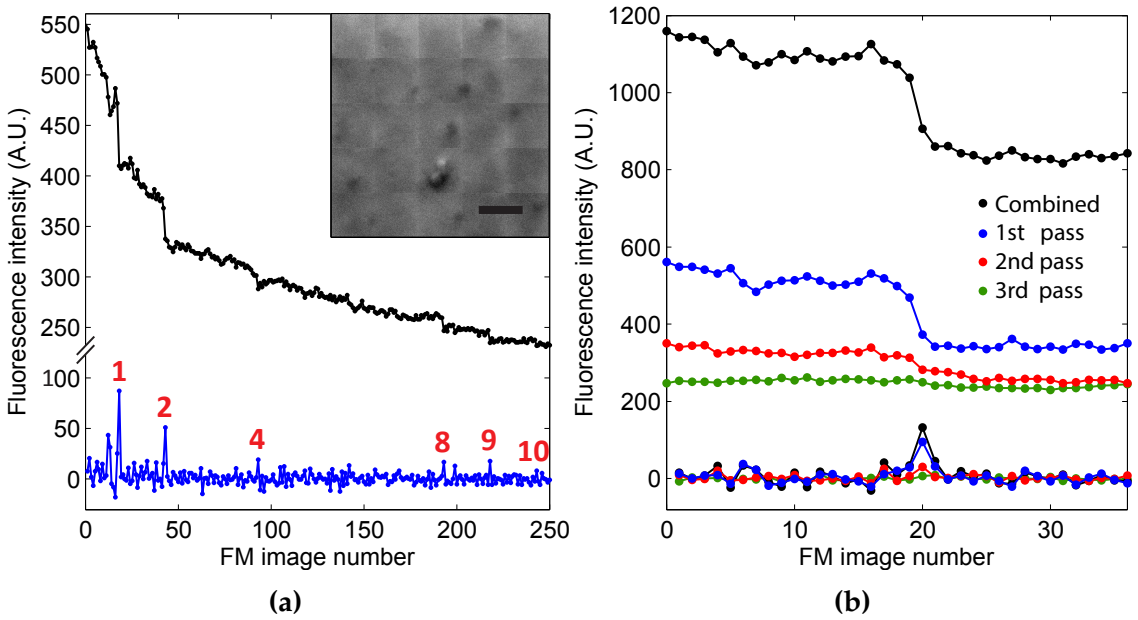

Figure 6.3: *(a) shows the intensity traces of Experiment 2307_d where the ROI is scanned 10 times with a 216 nm SR pixel size. Numbers 1–10 denote the steps in the intensity level in the corresponding pass. Not every pass has an influence to the fluorescence intensity. The inset shows the SEM image of the ROI, which reveals a double-bead inside the 18th SR pixel. (b) presents the intensity traces of Experiment 2307_n having three passes over the ROI with a 108 nm step size. The drop in fluorescence intensity is found at the same SR pixel by the 1st and 2nd scan, confirming the location of the probe. Here, the following exposure settings were applied in both (a) and (b): SR pixel size of 216/108 nm, landing energy of 1 keV, electric current of 6 pA, dwell time of 800 ns, e-beam step-size of 15.43 nm, electron dose of 0.13 e/nm^2, excitation light power of 400 mW (nominal), light exposure time of 3 s and SEM magnification of 30 000 x (8.53 µm field-of-view).*

prominent after most of the fluorescent molecules are already destroyed. This kind of behaviour might also be related to the complexity of the fluorescence cycle in our multi-dye-doped polymer beads. Nevertheless, it further verifies that multiple passes are required to obtain reliable probe localization. The underlying shape of the fluorescence trace indicates quick photobleaching of the beads under vacuum conditions.

Figure 6.3b shows an experiment where a fluorescent bead is found in the same SR pixel by two subsequent passes, with a 108 nm pixel size, after which the bead is fully bleached and only flat intensity trace is observed during the 3rd pass. During the 1st pass, a particular profile can be observed of the trace when the intensity drops: bleaching starts already one pixel earlier and still continues one pixel after the largest step. This implies that the effective bleaching spot size

with the corresponding exposure settings on an ITO-glass substrate is larger than 108 nm.

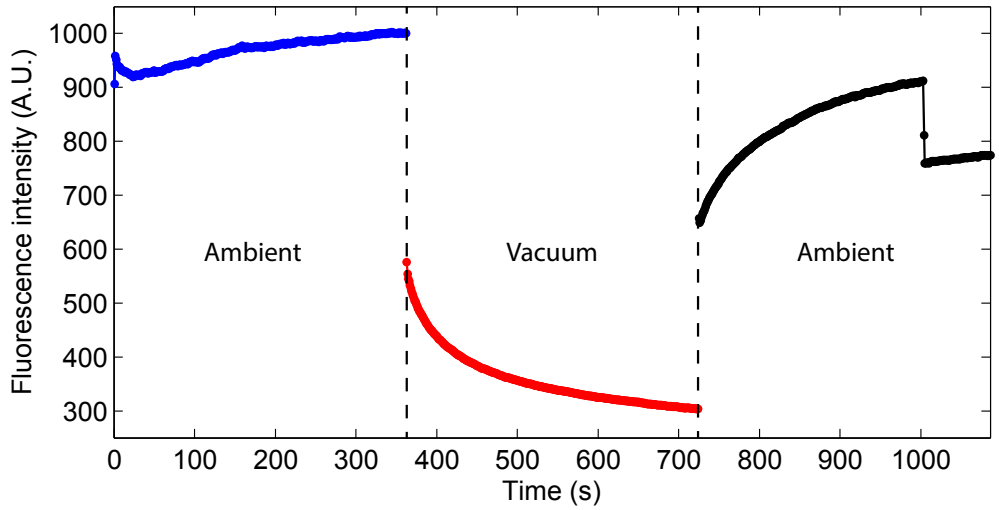

Figure 6.4: *Photobleaching of the fluorescent polymer beads in the ambient and under vacuum conditions. The fluorescence intensity is monitored from exactly the same sample area. Photobleaching is very quick in vacuum (red curve), but it is reversible as can be see from the black curve. Already the starting level of the fluorescence intensity is much lower in vacuum. The degraded fluorescence is certainly a major drawback for our experiments. The reason for the sudden drop in the black curve is an unknown and is considered as an artifact, even though similar drops have been observed in other experiments as well (not shown).*

The fluorescent polymer beads are extremely photostable in the ambient conditions but show a very peculiar behaviour in vacuum, as their photobleaching becomes highly pronounced (cf. the general trend underlying bleaching curves in Figures 6.1 and 6.3). Only contrary studies can be found in the literature as has been discussed in Chapter 3: photobleaching processes typically involve oxygen species that are not present in vacuum. Experimental data of photobleaching is presented in Figure 6.4, where subsequent images are acquired of the same sample area with the full excitation light power of 400 mW and exposure time of 1 s. The peculiar behaviour may be explained by fluorescence intermittency, where the power-law distributed on/off-times result in increasing on- or off-times depending on the initial conditions (see Section 3.1). Fluorescence intermittency would also explain the photobrightening/recovery once the sample is brought back to the ambient. It might be that the dye molecules inside the polystyrene sphere transfer to a dark state that quickly relaxes in air but very slowly in vacuum. The relaxation process might involve an oxygen species or air humidity that

assists in a charge transfer process and the return back to the molecular ground state. Moreover, because already the starting level of fluorescence intensity is much lower in vacuum than in the ambient, maybe some of the non-radiative transitions between linked dye-molecules inside the sphere become very unlikely due to similar reasons. Nevertheless, quick photobleaching under vacuum conditions is a major drawback for our superresolution experiments, because it significantly reduces the fluorescence signal, i.e. the photon count obtained per fluorescent particle.

6.2 TransFluoSpheres on TEM-grid in FEI Verios SEM

In this section, the results are presented from superresolution experiments performed with the SECOM platform on FEI Verios 460, having fluorescent polymer beads on a TEM-grid substrate, on top of a 30–60 nm Formvar polymer membrane. In all the experiments below, the ROI is restricted just around one diffraction limited spot in the fluorescence image. The ROI has typically dimensions of around 1 x 1 μm, and hence spatial filtering is not applied. In principle, the spatial filtering works fine also with small ROIs but it is not advantageous either (typical filter size being 700–800 nm). In the experiments with the Verios, we had significant issues with drift during the measurements, and the alignment of the electron and optical microscope was generally not good. Therefore, the monitored area, from which the fluorescence intensity is calculated, is defined manually in the FM image and kept constant around the fluorescence spot. In all the experiments below, the following exposure parameters were applied: landing energy of 1 keV, negative stage bias-voltage of 1 kV, excitation wavelength of 475 nm, light power of 400 mW (nominal), light exposure time of 2 s and SEM magnification of 40 000 x (corresponding to field-of-view of 10.4 μm). The SR pixels size, electric current, dwell time and e-beam step-size were varied between the experiments, yielding also different electron doses of 0.1–0.5 e/nm^2.

Figure 6.5 shows the results from Experiment 2209_q which is similar to the one presented in Figure 6.3b, but now on a TEM-grid in the Verios with a negative stage bias of 1 kV. Here, a 108 nm SR pixel size was applied and two subsequent passes were made by doubling the dose (dwell time) for the second pass. That was done because electronbleaching results in an exponential-like decay of the fluorescence intensity (see Section 4.3.1) and to obtain a detectable step in the fluorescence trace also during the second scan, it is favourable to increase the

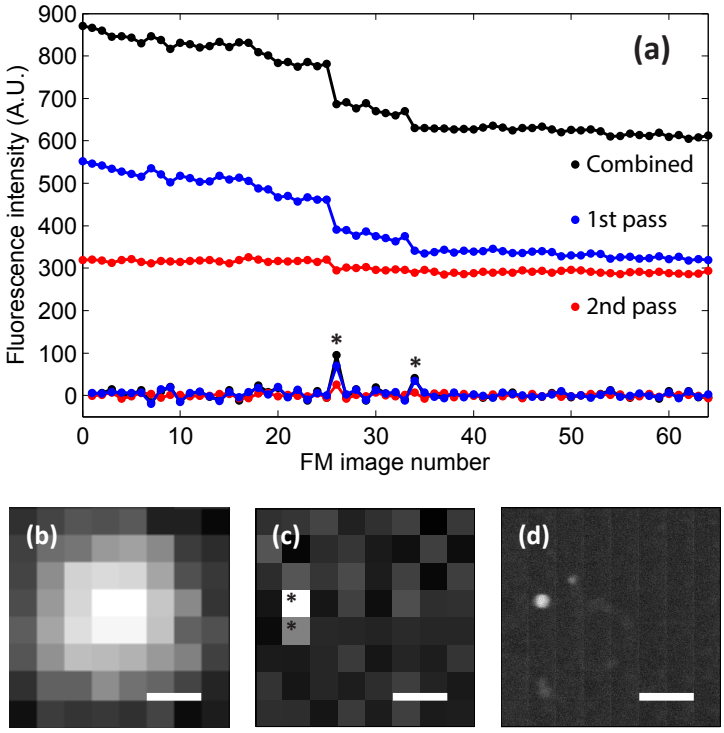

Figure 6.5: *Results of Experiment 2209_q. (a) shows the fluorescence trace and its derivative for the 1st and 2nd pass, plotted with blue and red curves, respectively. The combined trace and derivative are plotted with black curves. The bead is localized in the same SR pixel with both passes and a clear main peak occurs in the derivatives. However, the first pass produces also another peak, and bright a pixel next to the main peak (both peaks denoted with stars). (b) represents the fluorescence spot in the 0th FM image. The monitored area corresponds to this cropped FM image. (c) shows the final SR image of the combined data. (d) represents the corresponding SEM image. The scale bars in (b)-(d) are 216 nm, corresponding to 2 x SR pixel size. The ROI was centered to the fluorescence spot in the FM image but the bead is not found in the center of the SR image implying misalignment between the electron and optical microscope. Here, the following exposure settings were applied: SR pixel size of 108 nm, electric current of 6.3 pA (nominal), dwell time of 1.2/2.4 µs (1st/2nd pass), e-beam step-size of 15.43 nm, yielding electron dose of 0.20/0.40 e/nm^2.*

electron dose. Here, both passes located an individual fluorescent bead in the same SR pixel. By combining (summing) the trace and trace derivative of the two passes, the probe location becomes even more prominent. However, more information is available in the SR image as the first pass produces a drop in intensity also at the SR pixel just below the brightest one. It could be therefore assumed that the bead is located close to the edge of these two pixels (stars in Figure 6.5c). However, the SEM image suggests the opposite, meaning that the bead would be near the top edge of the brightest pixel. Drift may explain this deviation between the SR and SEM image, but one must be careful in interpreting the SR images in

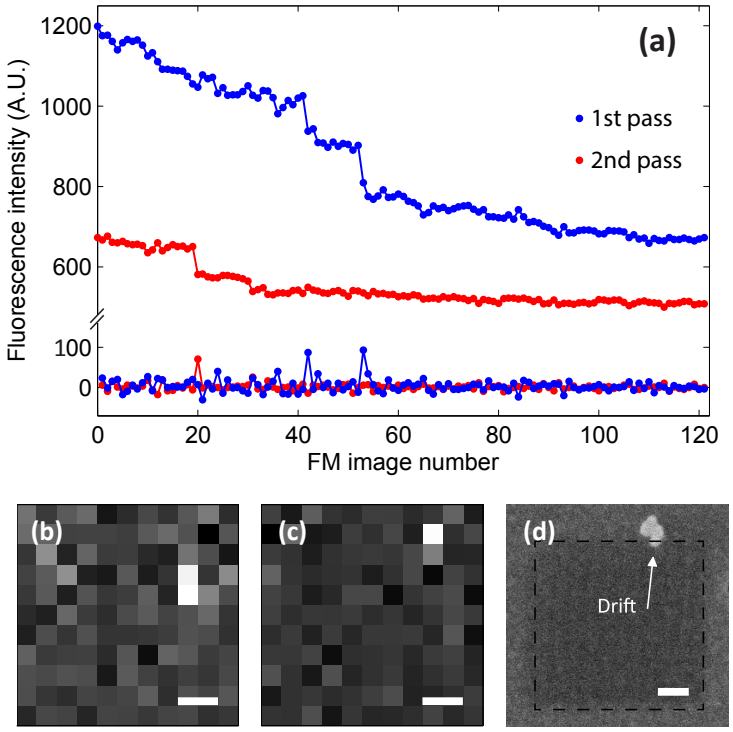

Figure 6.6: *Results of Experiment 2409_f. (a) shows the fluorescence traces and derivatives. (b) shows the SR image of the 1st pass and (c) that of the 2nd pass. (d) presents a subsequent manually acquired SEM image of the sample, where the ROI is depicted with a black dashed square and the drift direction is indicated with an arrow. The scale bars in (b)-(d) are 162 nm. Here, the following exposure settings were applied: SR pixel size of 81 nm, electric current of 6.3 pA (nominal), dwell time of 1.2/2.4 µs (1st/2nd pass), e-beam step-size of 16.2 nm, yielding electron dose of 0.18/0.36 e/nm^2.*

general. Here, for instance, an increase before the second drop in the fluorescence trace makes to drop more pronounced. It is the noise in fluorescence intensity that makes it challenging to reliably tell where the fluorescent probe is exactly located, at least within several adjacent bright pixels.

Figure 6.6 presents Experiment 2409_f showing the drift issue mentioned above. Here, the sample stage and/or electron beam was drifting during the measurement adding difficulty to the interpretation of the data. A cluster of beads was localized nicely with a 81 nm SR pixel size, by two subsequent passes, but the locations differ due to systematic drift indicated in the subsequent SEM image.

Figure 6.7 shows Experiment 2209_g where three-bead cluster could be localized inside a single 108 nm SR pixel by two subsequent scans. The location is confirmed by the subsequent SEM image. No drifting occurred this time. The experiment demonstrates that if the fluorescent probe is very bright, such as here

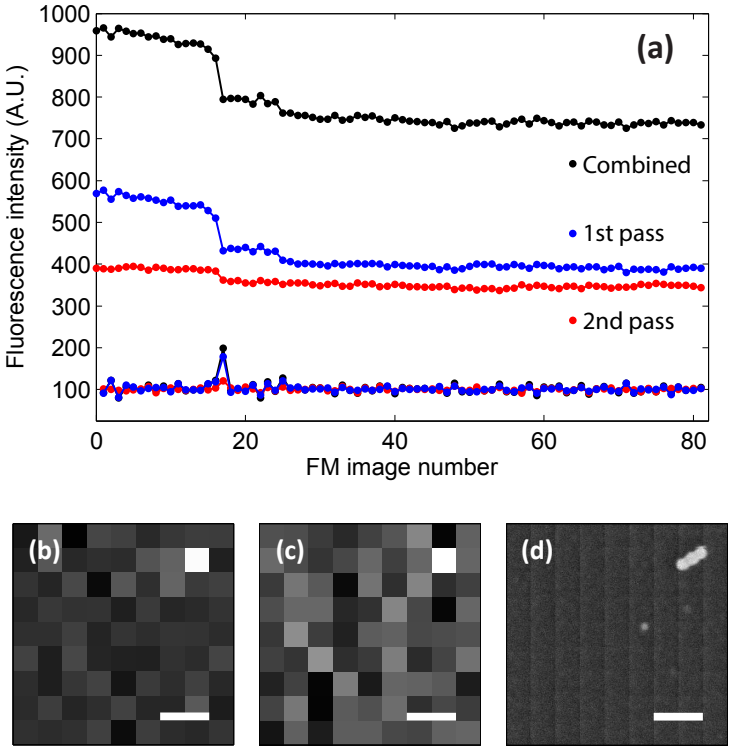

Figure 6.7: *Results of Experiment 2209_g. (a) shows the fluorescence traces and derivatives. (b) shows the SR image of the 1st pass and (c) that of the 2nd pass. (d) shows the subsequent SEM image of the ROI. The experiment shows very convincing localization of the probe-cluster inside a single SR pixel. The scale bars in (b)-(d) are 216 nm. Here, the following exposure settings were applied: SR pixel size of 108 nm, electric current of 13 pA (nominal), dwell time of 1.2 µs (both passes), e-beam step-size of 15.43 nm, yielding electron dose of 0.41 e/nm^2.*

the three beads together, the localization becomes fairly easy. Moreover, with a larger ensemble of dye-molecules, also the relative variation of the fluorescence emission (noise) becomes a little less prominent.

Figure 6.8 presents Experiment 2309_g with only a 54 nm SR pixel size. Now the peaks in the trace derivative are very much embedded under the noise level, even though the steps are clearly visible in the intensity trace itself. This is because now the contribution in bleaching is shared among several pixels. However, if the contribution of neighbouring pixels is added together, i.e. the derivative values are summed of pixels that are adjacent to each other in the two-dimensional configuration, the peaks are found again in the derivatives (see Figure 6.8b). We call this method binning, that is, adding values together of e.g. 2 x 2 pixels in the SR image.

It obviously matters which pixels are binned together: with the applied 2 x 2 bin-

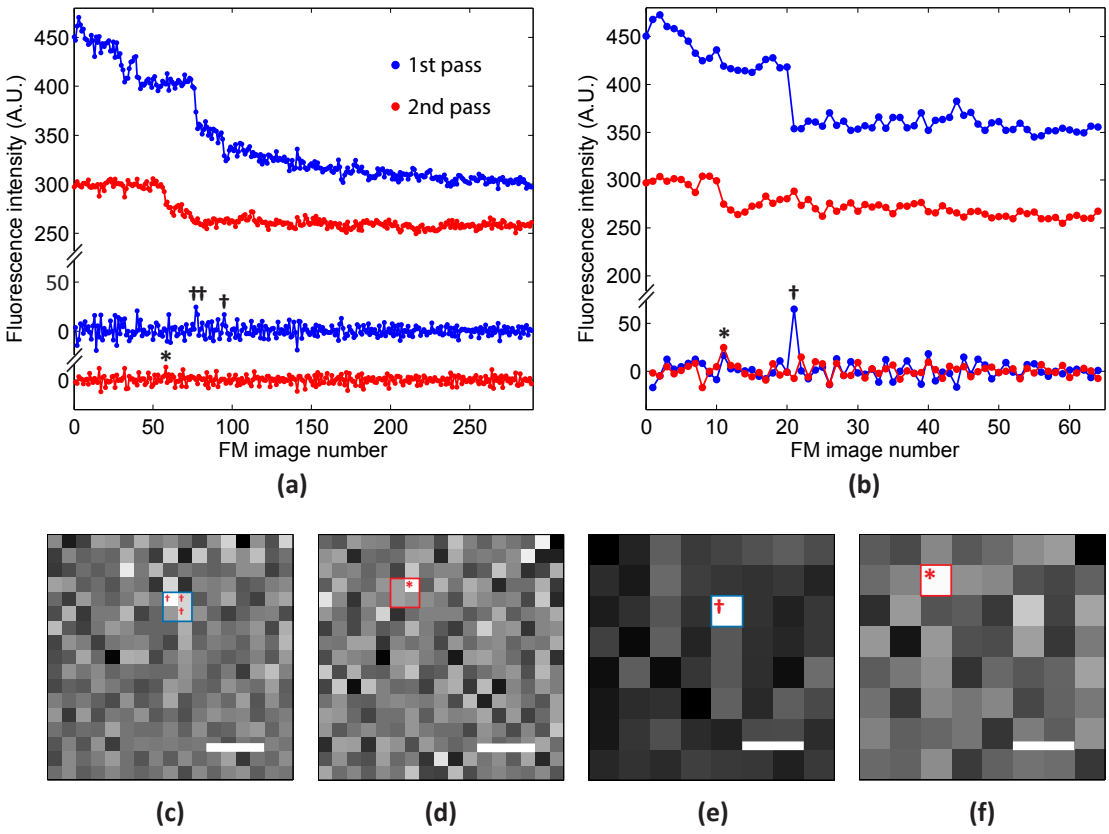

Figure 6.8: *Results of Experiment 2309_g with only 54 nm SR pixel size. (a) shows the fluorescence traces and derivatives. The contribution of individual SR pixels is embedded under the noise level but a clear steps are still visible in the traces. (b) shows the same data with the binning of 2 x 2 pixels. Clear peaks can be found again in the derivatives for both the 1st and the 2nd pass. (c)-(d) show the SR images of the 1st and 2nd pass, respectively. (e)-(f) show the SR images of the 1st and 2nd pass, with 2 x 2 pixel-binning. The daggers and stars connect the derivative peaks to the SR pixels. The subsequent SEM image is not shown because the ROI had drifted away and no particle was present in the image. However, a manually acquired SEM image is presented in Figure 6.9. The scale bars in (c)-(f) are 216 nm corresponding to 4 x SR pixel size. Here, the following exposure settings were applied: SR pixel size of 54 nm, electric current of 6.3 pA (nominal), dwell time of 2/4 µs (1st/2nd pass), e-beam step-size of 18 nm, yielding electron dose of 0.24/0.49 e/nm^2.*

ning there are four different options. Here, all possible options are calculated, and the ones showing highest peaks in derivative are presented in Figures 6.8b,e-f. The binned pixels showing up bright in the resulting SR images are connected to the locations in the original SR images with coloured squares. The pixel-binning is a tool to find approximate location of the probes, and the fine localization must be performed in the original SR images, which for this experiment is done in Figure 6.9 for the 1st pass. Here, the 1st and 2nd passes would ultimately be added together, as has been done in some of the experiments above, but because of drift

between that passes, no additional information could be obtained .

It is noticed here that standard deviation is not the best measure for the noise level as it greatly underestimates it. The noise level does not stay constant during the measurement but varies a lot, and the large occasionally occurring noise peaks make the identification of the true signals a difficult task. The noise level variation is most likely related to fluorescence intermittency of the dye-molecules. Here, the SNR is calculated by comparing the highest peak value (corresponding to the step in the fluorescence trace) to the mean value of the three next highest (noise) peaks. Only $\mathrm{SNR} = 1.3$ is obtained for the 1st pass derivative, and $\mathrm{SNR} = 1.2$ for the 2nd pass derivative. For the binned data, we obtain $\mathrm{SNR} = 3.9$ (1st pass) and $\mathrm{SNR} = 2.8$ (2nd pass), which are already reasonable for peak detection. Hence, the probe(s) can be clearly localized within the binned 108 nm size pixels, and tracked back in the original SR image with a pixel size of 54 nm.

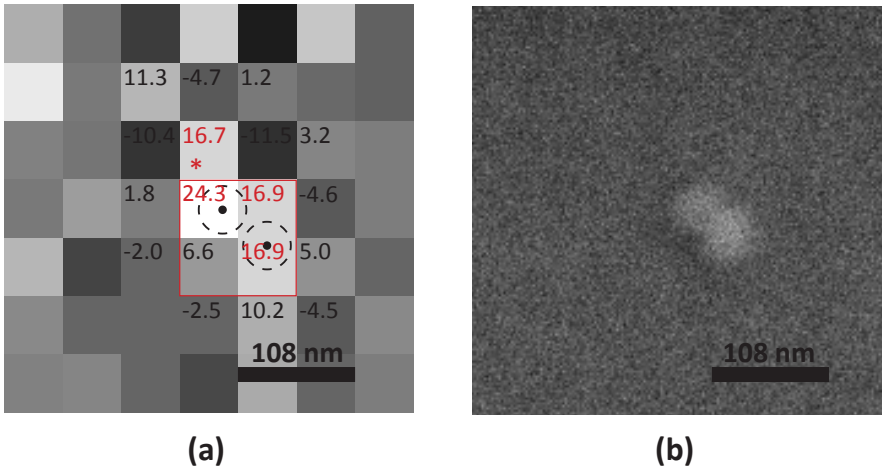

Figure 6.9: *SR image of the 1st pass in Experiment 2309_g with pixel weight-values, and a comparison to the SEM image. Pixels with red numbers denote the ones having intensity values larger than 50% of that of the brightest pixel. A double-bead is found in the SEM image. Two 45 nm spheres are shown in the SR image as an illustration but their position is not based on any weighted fitting. There should be no dark pixels with large negative values next to the bright pixels if they are based on true bleaching signals, because if there are, in such a case the change in the intensity is more likely due to the high-frequency noise (see the pixel denoted with a red star). The noise contribution can be estimated by comparing the absolute values of the subsequent SR pixels in the scanning order.*

In Figure 6.9, the weight-values for pixels around the approximate probe location are show in the non-binned SR image of the 1st pass in Experiment 2309_g. The SR image is compared to the SEM image of the corresponding sample area,

which reveals a double-bead. The red square corresponds to the pixel area that was binned in Figure 6.8. The fine-location of the beads can be estimated as depicted in the figure. The localization is not rigorous but it suggests that localization is feasible within several adjacent pixels based on their weights. This so-called sub-pixel localization is discussed more in Section 6.3, where the definition of the resolution of our method is also addressed, the definition of resolution being generally unambiguous. Here, we can claim that at least two fluorescent probes occur in the the depicted area, which is later confirmed by the SEM image.

Figure 6.10 presents Experiment 2409_k where several beads (a single bead and a cluster) could be resolved inside an elongated diffraction limited spot with a 81 nm SR pixel size, by two subsequent passes. Binning of 2 x 2 pixels is applied to confirm the locations of the probes. Drift is again clearly visible and noise is very apparent. One needs to keep in mind that it is better to look at the steps in the fluorescence traces, at which the total signal level drops, rather than the higher frequency variation of the signal.

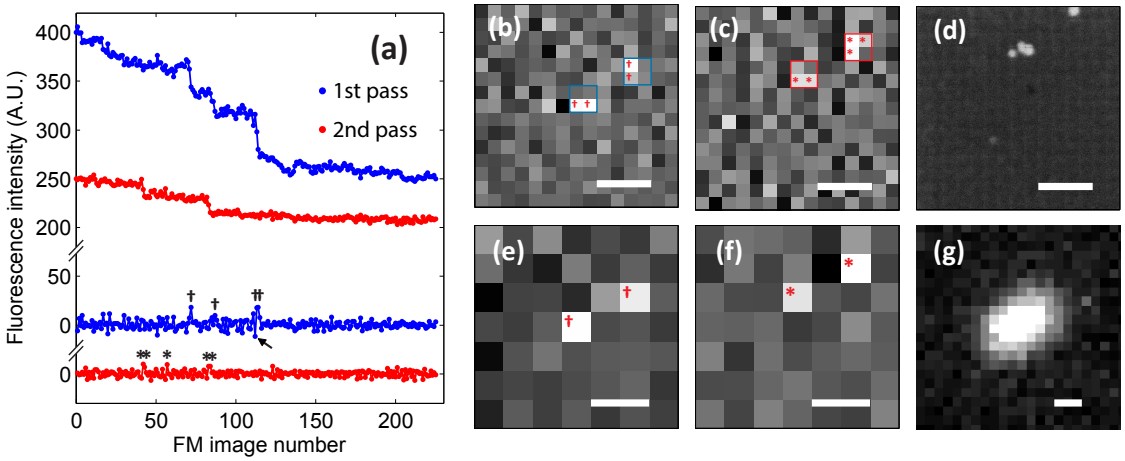

Figure 6.10: *Results of Experiment 2409_k. (a) shows the fluorescence traces and derivatives. (b)-(c) present the original SR images with a 81 nm pixel size. (e)-(f) present the SR images with 2 x 2 pixel-binning. (d) shows the SEM image, and (g) the initial FM image. The daggers and stars connect the derivative peaks to the SR pixels. In (a), the arrow indicates a major increase in the fluorescence intensity just before a drop, producing the black pixel before two bright ones in (b). It demonstrates how the noise plays a role in the SR image formation, and that it should be considered for developing means to find probe locations in a sub-pixel scale. The scale bars in (b)-(g) are 324 nm corresponding to a 4 x SR pixel size of 81 nm. Here, identical exposure parameters were applied as in Experiment 2409_f (Figure 6.6).*

6.3 Discussion and outlook

The obtained results successfully demonstrate the electronbleaching based superresolution method to work on the SECOM platform. Individual fluorescent probes could be resolved inside a diffraction limited spot in the FM image. The fluorescent polymer beads could be reliably localized with 54 nm SR pixel size, by two subsequent passes over the ROI. The results are very promising, especially because only little optimization of the method has been done so far. In this section, the experimental findings are discussed, underlying the challenges and recommendations for further study.

To be able to distinguish two probes in the superresolution image, there must be at least one dark pixel between the bright pixels indicating fluorescent probes. It directly follows that the image resolution cannot be better than 2 x SR pixel size. If the fluorescent probe happens to be just on the edge of two SR pixels, both pixels show up bright in the final SR image. If the probe occurs at the intersection of four adjacent pixels, they all should show up bright, if the electron dose is properly adjusted. In these cases, neighbouring probes at a distance of 2 x SR pixel size hardly yield a dark pixel between them, and they are impossible to resolve. The resolution limit of our method is conservatively approximated at 2.5 x SR pixel size, and localization precision equal to 2 x SR pixel size (see Figure 6.11) .

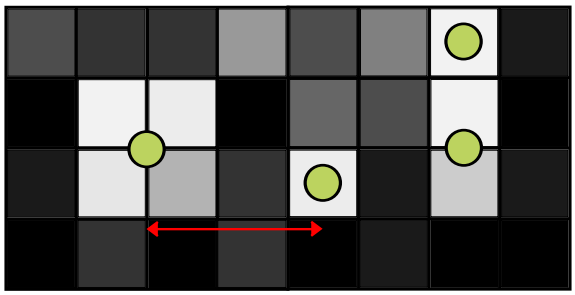

Figure 6.11: *A schematic illustration of the resolution limit of the method. If a fluoresent probe occurs at the edge/intersection of adjacent SR pixels, at least a distance of 2.5 x SR pixel size is required to distinguish the two neighbouring probes (red line). The localization precision is conservatively approximated at 2 x SR pixel size.*

The SR pixel size of 54 nm implies a 108 nm localization precision and approximately a 160 nm SR image resolution. However, the experiments suggest that localization precision equal to the SR pixel size could be feasible by weighted fitting of individual pixels around the detected probe location, which is confirmed

by pixel-binning (see Figures 6.8–6.9). This would yield localization precision comparable to the size of the fluorescent polymer bead. To obtain sub-pixel localization, suggested here, the bleaching profile of the electron beam must be considered. The effective bleaching profile of the electron beam, i.e. the effective dose distribution or the probing size, should be one of the first priorities for future research. By knowing how the bleaching rate/effective dose depends on the distance between the e-beam spot and the fluorescent probe, the accumulative dose per fluorescent probe could be calculated and exploited in the weighted fitting of multiple bright SR pixels. In addition, the SNR of the fluorescence trace derivative should be better than in the current experiments.

Every fluorescent molecule has an equal probability to switch off under an electron exposure, and from the characterization studies in Chapter 4 we know how much dose on average is required to bleach a polymer bead. However, when approaching the single emitter level, the blinking of fluorescent molecules starts to induce natural variation to the fluorescence signal. In our case, already an individual fluorescent particle is an ensemble of dye molecules, and blinking cannot be distinctly observed. However, the random emission statistics still produces noise which is the main limiting factor for the resolution, i.e. reduction of the SR pixel size and implementation of the weighted fitting discussed above. It is observed that with a small pixel size of <100 nm the modification of fluorescence intensity by the electron exposure of an individual pixel is easily embedded under the noise level. With a SR pixel size of 54 nm, the noise easily produces peaks that are of comparable height to the peaks produced by the steps of the total intensity level of the fluorescence trace (cf. pixels in Figure 6.9). It mainly results from the fact that with a small SR pixel size, the effective bleaching spot extends outside the pixel itself. Therefore, the decrease in fluorescence intensity is not abrupt but shared among several SR pixels, i.e. the effect per pixel diminishes.

The electronbleaching extending outside the SR pixel and the random intensity variation of fluorescence emission combined are the main limiting factors for the resolution of the method. These factors are connected such that if either one could be improved, it would enhance the resolution.

The experiments were performed with both ITO-glass and TEM-grid substrates. TEM-grids with a free-standing thin film on top were expected to alleviate out-of-focus bleaching because the electrons could just go through the film. However, the whole interaction volume of a 1 keV electron beam falls inside a 30–60 nm

thick Formvar membrane (see simulations in Chapter 3), and the behaviour of the two substrate types was not markedly different in the experiments. The use of TEM-grids did not result in significant improvement in the obtained SR pixel size. The simulated backscattering coefficient of ITO is $\sim$0.3, whereas that for Formvar is $\sim$0.07, implying less undesired scattering from the Formvar membrane in general. However, the ratio between electron emission rates will also need to be taken into consideration, and may well be of more importance given our observations on the influence of negative stage bias discussed below.

Better resolution was obtained on the TEM-grid samples, but also the microscope employed in the experiments was changed from FEI Quanta to FEI Verios 460, on which a negative stage bias-voltage could be applied. It was discovered that the stage bias might have an important role in alleviating out-of-focus bleaching of the probes. This is most likely due to the the negative potential of the stage which repels the scattered secondary electrons, expels them quickly from the sample surface, and therefore reduces their horizontal path length, along which they could walk around inducing electronbleaching. The electric field on the sample surface is determined by the applied stage bias, detector bias voltage, and the distances between different parts inside the SEM chamber. Without the stage bias, even the results with 108 nm SR pixel size were difficult to reproduce in the Verios due to an ambiguous out-of-focus bleaching of fluorescent beads, especially with the immersion mode on, immersion mode referring to the final magnetic lens extending down to the sample. Bleaching behaviour as a function of stage bias, without and with the immersion mode on, should be quantitatively studied in the future.

TEM-grids with ultrathin ($\sim$10 nm) films on top could be tried, such that most of the electrons go through without scattering in the substrate. On the other hand, with real tissue section samples, the tissue might be thick enough to absorb the electrons anyway. Furthermore, if the electrons would go through, an "electron trap" would be needed below the sample because otherwise the accumulative charge might cause troubles for the light objective. In this work, TEM-grids were placed on plain ITO-coated glass slips, but it is not the best option as some electron scattering from the ITO-glass might still induce out-of-focus bleaching. The electron trap could be a transparent conductive thin-film or a electrode with a bias voltage deflecting the transmitted electrons to the side, to protect the light objective and prevent any electron scattering form below the specimen. Higher

landing energy might be favourable on TEM-grids with a free standing thin-film: already 99% of the incident electrons go through 50 nm thick Formvar film at 5 keV beam energy (simulation not shown). On the other hand, the method was not experimented with <1 keV landing energies either. It is clear from the results in Section 4.3.3 that 1 keV is the most efficient energy to bleach the fluorescent beads, but it is not trivial that this particular beam energy would therefore also provide the best ratio of in-focus to out-of-focus bleaching.

Surprisingly, and very unfortunately, the photobleaching of our fluorescent polymer beads is highly pronounced under vacuum conditions. Furthermore, the fluorescence recovers when the sample is brought back to the ambient conditions, implying that the photobleaching in vacuum is reversible. The polymer bead consists of fluorescent molecules embedded in a polymer matrix, the exact configuration that has been shown to support long-lived metastable dark states (see Section 3.1). It might be that the lack of humidity or oxygen in vacuum drastically increases the lifetime of metastable dark states, as charge dissipation becomes more difficult. Additionally, the rate of non-radiative energy transfer between the primary and secondary dyes might be reduced due to similar reasons. The complexity of the fluorescence process in our current polymer beads and their very undesired photobleaching behaviour in vacuum suggests that other probes should be investigated for superresolution experiments in the immediate future.

Besides optimization of the exposure parameters and substrate, optimization of the fluorescent probes should be the main development path in future study. The probe needs to be photostable and bright under vacuum conditions. Furthermore, it should be as "electronstable" as possible, such that it does not fully bleach under low electron dose exposure. This would aid in specific electron bleaching just in focus of the electron beam, i.e. narrowing down the effective bleaching profile. In general, if higher doses could be used, also the SEM detector signal might become high enough to enable a genuinely simultaneous acquisition of the SEM image. However, to obtain a high-resolution SEM image of the biological tissues, much higher currents of >100 pA are typically required (SEM image of the tissue in Figure 2.11 was acquired with 400 pA). If the superresolution image is acquired with different exposure settings, it is challenging to keep a perfect overlap between the FM and SEM images. It requires a very good alignment of the SEM, such that the e-beam spot location stay constant while changing the

beam parameters.

Ultimately, the probes could be switched reversibly off, or even be excited with the electron beam to reverse the whole method by monitoring cathodoluminescence of the probes. With quantum dots, this might be possible, and they are potential probe candidates for the method. Typically quantum dots are very photostable and some quantum dots are shown to exhibit purely exponential "on"- and "off"-time distribution instead of the power law distribution [67]. It would make the distinguishing of electron-beam induced signal more plausible, as statistical aging would not increase the "off"-period during the measurement. In the future study, it is advised to employ smaller probes, also with two or more different colors to demonstrate the full potential of the method.

The electron doses used in the superresolution experiments were very low compared to the ensemble bleaching curves shown in Section 4.3.1. However, the conditions in the experiments were very different as well. In the characterization experiments, the FM imaging was performed in the ambient, a long time (hours) after electron exposure in the SEM. It is advised to study the bleaching behaviour solely under vacuum conditions, by automated time-lapse experiment in the SECOM platform where the same sample area is exposed a bit by bit while monitoring the fluorescence intensity. The same sample area could be also checked in the ambient afterwards.

Finally, recommendations are given to improve the practical implementation of the method. The SEM controller box currently limits the e-beam dwell time to a lowest value of 800 ns, which makes the experiments difficult as very low currents are required to obtain the required electron dose range. Furthermore, because the electron-beam is kept on all the time during the measurement, the ROI is exposed with additional dose while the beam moves back and forth over the ROI, to the parking spot. Implementation of a beam blanker would solve the issue with unnecessary exposure of the ROI, as the beam could be blanked during the FM image acquisition, not just moved to the side. SEM controller boxes that enable dwell times of <100 ns are commercially available. However, both issues could be solved at the same time with a blanker that enables control over the beam in nanosecond time-scales, such that the blanker could be used to ration the dose injection into the sample.

In the latter experiments, the stability of the system caused difficulties as the sample stage and/or the beam drifted over time (see e.g. Figure 6.6). A drift

correction may be required to keep the registry between the FM and SEM images, especially if the SEM image is acquired after the actual SR imaging where the SR pixels are exposed with a much lower electron dose. At the moment, the whole optical field-of-view is exposed while acquiring the FM images. It could be restricted especially if photobleaching is an issue, e.g. by confocal means. To speed up the investigation of large sample areas, multiple ROIs could be scanned simultaneously, parallel to each other. The time consuming part in the method is not the e-beam scanning but the FM acquisition, which requires exposure time of seconds. In contrast, e-beam scanning of an SR pixel takes typically less than 100 μs.

CHAPTER 7

Conclusion

In this Master's thesis, an electron-beam-induced optical superresolution method is demonstrated to operate beyond the diffraction limit of light. The method is applied in an integrated light-electron microscope platform (SECOM, Delmic) with which the electron and optical imaging can be performed simultaneously, keeping the region-of interest stationary in the field-of-view of both microscopes. The method is demonstrated with 40 nm fluorescent polymer beads (TransFluoSpheres 488/645, Molecular Probes) on both ITO-coated glass and TEM-grid substrates.

The method is based on electronbleaching of fluorescent probes. It acquires the information of probe locations by switching them "off" with the electron beam, the position of which is known at nanometer scale accuracy. The electronbleaching rate of the fluorescent beads mostly depends on the injected electron dose and electron landing energy. The dose dependence of the fluorescence intensity can be approximated with a single-exponential decay. When the beads are exposed with a constant dose but varying the electron landing energy, a clear minimum of the remaining fluorescence can be found around 1 keV, implying that the most efficient bleaching occurs at that energy. At that energy, the interaction volume of the electron beam corresponds to the size of the polymer bead. Interestingly, spatial dose distribution, meaning the e-beam step-size, has an influence on the bleaching rate with a constant dose per area. In contrast, the electric current and temporal distribution of the dose show little influence.

In the superresolution (SR) experiments, individual fluorescent probes could be resolved inside a diffraction limited spot in the fluorescence microscopy (FM) image with a SR pixel size of 108 nm, on an ITO-glass substrate. A cluster of

two beads could be reliably localized with a 54 nm SR pixel size, by two subsequent passes over the ROI on a TEM-grid substrate, implying a localization precision of 108 nm and image resolution of approximately 160 nm, the definition of resolution being 2.5 x SR pixels size. The resolution obtained is well beyond the resolution limit of the conventional wide-field FM employed in the SECOM platform. Furthermore, the obtained results suggest that a localization precision equal to the SR pixel size is feasible, which with the current state of the experiments implies a precision comparable to the size of the fluorescent polymer bead. To confirm such a localization precision, however, further investigation of the effective bleaching profile of the electron beam, and the development of means to reliably find the weight center among several SR pixels, are required.

The SEM image of the sample is acquired right after the actual electron bleaching procedure. As both FM and SEM images are based on the electron-beam position on the sample, in the SEM coordinate system, it yields intrinsically perfect spatial overlap of the optical information and the ultrastructure. The intrinsic correlation between the FM and SEM images is the main advantage of the method. However, the stability of the system must be improved and/or a drift correction implemented to reliably keep the overlay accuracy, as long as the SEM image cannot be recorded genuinely from the SEM signal during the bleaching procedure.

The developed method may eventually become a very useful tool for researchers doing correlative light-electron microscopy, and it could be applied especially to ultrathin tissue-section imaging in cell and molecular biology. However, the method needs a considerable amount of further development and optimization to become applicable for a non-specialist user. There are three parallel approaches that should be taken in the future development: 1. Finding the optimal exposure setting to minimize the out-of-focus bleaching of fluorescent probes, including the optimization of the substrate and studying the influence of negative stage bias-voltage. In addition, the effective bleaching profile of the electron beam should be investigated. 2. Optimization of the fluorescent probes. The probes should be photostable under vacuum conditions (no photobleaching and little blinking), as well as electronstable, such that relatively high doses could be applied without fully bleaching the probes. In addition, the future probes should be much smaller than the currently used 40 nm polymer beads. Quantum dots might be good candidates for this purpose. 3. Implementation of hardware that enables short dwell times of <100 ns and e-beam blanking during the experiment.

References

[1] R. Yuste, "Fluorescence microscopy today," *Nature Methods*, vol. 2(12):902–904 (2005).

[2] B. N. G. Giepmans, T. J. Deerinck, B. L. Smarr, Y. Z. Jones, and M. H. Ellisman, "Correlated light and electron microscopic imaging of multiple endogenous proteins using Quantum dots," *Nature Methods*, vol. 2(10):743–749 (2005).

[3] G. M. Gaietta, B. N. G. Giepmans, T. J. Deerinck, W. B. Smith, L. Ngan, J. Llopis, S. R. Adams, R. Y. Tsien, and M. H. Ellisman, "Golgi twins in late mitosis revealed by genetically encoded tags for live cell imaging and correlated electron microscopy," *PNAS*, vol. 103(47):17777–17782 (2006).

[4] A. A. Mironov and G. V. Beznoussenko, "Correlative microscopy: a potent tool for the study of rare or unique cellular and tissue events," *Journal of Microscopy*, vol. 235:308–321 (2009).

[5] S. Watanabe, A. Punge, G. Hollopeter, K. I. Willig, R. J. Hobson, M. W. Davis, S. W. Hell, and E. M. Jorgensen, "Protein localization in electron micrographs using fluorescence nanoscopy," *Nature Methods*, vol. 8(1):80–84 (2011).

[6] B. G. Kopek, G. Shtengel, C. S. Xu, D. A. Clayton, and H. F. Hess, "Correlative 3D superresolution fluorescence and electron microscopy reveal the relationship of mitochondrial nucleoids to membranes," *PNAS*, vol. 109(16):6136–6141 (2012).

[7] N. Liv, A. C. Zonnevylle, A. C. Narvaez, A. P. J. Effting, P. W. Voorneveld, M. S. Lucas, J. C. Hardwick, R. A. Wepf, P. Kruit, and J. P. Hoogenboom, "Simultaneous Correlative Scanning Electron and High-NA Fluorescence Microscopy," *PLOS ONE*, vol. 8(2) (2013).

[8] C. J. Peddie, K. Blight, E. Wilson, C. Melia, J. Marrison, R. Carzaniga, M.-C. Domart, P. O'Toole, B. Larijani, and L. M. Collinson, "Correlative and integrated light and electron microscopy of in-resin GFP fluorescence, used to localise diacylglycerol in mammalian cells," *Ultramicroscopy*, vol. 143:3–14 (2014).

[9] A. C. Zonnevylle, R. F. C. Van Tol, N. Liv, A. C. Narvaez, A. P. J. Effting, P. Kruit, and J. P. Hoogenboom, "Integration of a high-NA light microscope in a scanning electron microscope," *Journal of Microscopy*, vol. 252(1):58–70 (2013).

[10] DELMIC BV, *SECOM platform, http://delmic.com/secom.php* (Accessed: Aug 12th, 2014).

[11] M. Haring, *High Resolution Correlative Light and Electron Microscopy*, Master's thesis, Delft University of Technology (2014).

[12] L. Novotny and B. Hecht, *Principles of Nano-Optics*, 2nd ed. (Cambridge University Press, 2012).

[13] P. Atkins and R. Friedman, *Molecular Quantum Mechanics*, 5th ed. (Oxford University Press, 2011).

[14] P. F. Bernath, *Spectra of Atoms and Molecules*, 2nd ed. (Oxford University Press, 2005).

[15] Franck-Condon principle, *Wikipedia article, http://en.wikipedia.org/wiki/Franck-Condon_principle* (Accessed: Aug 12th, 2014).

[16] J. R. Lakowicz, *Principles of Fluorescence Spectroscopy*, 3rd ed. (Springer, 2006).

[17] R. M. Dickson, A. B. Cubitt, R. Y. Tsien, and W. E. Moerner, "On/off blinking and switching behaviour of singlemolecules of green fluorescent protein," *Nature*, vol. 388:355–358 (1997).

[18] L. Song, E. J. Hennink, I. T. Young, and H. J. Tanke, "Photobleaching Kinetics of Fluorescein in Quantitative Fluorescence Microscopy," *Biophysical Journal*, vol. 68:2588–2600 (1995).

[19] Semrock, Inc., *Semrock Filter Sets, http://www.semrock.com/sets.aspx* (Accessed: Aug 22th, 2014).

[20] T. Kogure, S. Karasawa, T. Araki, K. Saito, M. Kinjo, and A. Miyawaki, "A fluorescent variant of a protein from the stony coral Montipora facilitates dual-color single-laser fluorescence cross-correlation spectroscopy," *Nature Biotechnology*, vol. 24(5):577–581 (2006).

[21] Carl Zeiss AG, *Confocal Laser Scanning Microscope LSM 710, http://www.zeiss.com/microscopy/en_de/products/confocal-microscopes/confocal-microscopy-lsm-710.html* (Accessed: Aug 22th, 2014).

[22] F. Helmchen and W. Denk, "Deep tissue two-photon microscopy," *Nature Methods*, vol. 2(12):932–940 (2005).

[23] P. Theer, M. T. Hasan, and W. Denk, "Two-photon imaging to a depth of 1000 μm in living brains by use of a Ti:Al_2O_3 regenerative amplifier," *Optics Letters*, vol. 28(12):1022–1024 (2003).

[24] B. N. G. Giepmans, S. R. Adams, M. H. Ellisman, and R. Y. Tsien, "The Fluorescent Toolbox for Assessing Protein Location and Function," *Science*, vol. 312(5771):217–224 (2006).

[25] Molecular Probes, Inc., Invitrogen Detection Technologies, *Product information: TransFluoSpheres Fluorescent Microspheres* (2005) http://www.lifetechnologies.com/order/catalog/product/T10711.

[26] E. Abbe, "Beiträge zur Theorie des Mikroskops und der mikroskopischen Wahrnehmung," *Archiv für Mikroskopische Anatomie*, vol. 9(1):413–468 (1873).

[27] Nikon MicroscopyU, The Source for Microscopy Education, *The Diffraction Barrier in Optical Microscopy, http://www.microscopyu.com/articles/superresolution/diffractionbarrier.html* (Accessed: Aug 26th, 2014).

[28] L. Shao, B. Isaac, S. Uzawa, D. A. Agard, J. W. Sedat, and M. G. L. Gustafsson, "I^5S: Wide-Field Light Microscopy with 100-nm-Scale Resolution in Three Dimensions," *Biophysical Journal*, vol. 94:4971–4983 (2008).

[29] B. Huang, M. Bates, and X. Zhuang, "Super-Resolution Fluorescence Microscopy," *Annual Review of Biochemistry*, vol. 78:993–1016 (2009).

[30] S. W. Hell and J. Wichmann, "Breaking the diffraction resolution limit by stimulated emission: stimulated-emission-depletion fluorescence microscopy," *Optics Letters*, vol. 19(11):780–782 (1994).

[31] T. A. Klar and S. W. Hell, "Subdiffraction resolution in far-field fluorescence microscopy," *Optics Letters*, vol. 24(14):954–956 (1999).

[32] M. Hofmann, C. Eggeling, S. Jakobs, and S. W. Hell, "Breaking the diffraction barrier in fluorescence microscopy at low light intensities by using reversibly photoswitchable proteins," *PNAS*, vol. 102(49):17565–17569 (2005).

[33] E. Betzig, G. H. Patterson, R. Sougrat, O. W. Lindwasser, S. Olenych, J. S. Bonifacino, M. W. Davidson, J. Lippincott-Schwartz, and H. F. Hess, "Imaging Intracellular Fluorescent Proteins at Nanometer Resolution," *Science*, vol. 313:1642–1645 (2006).

[34] M. J. Rust, M. Bates, and X. Zhuang, "Sub-diffraction-limit imaging by stochastic optical reconstruction microscopy (STORM)," *Nature Methods*, vol. 3(10):793–795 (2006).

[35] S. T. Hess, T. P. K. Girirajan, and M. D. Masony, "Ultra-High Resolution Imaging by Fluorescence Photoactivation Localization Microscopy," *Biophysical Journal*, vol. 91:4258–4272 (2006).

[36] M. Bates, B. Huang, and X. Zhuang, "Super-resolution microscopy by nanoscale localization of photo-switchable fluorescent probes," *Current Opinion in Chemical Biology*, vol. 12(5):505–514 (2008).

[37] M. Bates, B. Huang, G. T. Dempsey, and X. Zhuang, "Multicolor Super-Resolution Imaging with Photo-Switchable Fluorescent Probes," *Science*, vol. 317(5845):1749–1753 (2007).

[38] L. Reimer, *Scanning Electron Microscopy: Physics of Image Formation and Microanalysis*, 2nd ed., edited by P. W. Hawkes (Springer, 1998).

[39] FEI Company, *An Introduction to Electron Microscopy* (Booklet, 2010) http://www.fei.com/introduction-to-electron-microscopy/student-resources/.

[40] P. de Boer, J. P. Hoogenboom, and B. N. G. Giepmans, "Correlated light and electron microscopy: From basics to biology / Ultrastructure lights up!" (Submitted, 2014).

[41] J. B. Pawley, ed., *Handbook of Biological Confocal Microscopy*, 3rd ed. (Springer, 2006).

[42] L. A. Deschenes and D. A. V. Bout, "Single molecule photobleaching: increasing photon yield and survival time through suppression of two-step photolysis," *Chemical Physics Letters*, vol. 365:387–395 (2002).

[43] E. J. Sánchez, L. Novotny, G. R. Holtom, and X. S. Xie, "Room-Temperature Fluorescence Imaging and Spectroscopy of Single Molecules by Two-Photon Excitation," *Journal of Physical Chemistry A*, vol. 101(38):7019–7023 (1997).

[44] C. Eggeling, J. Widengren, R. Rigler, and C. A. M. Seidel, "Photobleaching of Fluorescent Dyes under Conditions Used for Single-Molecule Detection: Evidence of Two-Step Photolysis," *Analytical Chemistry*, vol. 70(13):2651–2659 (1998).

[45] G. Donnert, C. Eggeling, and S. W. Hell, "Major signal increase in fluorescence microscopy through dark-state relaxation," *Nature Methods*, vol. 4(1):81–86 (2007).

[46] E. Füreder-Kitzmüller, J. Hesse, A. Ebner, H. J. Gruber, and G. J. Schütz, "Non-exponential bleaching of single bioconjugated Cy5 molecules," *Chemical Physics Letters*, vol. 404:13–18 (2005).

[47] C. Julien, A. Débarre, D. Nutarelli, A. Richard, and P. Tchénio, "Single Molecule Study of Perylene Orange Photobleaching in Thin Sol-Gel Films," *Journal of Chemical Physics B*, vol. 109:23145–23153 (2005).

[48] W. E. Moerner, "Those Blinking Single Molecules," *Science*, vol. 277(5329):1059–1060 (1997).

[49] J. Schuster, J. Brabandt, and C. von Borczyskowski, "Discrimination of photoblinking and photobleaching on the single molecule level," *Journal of Luminescence*, vol. 127:224–229 (2007).

[50] A. Issac, C. von Borczyskowski, and F. Cichos, "Correlation between photoluminescence intermittency of CdSe quantum dots and self-trapped states in dielectric media," *Physical Review B*, vol. 71:161302 (2005).

[51] F. Vargasa, O. Hollricher, O. Marti, G. de Schaetzen, and G. Tarrach, "Influence of protective layers on the blinking of fluorescent single molecules observed by confocal microscopy and scanning near field optical microscopy," *Journal of Chemical Physics*, vol. 117(2):866–871 (2002).

[52] R. Zondervan, F. Kulzer, S. B. Orlinskii, and M. Orrit, "Photoblinking of Rhodamine 6G in Poly(vinyl alcohol): Radical Dark State Formed through the Triplet," *Journal of Physical Chemistry A*, vol. 107:6770–6776 (2003).

[53] X. Brokmann, J.-P. Hermier, G. Messin, P. Desbiolles, J.-P. Bouchaud, and M. Dahan, "Statistical Aging and Nonergodicity in the Fluorescence of Single Nanocrystals," *Physical Review Letters*, vol. 90(12):120601 (2003).

[54] J. P. Hoogenboom, E. M. H. P. van Dijk, J. Hernando, N. F. van Hulst, and M. F. García-Parajó, "Power-Law-Distributed Dark States are the Main Pathway for Photobleaching of Single Organic Molecules," *Physical Review Letters*, vol. 95:097401 (2005).

[55] R. Verberk, *Photon statistics and power-law blinking of single semiconductor nanocrystals*, Ph.D. thesis, Leiden University (2005).

[56] K. D. Weston, P. J. Carson, J. A. DeAro, and S. K. Buratto, "Single-molecule detection fluorescence of surface-bound species in vacuum," *Chemical Physics Letters*, vol. 308:58–64 (1999).

[57] I. Utke, P. Hoffmann, and J. Melngailis, "Gas-assisted focused electron beam and ion beam processing and fabrication," *Journal of Vacuum Science & Technology B*, vol. 26(4):1197–1276 (2008).

[58] L. G. Christophorou, J. K. Olthoff, and M. V. V. S. Rao, "Electron Interactions with CF4," *Journal of Physical and Chemical Reference Data*, vol. 25(5):1341–1388 (1996).

[59] B. Boudaïffa, P. Cloutier, D. Hunting, M. A. Huels, and L. Sanche, "Cross Sections for Low-Energy (10–50 eV) Electron Damage to DNA," *Radiation Research*, vol. 157(3):227–234 (2002).

[60] N. Silvis-Cividjian, C. W. Hagen, and P. Kruit, "Spatial resolution limits in electron-beam-induced deposition," *Journal of Applied Physics*, vol. 98:084905 (2005).

[61] Spectrum Laboratories, Inc., *Micro Float-A-Lyzer, http://www.spectrumlabs.com/dialysis/MicroFAL.html* (Accessed: Oct 14th, 2014).

[62] Bangs Laboratories, Inc., *TechNote 203: Washing Microspheres* (2013) http://www.bangslabs.com/support/technical-support/technotes.

[63] Molecular Probes, Inc., Invitrogen Detection Technologies, *Certificates of Analysis: TransFluoSpheres Fluorescent Microspheres* (2012/2013) http://www.lifetechnologies.com/order/catalog/product/T10711.

[64] M. T. Haring, N. Liv, A. C. Zonnevylle, A. C. Narvaez, P. Kruit, and J. P. Hoogenboom, "Automated sub-5nm overlay accuracy in correlative fluorescence and electron microscopy using cathodoluminescence pointers," (in preparation, 2014).

[65] Delmic, *Odemis Developer Manual: Release v1.5-81-g8c70a6b* (2014) https://github.com/delmic/odemis.

[66] The HDF Group, *Hierarchical Data Format, http://www.hdfgroup.org/HDF5/* (Accessed: Oct 19th, 2014).

[67] B. Bruhn, J. Valenta, F. Sangghaleh, and J. Linnros, "Blinking Statistics of Silicon Quantum Dots," *Nano Letters*, vol. 11(12):5574–5580 (2011).